2012-09-13

The Elastic Properties of Carbonaceous Chondrites

Ibrahim, El-Mahadia

UNIVERSITY OF CALGARY

The Elastic Properties of Carbonaceous Chondrites

by

El-Mahadia I. Ibrahim

A THESIS

SUBMITTED TO THE FACULTY OF GRADUATE STUDIES

IN PARTIAL FULFILMENT OF THE REQUIREMENTS FOR THE

DEGREE OF MASTER OF SCIENCE

DEPARTMENT OF GEOSCIENCE

CALGARY, ALBERTA

SEPTEMBER, 2012

Abstract

Asteroids have diverse lithologies as reflected in the range of recovered meteorites. Size distributions of clasts of asteroid 25143 Itokawa (LL-chondrite) and Tagish Lake meteorites (ungrouped C2 carbonaceous chondrite) indicate variation in fragmentation behavior. The steeper size distribution of the carbonaceous lithology apparently reflects its lower strength. A comparison between the smooth and rough terranes on Itokawa shows that fracturing or intracrater flows apparently eliminate larger fragments.

Carbonaceous chondrites' P- and S-wave velocities, which are indicators of the elastic moduli, exhibit variation with bulk density, petrologic type, and cosmic-ray exposure ages. The hydrated carbonaceous chondrites apparently record damage from collisions with weaker objects as indicated by their decrease of elastic velocities in proportion to their cosmic ray exposure ages. These inferred collisions are frequent relative to exposure ages of other major meteorite groups. These weaker impactors are not sampled in our meteorite collections, but are evidenced in the fireball population.

Dedication

To my mother

أمي إلى

Table of Contents

vii

List of Tables

List of Figures

half the meteorite to be destroyed by collisional processes (Figure adapted from Herzog, 2003).

List of Equations

(2.1) $N = C\, D^{-b}$

(2.2) $F = C'\, D^{-y}$

(2.3) $H = 18.1 - 2.5 \log \dfrac{pv}{0.1} - 5 \log \dfrac{D}{1\,Km}$

(2.4) $D = \dfrac{1347}{\sqrt{pv}}\, 10^{-H/5}$

(3.1) $E = \dfrac{\sigma}{\varepsilon}$

(3.2) $E = \rho_{Bulk} * V_E$

(3.3) $V_E = 2 * V_s^2 * (1 + v)$

(3.4) $\mu = \dfrac{\tau}{\gamma}$

(3.5) $\mu = V_s^2 * \rho_{Bulk}$

(3.6) $K = \rho_{Bulk} * \left(V_p^2 - \dfrac{4}{3} * V_s^2 \right)$

(3.7) $v = \dfrac{V_p^2 - 2*V_s^2}{2*(V_p^2 - V_s^2)}$

(3.8) $\lambda = K - \dfrac{2}{3} * \mu$

(3.9) $v = \dfrac{x}{t}$

(3.10) $Z = \rho.v$

(3.11) $V_{Sample} = V_{Container} - V_{Beads}$

(3.12) $V_{Beads} = \dfrac{M_{\,Beads}}{\rho_{\,Beads}} = \dfrac{M_{\,Total} - M_{Container} - M_{Sample}}{\rho_{\,Beads}}$

(3.13) $V_{Sample} = V_{Container} - \dfrac{M_{Total} - M_{Container} - M_{Sample}}{\rho_{\,Beads}}$

(3.14) $\rho_{Beads} = \dfrac{M_{Beads+\,Container} - M_{Container}}{V_{Container}}$

$$(3.15) \quad V_{Sample} = V_{Container} - \frac{M_{Total} - M_{Container} - M_{Sample}}{\frac{M_{Beads + Container} - M_{Container}}{V_{Container}}}$$

$$(3.16) \quad V_{Sample} = V_{Container} \left[\frac{M_{Beads+Container} + M_{Sample} - M_{Total}}{M_{Beads+Container} - M_{Container}} \right]$$

$$(3.17) \quad \rho_{bulk} = \frac{M_S}{V_S}$$

List of Symbols, Abbreviations and Nomenclature

a	Semi-major Axis
AMICA	Asteroid Multiband Imaging Camera
AU	Astronomical Unit
b	Slope of logarithmic cumulative size distribution
β	Slope of logarithmic cumulative mass distribution
C or $C`$	Constant
cm^3	Cubic Centimetre
CRE	Cosmic Ray Exposure
C-chondrites or CC's	Carbonaceous Chondrites
CI	Ivuna-like chondrites
CM	Mighei-like chondrites
CR	Renazzo-like chondrites
CO	Ornans-like chondrites
CV	Vigarano-like chondrites
CK	Karoonda-like chondrites
D	Diameter of Particle/ Boulder/Asteroids
e	eccentricity
ε	Strain
GPa	Gigapascal

H	Apparent Magnitude
i	Inclination angle
ISAS	Institute of Space and Astronautical Science
ESA	European Space Agency
JAXA	Japan Aerospace Exploration Agency
JPL	Jet Propulsion Laboratory
JHUAPL	John Hopkins University-Applied Physics Laboratory
km	Kilometer
LINEAR	Lincoln Near-Earth Asteroid Research
LL-chondrites	Low-iron Low-metal chondrites
MGS	Mars Global Surveyor
MBA	Main Belt Asteroids
MOC	Moving Object Catalogue
MY	Mega year
N	Number of Particles/ Boulders/ Asteroids
NASA	National Aeronautics and Space Administration
NEA	Near-Earth Asteroid
NEC	Near-Earth Comet
NEAT	Near-Earth Asteroid Tracking
NEO	Near-Earth Observation
PHA	Potentially Hazardous Asteroids

pv	Geometric Albedo
PVC block	Polyvinyl chloride Block
PRSFD	Preliminary Raw Size-Frequency Distribution
Q	Aphelion
q	Perihelion
σ	Stress
SAO	Smithsonian Astrophysical Observatory
SDSS	Sloan Digital Sky Survey
SKADS	Sub-Kilometer Asteroid Diameter Survey
SMBAS	Subarau Sub-km Main-Belt Asteroid Survey
TL	Tagish Lake
UMD	University of Maryland
WISE	Wide-field Infrared Survey Explorer
y	Slope of logarithmic incremental size distribution

Chapter One: Introduction

About 4.6 billion years ago, a dense cloud of interstellar gas and dust matter collapsed under its own gravity. As a result of this collapse, a rotating gas and dust cloud was formed, and most of the gas and dust mass migrated to the center of this nebula forming a star known as the Sun while the remaining mass orbited around the newly formed Sun as a flattened protoplanetary disk. With the slow accretion of the gas and dust of the protoplanetary disk, most of the mass was incorporated into large objects, such as planets and moons, and the rest of the material that was not involved into planetary formation, or blown away by solar winds or sunlight, exists today in the form of populations of small objects widely known as small solar system bodies. These bodies are primitive in nature and were considered to be the "vermin of the skies" at some point of history (McSween, 1999); however, with the advances in observations, their potential role in understanding planetary evolution has now become of high interest in the planetary science community and other disciplines.

Small solar system objects – asteroids and comets – have preserved their initial chemical and physical properties to a degree relative to the large objects that have undergone complex geological and thermal processes, which provides an excellent opportunity to learn about the early conditions of the solar system as preserved within these small objects.

Asteroids are rocky objects residing primarily in a region in the Solar system known as the Asteroid Belt or the main belt (Figure 1.1), which is located between Mars and Jupiter between 2.06 and 3.65 AU from the Sun (Lewis, 2004). Complex collisional

and dynamical processes have resulted in the current observed distribution of the asteroids in the main belt, including the formation of asteroid families with similar orbital properties, and the presence of gaps in the orbital distribution of these objects as a result of resonances with other planets (Figure 1.2). Within the active environment of the main belt, those objects that are thrown into a resonance region are ejected from the main belt due to perturbations with Jupiter or other planets (e.g. secular resonance with Saturn). Some of these asteroids end up perturbed into the inner solar system where they are known as near-Earth objects (Figure 1.3), and they may have collisions with the inner terrestrial planets.

On the other hand, comets reside on the tail-end of the protoplanetary disk in two other planetesimals reservoirs; one is known as the Kuiper Belt (Figure 1.1), which is the region extending outwards from Neptune' orbit at ~ 35 AU to several hundred AU (Weissman et al., 2002). The other is a spherical region outside the Kuiper belt between 10^3-10^5 AU known as the Oort cloud. Unlike asteroids, comets have substantial amounts of ice and volatiles in their structure, which escape and engulf the comet nucleus when it is heated near the Sun. Comets' orbital evolution is believed to be governed largely by gravitational perturbations exercised by the large planets during their formation (Jupiter, Uranus, Saturn and Neptune), and later by galactic and stellar perturbations with the increasing distance from the Sun.

The primitive solar system objects do not only provide a glimpse into the early solar system compositions, but they are the result of the collisional and dynamical processes that have resulted in the current size distribution. Collisions between asteroids control their size distribution, as asteroids break up into smaller objects (O'Brien, 2004).
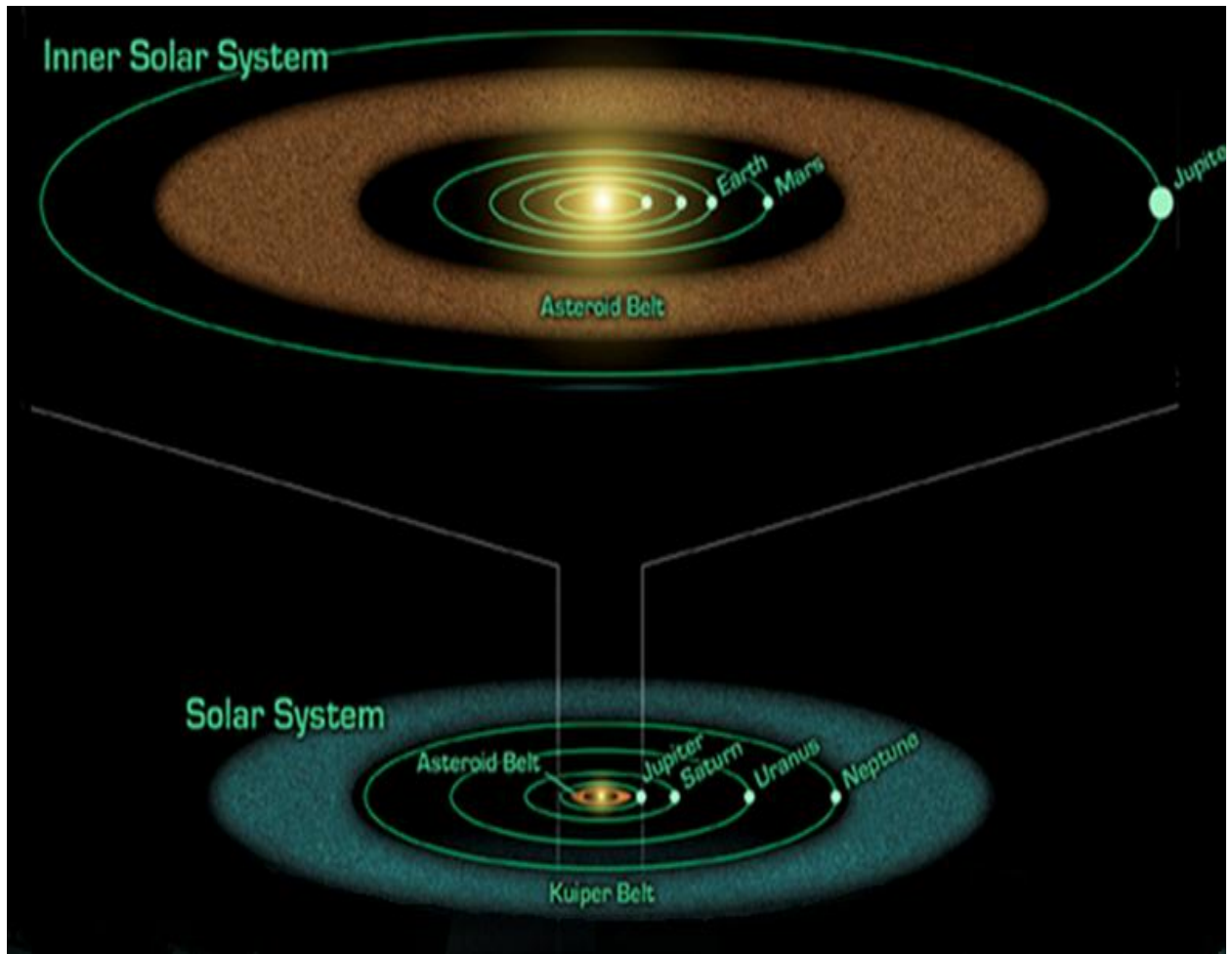
Figure (1.1): An illustration of the Solar system; the inner part shows the Terrestrial planets, moving outwards the Main Asteroid Belt and Trojan asteroids, the Gas Giants, and the Kuiper Belt region (http://www.nasa.gov/mission_pages/spitzer/multimedia/20081027b.html accessed July 28, 2012).
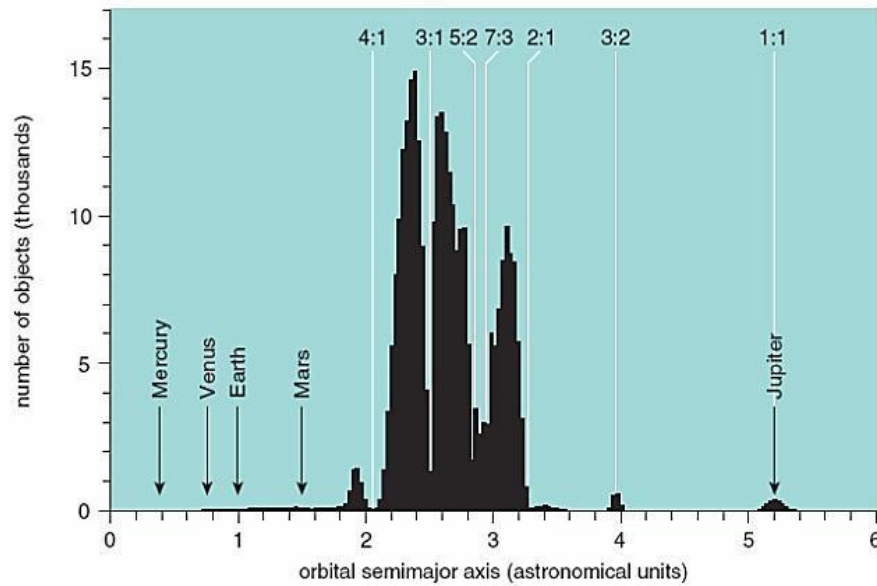
Figure (1.2): shows gaps in the semi-major axes of asteroids in the asteroid belt, known as the Kirkwood gaps, and form as a result of resonances with Jupiter (Lewis, 2004).

Extensive research has been done on the evolution of main-belt asteroids size distribution (e.g. Ivezić et al., 2001; and references therein); however, there is still a significant deviation for the observed distribution from the theoretical predictions (O'Brien, 2004). Most theoretical work assumes that the strength properties of asteroids are totally independent of the size, and models were developed based on this assumption. However, more sophisticated modeling now suggests that small ($\leq$ 1 km) asteroids' physical properties result in weak structure for the whole asteroid body with increasing size; whereas, larger asteroids become stronger with increasing size due to "gravitational self-compression" and in cases of fragmentation, the fragments are stronger due to "gravitational reaccumulation" (O'Brien, 2004). Reliable data about the observed size distribution of asteroids provide constraints on the strength properties of asteroids

(O'Brien, 2004); however, gaining reliable data on the strength properties of asteroids will provide constraints on their size distribution, and collisional evolution.
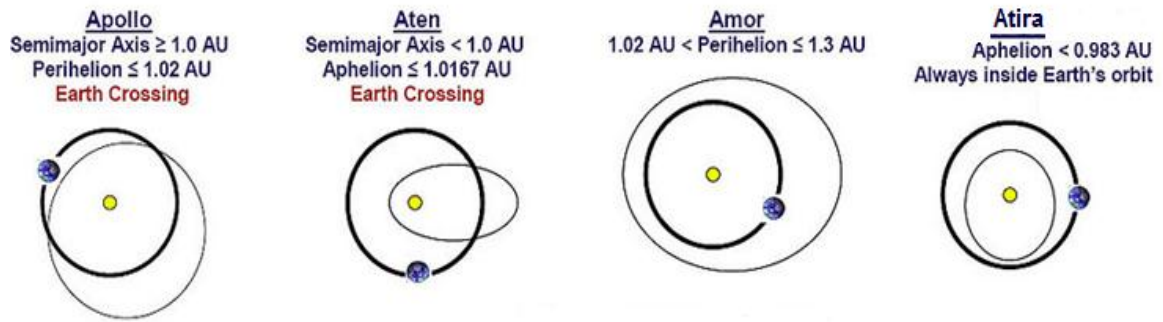
Type of Asteroids	Discovered number of objects (updated 18th of July, 2012)
Apollos	4866
Atens	712
Amors	3385
Atiras	11

Figure (1.3): Near-Earth Asteroids (NEAs) have orbits that bring them relatively close to the Earth; Apollos, Atens, Amors and Atiras, with the number of discovered NEAs discovered up to July 18, 2012 (Both figure and table were courtesy of the NEO program website accessed July 18, 2012). Blue dot is Earth and yellow is the Sun.

In situ measurements on asteroids' surfaces are extremely costly. Fortunately, during its orbit around the Sun, Earth collects free samples of solar system objects, from asteroids and comets, ranging from dust particles on the micrometer scale up to meters in diameter. Most of the material received does not survive the entry into the Earth's atmosphere, but particles that survive have been recovered from the atmosphere as

interplanetary dust particles, or found and recovered from the dry surfaces of the continents in the form of meteorites.

In recent decades, the study of meteorites has made major advances in determining composition, chemistry, mineralogy, and age of meteorites. Combined with other disciplines, such as planetary astronomy, astrophysics, analytical chemistry, and the origin of life, the field of meteoritics have provided knowledge on the composition, chemistry, and mineralogy of asteroidal and cometary fragments, and provided evidence for various chemical and physical processes that will assist in answering the questions pertaining to the birth and evolution of our solar system among others (Lauretta and McSween, 2006).

The variation in meteorites' physical strength causes bias in our current meteorite collections (Lewis, 1997), by over representing the stronger meteorites (e.g. iron, stony irons, and ordinary chondrites) while underrepresenting the weaker material (e.g. carbonaceous chondrites). The size and shape distributions of meteorites might provide limited insight into their original properties, but they provide significant information about the physics of meteorites' atmospheric entry, and ultimately information about their parent bodies' responses to collisions and impact cratering processes (Chapter Two).

Response to collisional processes is governed by the strength properties, which vary significantly with the composition of meteorites (Lewis, 2004). In our meteorite collection to date, the CI carbonaceous chondrites are known to be the weakest meteorite specimens as they can be crushed easily. In addition to composition, physical strength was found to be influenced by shock history, oxidation state, volatile content, and degree of terrestrial weathering (Lewis, 2004). Some constraints on the strength of meteoritic

material were obtained from observing pristine samples as they enter the atmosphere and recording their fragmentation prior to landing on the Earth surface (e.g. Halliday et al., 1996). However, a more applicable, straightforward approach to gaining data on the strength properties of meteorites is through direct measurement of physical and elastic properties of meteorite samples.

The present study aims to gain a better understanding of the physical properties of the weaker population amongst the meteorites in our collections; the carbonaceous chondrites. This is accomplished by using non-destructive techniques as this class of meteorites is very rare, and is fragile in structure. We used elastic wave velocities of meteorites, combined with their bulk density, to calculate their elastic moduli. This methodology is benign, as it does not alter or modify the samples in any way, and at the same time could be performed in situ relatively quickly. The elastic properties' variations with other physical properties provide some insight on the nature of the meteorites and their respective parent bodies (Chapter Three).

Implications on the carbonaceous chondrites class of meteorites and their impact rates with other classes could be attained from the cosmic ray exposure ages, as the latter reflect the amount of time a meteorite spent in space between exaction from parent body and collision with Earth. The variations in elastic properties with CRE ages provide some information on the interaction of carbonaceous chondrites with stronger and with weaker material. The final chapter (chapter four) will attempt to discuss these implications, mutual impact rates between different meteorites classes, their survivability, and representation in the fireball population.

The Appendices include the data acquired in this the study; the size distribution analysis of Itokawa and Tagish Lake, data on the elastic wave velocities, bulk densities, elastic moduli, and equations used to calculate the mutual impact rates between the different meteorite classes, and finally some notes for future work that would be useful.

Chapter Two: Chapter Two: A Comparison of Size-Frequency Distribution

2.1 Introduction

Images of variable resolution obtained by various flybys of asteroids' surfaces, such as Gaspra, Ida, Mathilde, Eros, Steins, Lutetia, and Itokawa, and the Martian satellites Deimos and Phobos have proven that the regolith of small objects could be unexpectedly ubiquitous (Figure 2.1). The ongoing planning of asteroidal sample-return missions has increased the interest in the physical properties of asteroids' regoliths as these will govern sampling strategies. Asteroids' regoliths have been generated by impact cratering on the underlying protoliths and altered by gardening from smaller impacts.

Numerical simulations of the size distributions of asteroids resulting from impact cratering and/or catastrophic collisions have increased in validity, in part because of the advances made in telescopic observation programs dedicated to studying asteroids, and the ever improving computational capability used to perform these simulations. Imagery obtained from flyby and rendezvous missions have allowed several studies of size distribution of ejecta fragments (boulders) scattered on asteroids' surfaces. The ongoing development of better spacecraft instruments and rendezvous missions has increased the resolution and quality of the obtained data.

This part of the project aimed to conduct a comparison of clasts' size-distribution of two objects with different lithologies; asteroid 25143 Itokawa (LL-chondrite lithology), and C2-ungrouped carbonaceous chondrite Tagish Lake. On Itokawa, three geologic terranes were imaged by the Hayabusa spacecraft with high resolution, and

therefore suitable for detailed size and shape distribution analyses of the boulder population.
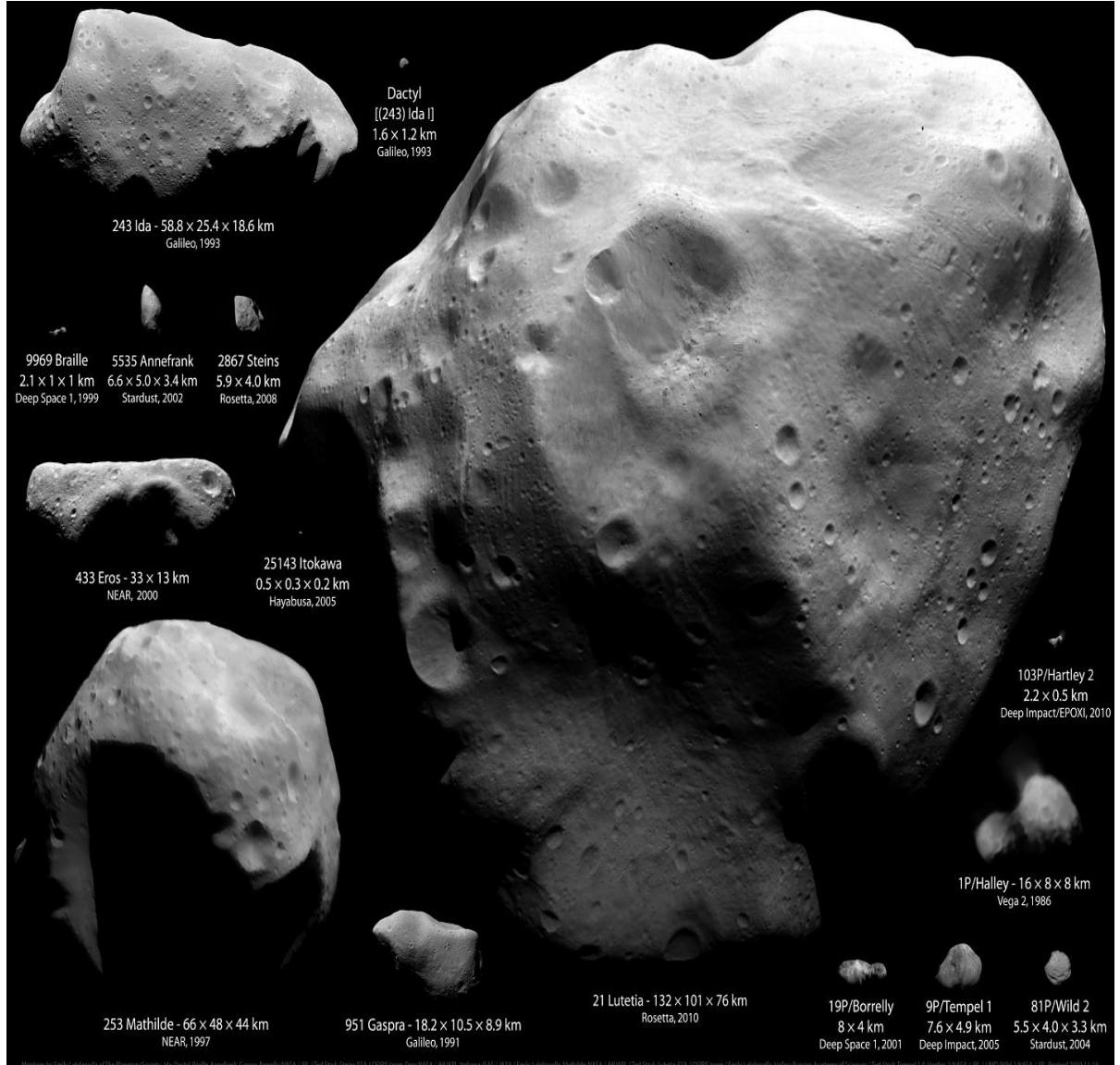
Figure (2.1): Montage by E. Lakdawalla. Ida, Dactyl, Braille, Annefrank, Gaspra, Borrelly: NASA / JPL / T. Stryk. Steins: ESA / OSIRIS team. Eros: NASA / JHUAPL. Itokawa: ISAS / JAXA / E. Lakdawalla. Mathilde: NASA / JHUAPL / T. Stryk. Lutetia: ESA / OSIRIS team / E. Lakdawalla. Halley: Russian Academy of Sciences / T. Stryk. Tempel 1, Hartley 2: NASA / JPL / UMD. Wild 2: NASA / JPL. The last asteroid visited by a spacecraft, Vesta, is not included.

10

On the other hand, multiple fragments of disaggregated samples of Tagish Lake meteorite were measured via traditional sieving and caliper measurement to produce a size-frequency distribution. The results for the two objects are compared to gain a better understanding of the fragmentation behavior between two different lithologies, with emphasis on the fragmentation in the much weaker dark asteroid lithology.

The following sections will briefly introduce the topic of particle size distribution, examples of size distribution of small solar system objects, and then Itokawa versus Tagish Lake in the last two sections followed by the conclusions and implications.

2.2 Particle Size Distribution: An Introduction

Notes to the reader: The discussions here are taken in large part from Hogg (2011), Hartmann (1969), and O'Brien (2004).

The Glossary of Geology defines particle size distribution as the fraction, percentage, weight, or number of counts of particles in each size fraction. Size distribution analysis is a useful tool in studying particle behavior within various systems; constructive systems such as crystallization or agglomeration, or destructive systems such as collisions. Multiple methodologies have been developed to study size distribution; however, the selection of a suitable technique depends mainly on the purpose of study and type of material investigated. The fractional form of size distribution is considered a practical method of presenting any size distribution analysis (Hogg, 2011), and involves producing graphic plots of the particle "quantity" versus particle "sizes". Particle sizes are generally given in terms of length, surface area, volume, or mass; whereas, quantities – numbers, masses, or volumes - are plotted against selected size pins either in

incremental or a cumulative distributions (Figure 2.2), in linear or logarithmic formats (Hartmann, 1969).

Generally, incremental size distributions have the advantage of showing the fine details in populations' behavior while cumulative distributions smooth out most of the details. In general, studies of planetary fragmentation commonly use cumulative size distributions to gain a more practical presentation of results. Regardless of the approach taken for any size distribution analysis, it is critical to define two parameters; the particle size as a linear dimension (usually the mean horizontal diameter using images, and the mean dimension using caliper measurements), and the sampling size of the measured particle population since any bias in the sampling process will give unreliable results (Hogg, 2011).
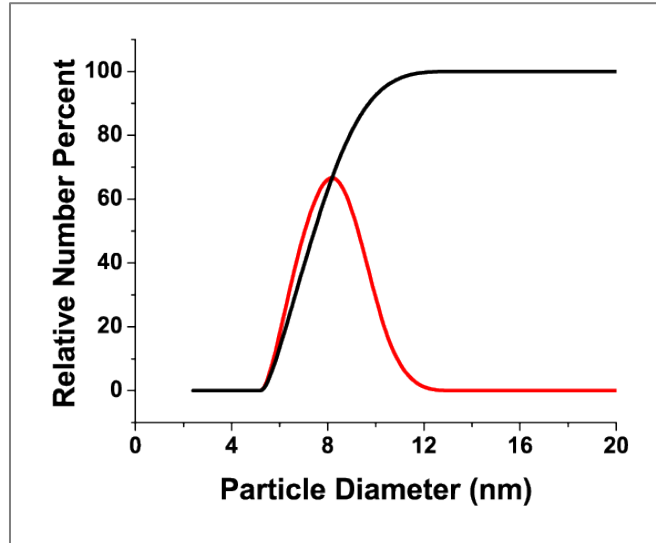
Figure (2.2): illustration of size distribution analysis, where red line is incremental fragment size distribution and black line is cumulative size distribution, using a linear format.

Most studies integrate all measured particles' sizes to produce a cumulative curve or a line that could be presented mathematically, and could be used to predict data behavior beyond the given data points. However, sometimes this integration may conceal small variations within the population, which may prove meaningful at some stage in the future.

On asteroids' surfaces, as well as on Earth, boulders' size distributions are observed to follow a power-law distribution (e.g. Hartmann, 1969):

$$N = C \, D^{-b} \qquad\qquad (2.1)$$

Where N is the cumulative number of fragments with sizes $> D$, b is the power-law index (slope) in a $\log N - \log D$ plot, and C is a constant.

In a logarithmic incremental presentation, the size distribution power-law becomes:

$$F = C' \, D^{-y} \qquad\qquad (2.2)$$

Where F is the number of fragments within a logarithmic increment, y is the slope and C' is the constant. It is critical to define what type of increment is being used (Hartmann, 1969); logarithmic incremental distributions have the same slope as linear cumulative distributions ($b = y$); however, using a linear incremental distribution will have a different slope than a linear cumulative distribution [$y = -(b + 1)$].

The steepness of the power-law slope depends on the behavior of the objects being fragmented, and the frequency of the fragmentation processes, as in fragment populations produced by a single fragmentation process show shallower slopes than those

13

broken during two or more stages of fragmentation. Similarly, populations with low strength properties are expected to break more easily under external forces and are more likely to show steeper slopes than those with higher strength (Hartmann, 1969). In this study, multiple stages of fragmentations have influenced the size distribution of both asteroid Itokawa and Tagish Lake meteorite; therefore, in comparing the two objects, the focus will be on the strength of the objects as the factor affecting the population size distribution.

As in many size distribution measurements, the basics include measuring the quantity of the particles since the size is determined more or less by the measurement instrumentation or methodology; e.g. mesh diameters in sieving define the size ranges for each particles' fraction. Three methodologies have been followed throughout the study; (1) direct measurement of individual particles (boulders) on Itokawa via image analysis, (2) direct measurement of Tagish Lake fragments via axial measurement using a digital caliper, and (3) size-separated particle measurement through conventional sieving, which involves classification of material sizes based on particles ability to pass through certain aperture size; thus, size is measured indirectly from the assigned aperture size.

All of the adopted methodologies have certain disadvantages associated with equipment including size limitations, resolution and operational constraints. An example of size limitations in image analysis is the defined size ranges optimum for operation, resolution determines the lower size limit and counting statistics determines the upper size limit. Resolution problems are observable in some techniques, such as sieving, which provide less resolution. However, sieving is excellent in discriminating particular aperture sizes, but it provides no specific information on intermediate sizes (Hogg, 2011).

Moreover, other factors affect the suitability of the different procedures for specific applications such as operator experience and equipment logistics.

2.3 Size Distribution of Selected Planetary Objects: A Literature Review

Many of the observed asteroids properties such as size, shape, and rotational properties provide a direct or indirect link to the collisional evolution of these objects (La Spina and Paolicchi, 1996). Blocks on asteroids' surfaces form as results of impacts and/or catastrophic disruption of their parent bodies; thus, their size distribution provides some insight into their parent bodies' physical properties.

2.3.1 Size Distribution of the Main Belt Asteroids

The current size distribution of the main belt asteroids is believed to have been modified by the continuous collisional processes and orbital evolution that dominate the main belt (Masiero et al., 2011); however, measurement of the current distribution provides some constraints for studying the initial conditions of asteroids. A number of systematic surveys have been conducted on the size distribution of the Main Belt asteroids, for objects ranging from hundreds of kilometers down to a few hundreds of meters (Yoshida, 2012; and references). Since asteroidal diameters cannot be measured directly, a corresponding measurement is commonly used to reflect their sizes, known as the apparent magnitude *H*. The apparent magnitude H is the visual magnitude an observer would record if the asteroid was placed 1 AU away from the Sun at zero phase angle (e.g.

Parker et al., 2008 and references). The lower the magnitude, the larger the object will be. The conversion from this magnitude to an equivalent diameter requires the knowledge of the geometric albedo pv. An "albedo" of any surface is the amount of light reflected by that surface depending on its composition. If the geometric albedo pv is known, then the diameter can easily be obtained using (Parker et al., 2008):

$$H = 18.1 - 2.5 \log \frac{pv}{0.1} - 5 \log \frac{D}{1\,Km} \qquad (2.3)$$

The ability to gain better accuracy of measuring the albedos (and consequently the equivalent diameters) of large populations of asteroids provides a better insight into the size distribution of the current asteroid populations. The majority of asteroids' telescope observations are conducted in visible light wavelengths, which assumes an albedo to convert the H magnitude to diameters. Recently, this was addressed by conducting infrared observations of asteroids, such as the Wide-field Infrared Survey Explorer (WISE), which allows for better size-frequency distribution analyses of asteroids independent of any assumptions of albedos to convert from H magnitudes to equivalent diameters (Masiero et al., 2011).

The main belt asteroid size distribution was obtained by a number of observation surveys; such as, the Sloan Digital Sky Survey (Ivezić et al., 2001), which produced a power-law index of -2.3 ± 0.05 for asteroids ranging between 400 m and 5 km in diameter. Another survey conducted by the Subarau Sub-km Main-Belt Asteroid Survey (SMBAS) covered size ranges between 500 m and 1 km diameter asteroids and found a

power-law index of -2.19 ± 0.02 (O'Brien et al., 2004). The WISE data yield preliminary results on the observed diameters and the cumulative "preliminary raw size-frequency distribution" (PRSFD) for the three main regions of the Main Belt of asteroids. The inner-Main Belt extends between a = 1.8 - 2.5 AU, the middle-Main Belt between a = 2.5 - 2.82 AU, and the outer-Main Belt between a = 2.82 - 3.6 AU. For small objects, the power-law index in the three regions was found to be consistent with the index reported by Gladman et al. (2009) survey, with a value of -2.5 (Masiero et al., 2011); however, a significant change in slope was also observed for these objects for diameters between 15-25 km (Figure 2.3).
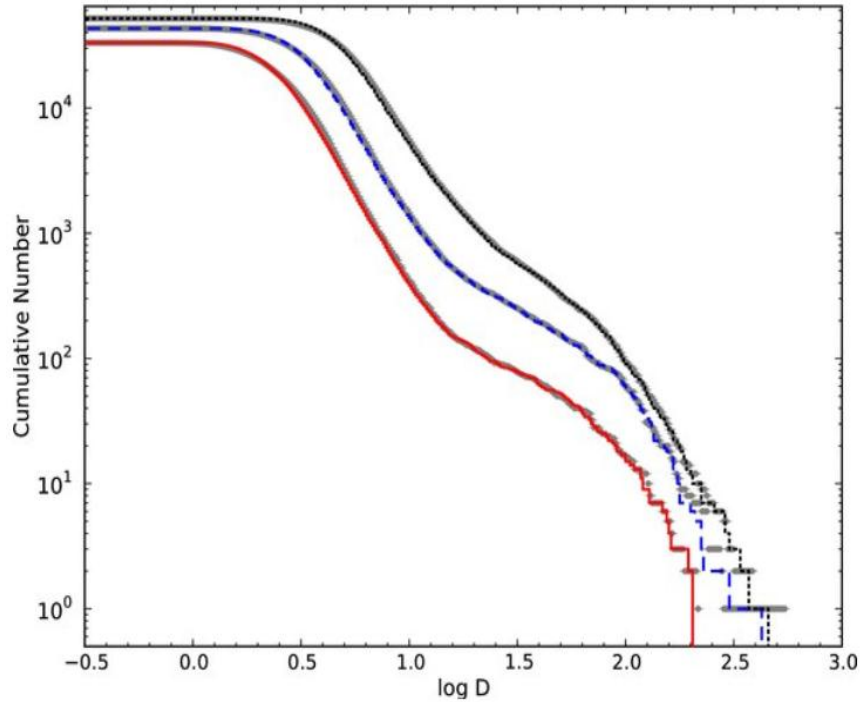
Figure (2.3): Cumulative raw-size distribution of the main belt asteroids in the inner-(red), middle- (blue), and outer-main belt (black). Plotted under the distributions are gray points showing the Monte Carlo simulation for each dataset; the error bars are the size of the points (figure and caption adopted from Masiero et al., 2011).

17

2.3.2 Size Distribution of the Asteroid Families

Approximately a century ago, Hirayama (1918) recognized clusterings of asteroids in proper orbital element space that were not random, but are believed to have resulted from catastrophic impact fragmentation of a large parent body (Marzari, 1995). The orbital elements (semi major axis, eccentricity, inclination, longitude of the ascending node, argument of periapsis, and the mean anomaly) experience long- and short-term oscillations caused by planetary perturbations; whereas proper orbital elements eliminate these oscillations to produce time-independent orbital elements (Lewis, 1997). Several of these families are apparent by simply observing plots of proper orbital elements (Figure 2.4), and have been universally accepted since Hirayama's work and also validated by colors from the SDSS survey (e.g. Nesvorny et al., 2005). Some families, especially the smaller populations, required further statistical analyses of large datasets to be established (Zappala et al., 1995). The remaining populations that were less pronounced than the families, with still statistically significant clusterings, were identified as "clumps" (O'Brien, 2004).

The current size distributions have retained the signature of the most recent break up event(s); however, subsequent collisions continued to modify the sizes and orbital parameters of each family members (Marzari, 1999), which means that the observed size distribution today is different than the one that resulted from the initial distribution of the parent body. Different approaches have been taken to study asteroid families' size distributions. Some studies focus on certain regions of the observed size distribution

18

curves to produce an estimate of the original distribution of the population and the subsequent modifications that occurred to it (e.g. Anders, 1965; Hartmann and Hartmann, 1968) while other studies were concerned with the overall power-law fit of the distribution over a wide size range. Regardless of the approach and methodology, size distribution analyses of the families are restricted by detection limitations and lack of accurate measurement of the member dimensions.
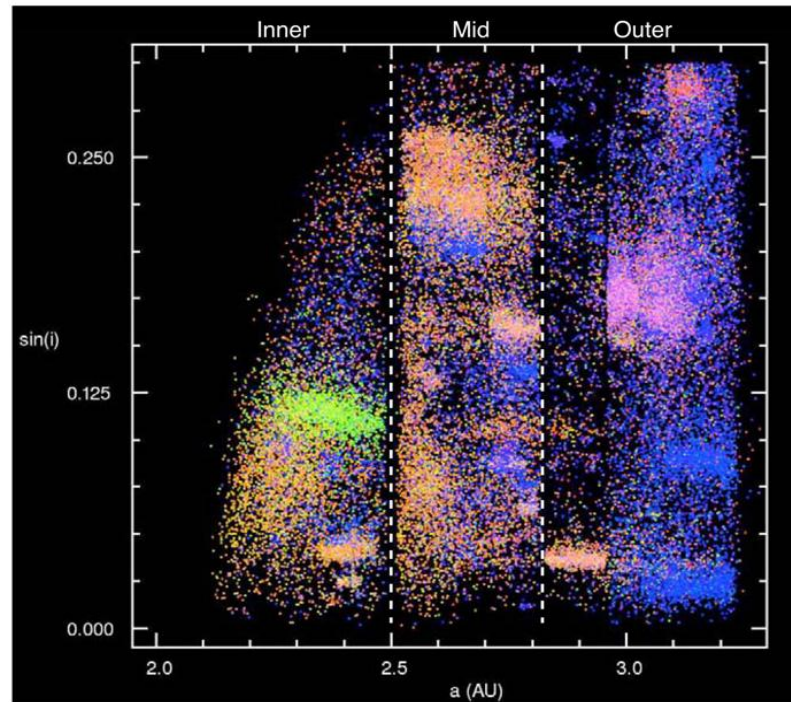
Figure (2.4): A plot of 40,000 asteroid families in the asteroid main belt as acquired from the Sloan Digital Sky Survey SDSS photometric data. The x-axis represents the semi-major axis a, while the y axis is the sine of the inclination angle i. Significant color variations exist between different asteroid families partly because of the varying mineralogy of their parent asteroids and probably also due effects of space weathering. Their distinctive optical colors indicate that the variations in chemical composition within a family are much smaller than the compositional differences between families,

19

and strongly support earlier suggestions that asteroids belonging to a particular family have a common origin (adopted from Parker et al., 2008).

The most recent size distribution studies of asteroid families using telescopic surveys have been conducted using Sloan Digital Sky Survey Moving Object Catalog 4 (e.g. Parker et al., 2008; Nesvorný et al., 2005). According to Parker et al. (2008), the size distribution is significantly variable among the families and differs from that of the background populations. Travelling inwards from the outer asteroid belt towards inner belt, the size distribution of the families becomes steeper (Figure 2.5), producing power-law indices ranging from -2.9 in the outer region, -3.0 in the middle region, to -3.3 in the inner region of the asteroid belt. This could be attributed to the observation of Parker et al. (2008) that S-type asteroids, which are the main residents of the inner belt region, show steeper slopes than C-type asteroids residing in the outer belt region, and older families tend to show steeper slopes than younger families, which might have also contributed to this difference in slope.
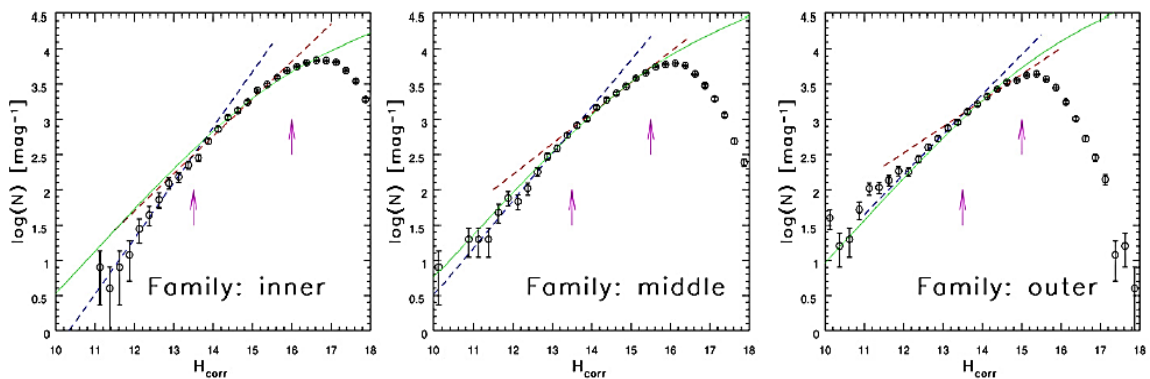
Figure (2.5): Illustration adopted from Parker et al. (2008) of the asteroids families magnitude distribution, travelling inwards from the outer region of the asteroid belt towards the inner region of the belt, they found out that the power-law index of the

distribution becomes steeper ranging from -2.9 in the outer belt, to -3.0 in the middle, to -3.3 in the inner part of the belt.
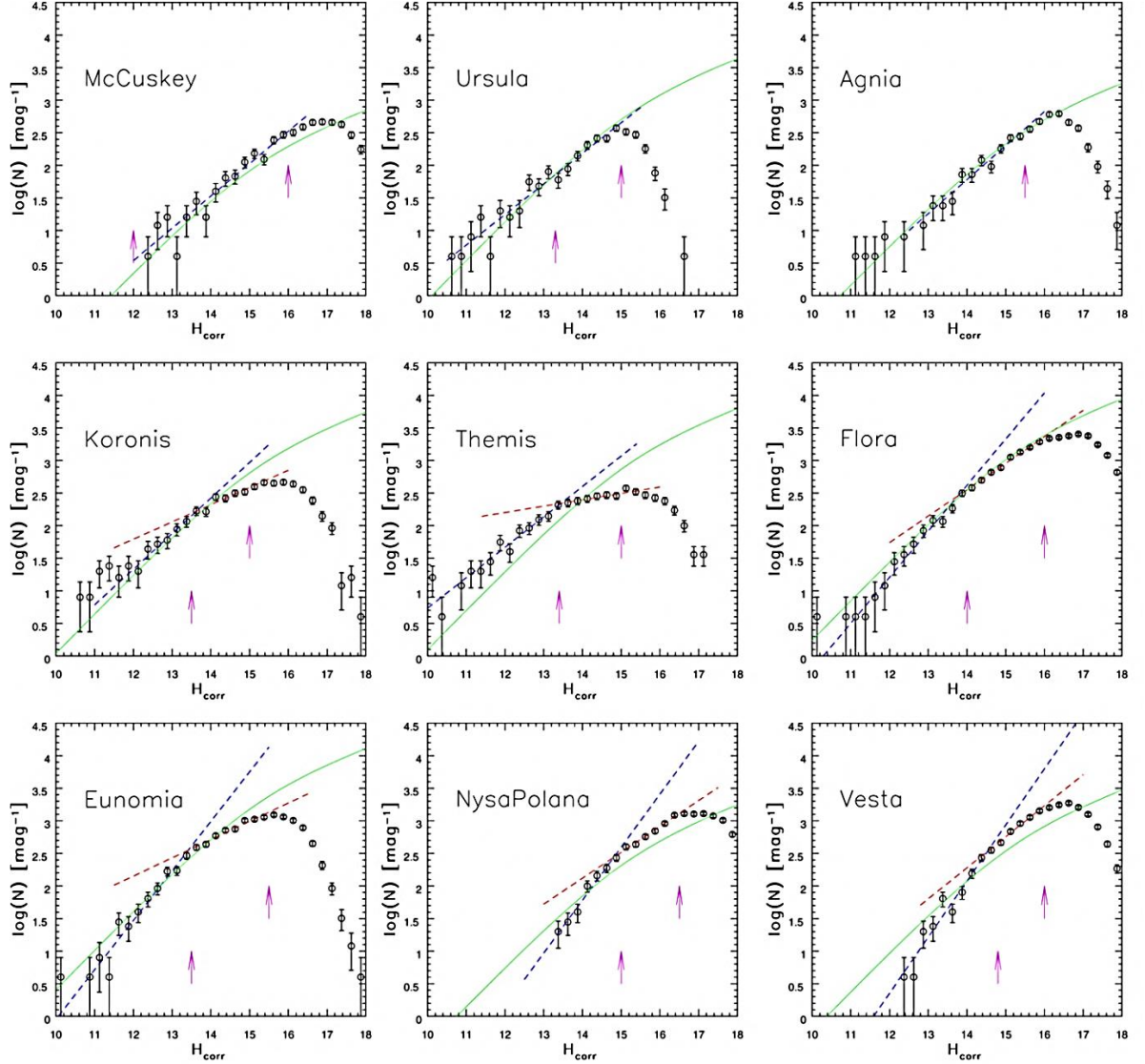
Figure (2.6): A plot of nine families; the first three panels (from top left to bottom right) show examples of families that follow a single power-law magnitude distribution, and the remaining six panels show magnitude distributions for families that require a double power-law fit. The two dashed lines show the best-fit "broken" power law: a separate power-law fit for the bright and faint end (Figure and caption adopted from Parker et al., 2008).

Parker et al. (2008) reported that out of 37 observed asteroid families, the size distribution for 15 families showed a change in slope that could be fit with a double power-law (Figure 2.6). This bimodal power-law apparently corresponds to the taxonomical type and the age of asteroids, as more S-types displayed it than C-type asteroids and older families' more than younger ones (Parker et al., 2008).

Furthermore, three of the most populous families in the asteroid belt, Koronis, Themis and Vesta, exhibit power-law indices of -2.08, -2.0, and -3.8, respectively (Parker et al., 2008).

2.3.3 Size Distribution of the near-Earth asteroids NEA

Some comets and asteroids have been nudged by gravitational perturbations into orbits that allow them to intersect with Earth's orbit, and the vast majority of these Earth-crossing objects are asteroids. Near-Earth asteroids are divided into groups based on their perihelion distances, aphelion distances, and semi-major axes, with ~1300 amongst them identified as Potentially Hazardous Asteroids (PHAs) that might pose as a threat to Earth at some point in the future (Table 2.1). Similarly to the main belt asteroids, the equivalent diameter of NEAs (in kilometer) could be obtained given the geometric visual albedo pv, using the equation:

$$D = \frac{1347}{\sqrt{pv}} 10^{-H/5} \quad (2.4)$$

(O'Brien, 2003)

22

NEA albedos that have been determined are generally from ground-based surveys, which resulted in a much wider range of albedo values than that of the main belt asteroids (O'Brien, 2004). Rabinowitz et al. (2000) provided an estimate of the NEA distribution down to H = 30 (for an albedo of 0.11, the equivalent diameter of 4 m using Spacewatch and Near-Earth Asteroid Tracking (NEAT) program (Figure 2.7). LINEAR survey allowed for determination of NEA distribution down to H = 22.5, which is equivalent to 85 − 190 m diameter asteroids (Stuart, 2001) and H = 25.5, which is equivalent to 20 − 50 m diameter asteroids (Harris, 2002).

Group	Description	Definition
NECs	**Near-Earth Comets**	$q<1.3$ AU, $P<200$ years
NEAs	**Near-Earth Asteroids**	$q<1.3$ AU
Atiras	NEAs whose orbits are contained entirely with the orbit of the Earth (named after asteroid 163693 Atira).	$a<1.0$ AU, $Q<0.983$ AU
Atens	Earth-crossing NEAs with semi-major axes smaller than Earth's (named after asteroid 2062 Aten).	$a<1.0$ AU, $Q>0.983$ AU
Apollos	Earth-crossing NEAs with semi-major axes larger than Earth's (named after asteroid 1862 Apollo).	$a>1.0$ AU, $q<1.017$ AU
Amors	Earth-approaching NEAs with orbits exterior to Earth's but interior to Mars' (named after asteroid 1221 Amor).	$a>1.0$ AU, $1.017<q<1.3$ AU
PHAs	Potentially Hazardous Asteriods: NEAs whose Minimum Orbit Intersection Distance (MOID) with the Earth is 0.05 AU or less and whose absolute magnitude (H) is 22.0 or brighter.	$MOID<=0.05$ AU, $H<=22.0$

Table (2.1): shows different NEA groups according to their perihelion distance (q), aphelion distance (Q) and their semi-major axes (a).
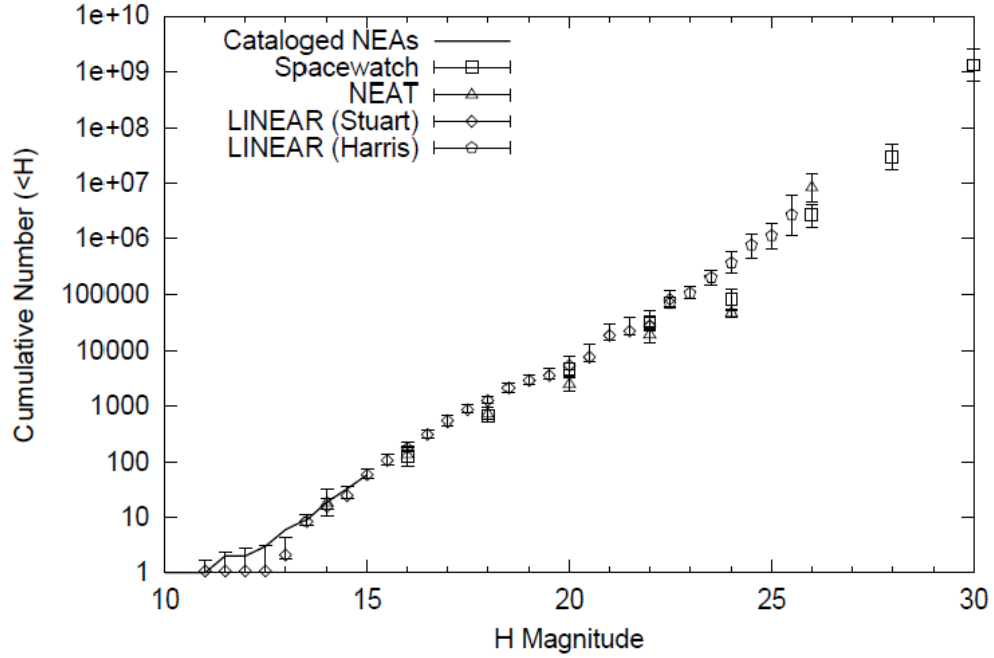
Figure (2.7): Plot of observational estimates of the NEA size distribution. The solid line is the cataloged population of NEAs from the JPL DASTCOM database. Squares and triangles are the Rabinowitz et al. (2000) estimate using Spacewatch and NEAT data. Diamonds are the Stuart (2001) estimate using LINEAR data, and pentagons are the Harris (2002) extension of that estimate. Assuming a constant albedo, as the H-magnitude of a body increases, its diameter decreases (Figure and caption adopted from O'Brien, 2004).

2.3.4 Size Distribution of Blocks on Asteroids

Boulders on asteroids surfaces are useful in providing some insights on the physical criteria and geological processes modifying asteroids' surfaces since these boulders are products of impact processes and surface processes over 4.6 billion years (Michikami et al., 2008). Boulders are produced as ejecta from impacts and only ejecta with velocities smaller than the escape velocity of the asteroid fall back and settle on the

24

surface under the influence of gravity. Over the last decades, several missions obtained data about asteroids' surfaces and boulders' spatial and size distributions from flyby and rendezvous imagery. Amongst the most studied surfaces are the Martian satellites Phobos and Deimos, and the asteroids 243 Ida, 433 Eros and 25143 Itokawa (Thomas et al., 2001; Lee et al, 1996; Michikami et al, 2008).

Eros is an S-type asteroid with an irregular shape ~ 34×13×13 km in dimensions. Prior its landing on Eros, the NEAR Shoemaker spacecraft orbited Eros for one year and imaged its entire surface at ~ 4 m/pixel resolution or better, and the landing area of NEAR was identified down to the centimeter scale (Veverka, 2002). Almost 180,000 images have been obtained for the entire surface from the orbital mission of NEAR, which allowed for the detailed mapping of craters and ejecta blocks. A size distribution study was conducted for blocks down to ~5 cm in diameter (Thomas et al., 2001). They used the mean horizontal dimensions of positive relief features on the surface as the block size. Positive relief features were defined as "Partially buried or weathered blocks with faint outlines, piles of regolith scree, protruding bedrocks, raised crater rims, and intersecting crater walls".

Approximately 6700 blocks were found across 1125 km^2 of the asteroid with variable sizes across the surface (Thomas et al., 2001). The global size distribution of blocks between sizes of 15 m and 80 m over the entire surface of Eros has a power-law index of -3.2 (Figure 2.8). However, different regions show different slopes for the cumulative size distribution of blocks. Some regions that might have undergone less processing of the material show lower slopes than average, whereas regions with blocks less than 10 cm in diameter show slopes of -6, which indicate the absence of larger

blocks. This size sorting effect was suggested to be a result of ejection of blocks and re-impact processes on the surface; both are enhanced by weathering, erosion, and transport of material. Blocks transport is suggested to be assisted by gravity, collapse into fractures, thermal cycling, and seismic activity (Thomas et al., 2001).
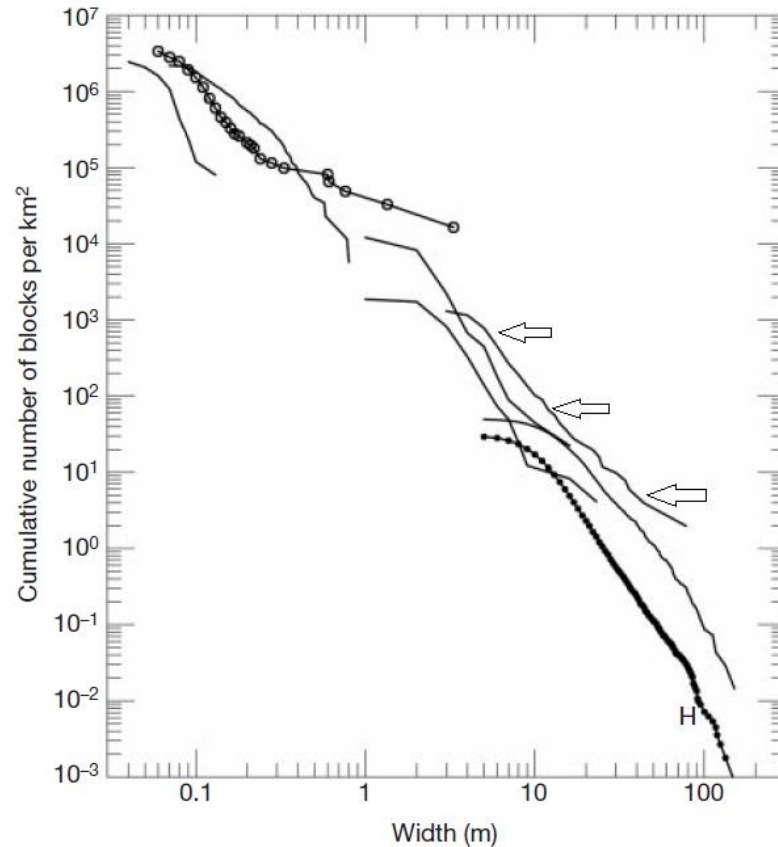
Figure (2.8): Block size frequencies on the surface of Eros. Cumulative numbers of blocks per unit area as a function of mean horizontal size (width). Arrows indicate global data size distribution with a slope of -3.2. Curves show resolution effects at lower size fractions (figure and caption extracted from Thomas et al., 2001).

The Martian satellite, Phobos, was photographed by approximately eight missions in the last four decades although the primary target for all the missions was Mars. Mars Global Surveyor' (MGS) four flybys of Phobos acquired imagery with resolution of ~ 2–

26

7 m/pixels, which were used to study the blocks size distribution over the entire surface (Thomas et al., 2000). They reported that most of the large blocks on Phobos are associated with the 9 km crater Stickney with ~ 90% of the mass of blocks located inside Stickney. The images showed ~2000 features, with the majority of them termed as blocks/boulders (Figure 2.9). Most of the blocks exhibited evidence of burial, weathering, or other aspects of degradation and some blocks blended together resulting in a "hummocky" appearance that might mislead in identifying them as separate blocks. The cumulative size distribution of the blocks on the entire surface produced a power-law relationship with an index of -3.2., which also falls within the range expected for ejecta blocks produced from excavation by high velocity impacts on airless bodies (Thomas et al., 2000).
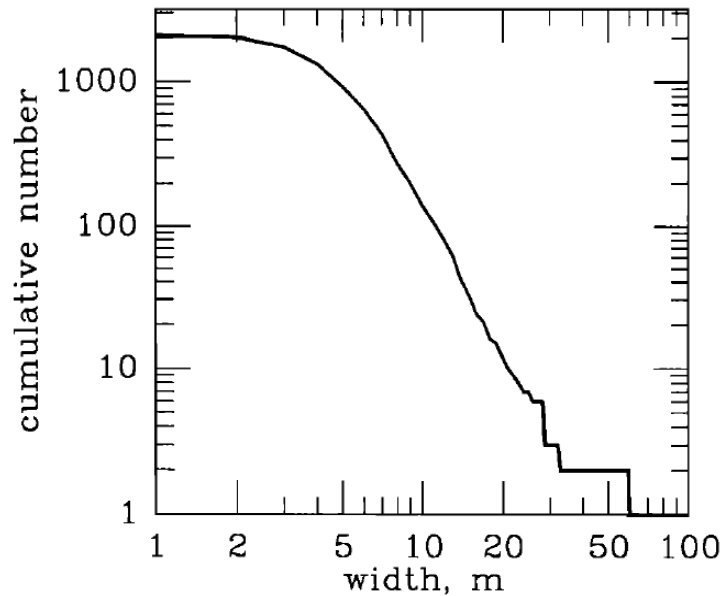
Figure (2.9): Plot shows a cumulative size distribution of the blocks on Phobos, where the size is defined as the width of the fragments/ boulders. The slope was found to be -3.2 (figure adopted from Thomas et al., 2000)

2.4 A Comparison between LL- chondrite and Carbonaceous Chondrite Lithology

2.4.1 Blocks on Itokawa

Asteroid 25143 Itokawa is a Mars-crosser S-type asteroid discovered in 1998 by the LINEAR (Lincoln Near-Earth Asteroid Research) project. Being an extremely small object (approximate mean diameter of 320 m and total surface area of 0.393 km^2), Itokawa is characterized by very low escape velocity (< 1 m/sec), and low bulk density (~1.95±0.13 gm/cc) that corresponds to a high macroporosity of 40 % indicating a rubble pile structure. It was selected as the first target of the sample return mission Hayabusa in 2000, and was successfully landed upon by Hayabusa spacecraft in 2005. The mission was successful in obtaining high resolution images of Itokawa and bringing back dust samples from the surface. Those returned dust particles were analyzed and confirmed the LL-chondritic composition proposed for Itokawa from its spectral data (Binzel et al., 2003; Nakamura et al., 2011; 2012).

Before the arrival of the Hayabusa mission to Itokawa' proximity, it was widely believed that there would be only a few boulders scattered on the surface. However, the surface proved to be covered by abundant prominent boulders. The Asteroid Multiband Imaging Camera (AMICA), on board the Hayabusa spacecraft, acquired high resolution images of most of the surface during the descent and touchdown phase on asteroid Itokawa (Fujiwara et al., 2006). Images of Itokawa showed that the surface was covered by a large number of boulders of different sizes (Fujiwara et al., 2006). Itokawa's surface provided many opportunities to study regolith features (Miyamoto et al., 2007), surface morphology (Noguchi et al., 2010), impact features (Nakamura et al., 2008), and blocks'

28

size, shape and spatial distributions (Michikami et al., 2010). The general shape of Itokawa have suggested that Itokawa might have formed because of a catastrophic disruption of its parent body and later reaccumulated to produce its present form (Fujiwara et al., 2006; Saito et al., 2006). Approximately 80% of Itokawa' surface is occupied by rough terrain characterized by large blocks and the remaining 20% is covered by relatively smooth terrain composed of comparatively fine-grained material (Michikami et al., 2008).
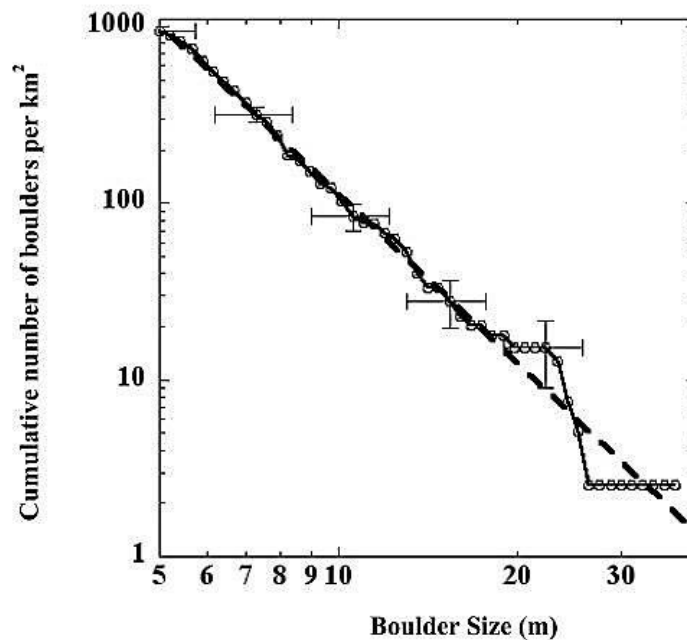
Figure (2.10): *Plot shows a cumulative size distribution of the blocks on Itokawa, where the size is defined as the mean horizontal dimension of the fragments/ boulders. The slope was found to be -3.1 (figure adopted from Michikami et al., 2008)*

The cumulative size distribution of blocks (boulders) was investigated by Michikami et al. (2008). They measured the mean horizontal dimensions of positive relief features larger than 5 m over the entire surface. Based on high resolution images (~

0.4 m/pixel) acquired by the AMICA, from a total number of 373 blocks larger than 5 m, they reported that the cumulative size distribution of the entire surface yields a power-law index of -3.1± 0.1 (Figure 2.10), which is within the range of size distribution found on other small airless objects such as Eros, Ida, Phobos and Deimos (e.g. Thomas et al., 2000; and references therein).

The size distribution of boulders on Itokawa was investigated for two purposes: (1) to gain a better insight on regolith behavior in different terranes, by comparing boulders size distribution within rough versus smooth terrains, and (2) as a proven representative of chondritic lithology for comparison purposes. For this, image (st_2532629277_v.fits) was selected from the Hayabusa descent and touchdown sequence with a resolution of ~0.1 m/pixel, which provided excellent details of three types of terranes with variable roughness (Figure 2.11). Muses-C area with its characteristic smooth terrain dominated most of the image, with occasional boulders scattered against the smooth background. Surrounding the Muses-C, were remarkably rough terranes with medium to large size boulders, and within the rough region to the northeastern side of the image there is the small (0.03 km-diameter) Komaba crater. The high resolution allowed the selection of four rectangular areas of ~170 m^2, two on typical rough terranes (Rough Terrane I and II) and two on the smooth regions (within Komaba crater and Muses-C).

Boulder populations ranged between 14 cm - 4 m in diameter, and a boulder's size was defined as the mean horizontal dimension of positive relief features (boulders) to enable the comparison with other studies. Using Smithsonian Astrophysical Observatory (SAO) astronomical imaging application DS9, boulders' dimensions were measured by

selecting the longest dimension of each boulder and the longest dimension perpendicular to it, and the mean value of these two dimensions was considered the mean horizontal dimension for each boulder. Since the measurements are based on a single image, there were some limitations in outlining all present boulders caused by the shadows, and the partial burial of boulders.

The cumulative size distribution per unit area was calculated for each of these rectangles yielding shallow slopes for the rough terrains (-1.63 and -1.32), and steeper slopes for the smooth terranes of Komaba crater (-3.33) and Muses-C (-3.06). Komaba crater yielded a slope that is within the uncertainty of that of Muses-C distribution; however, boulders within Komaba showed a relatively more restricted range of block sizes indicating that further processing of boulders have taken place on the surface as a result of impacts eliminating the larger size fragments and increasing finer block population (Figure 2.12).
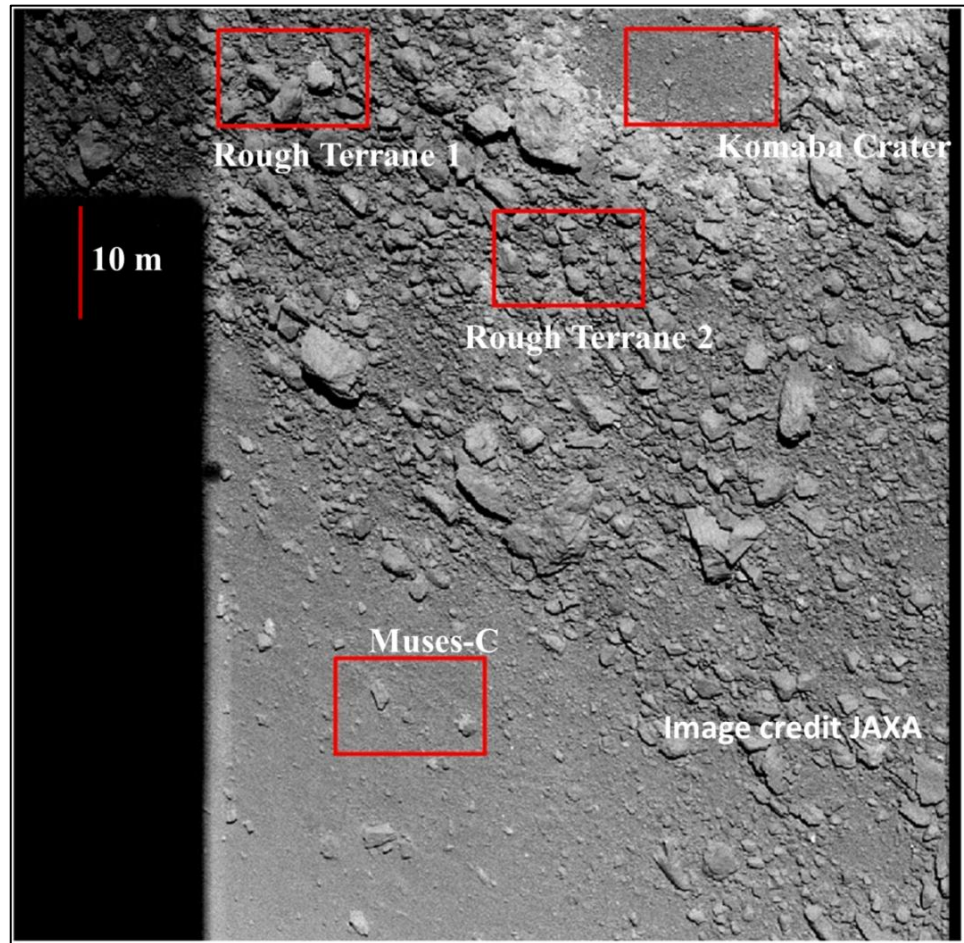
Figure (2.11): Image (st_2532629277_v.fits) from the descent and touchdown sequence with resolution of ~ 10 cm/pixel, with rectangular areas of ~170 m^2.
http://darts.isas.jaxa.jp/planet/project/hayabusa/data/amica/20051109/ST_2532629277_ v.jpg from the JAXA Hayabusa website accessed July 27th, 2012.

The second part of the study included an investigation of the shape distribution of boulders within the four regions, with focus on the smooth terranes (Muses-C and Komaba crater) by measuring the axial ratios of boulders. The shape distribution provides a measure of the boulders' uniformity and how effective are the surface processes such as impact craters and ejecta flows in controlling the global shape distribution of the regolith. To accomplish this, the obtained measurements of the two primary axes a, and b (the

32

third axis c represents the height of the blocks, which is perpendicular to our plane of view and therefore unobservable). The mean 'b/a' ratio yielded a mean value of 0.73 ± 0.03 for Komaba crater and 0.75 ± 0.03 for Muses-C region (Figure 2.13), and 0.70 ± 0.02 and 0.67 ± 0.03 for the rough terranes I and II, respectively. Despite the similarity in the mean "b/a" ratios for all those regions and particularly the smooth regions, the mode of Muses-c was 30% less than that found for the Komaba crater, which probably reflects a higher number of boulders that was measured in Komaba crater (see Appendix A for details).

2.4.2 Tagish Lake Size Distribution

Tagish Lake is an ungrouped carbonaceous chondrite, which fell and was recovered from Tagish Lake in Canada in 2000, with a recovered mass of ~10 Kg (Hildebrand et al., 2006). It is widely known as one of the most primitive and physically weak meteorites recovered to date, with a bulk density of 1.64 ± 0.02 g/cm^3 and corresponding microporosity of 40%. The calculated orbit for Tagish Lake rules out a cometary origin (Brown et al., 2000), and supported a main belt asteroid parent, possibly a D-type (outer main belt) or T-type (inner main belt) from their matching spectral signature (Hiroi et al., 2003).
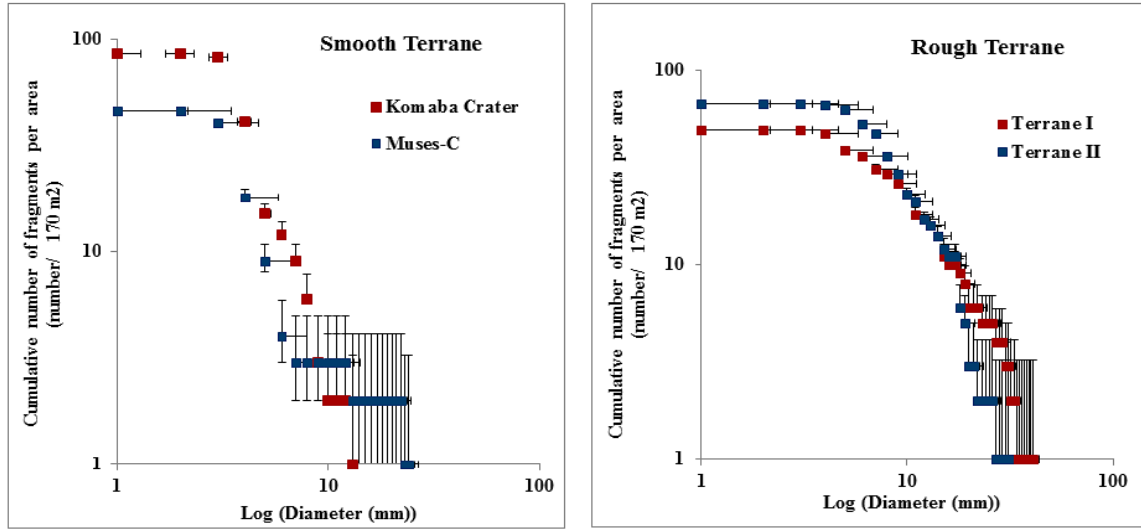
Figure (2.12): Plots show cumulative size distributions of the blocks on Itokawa, in which the size is defined as the mean horizontal dimension of fragments/ boulders. On the left side the smooth areas Muses-C and Komaba crater show slopes of -3.06 and -3.33, respectively. The right hand side shows two areas on the rough regions; rough terrane I exhibits a slope of -1.63 and rough terrane II a slope of -1.32. The vertical error bars are the square root of the cumulative number of fragments divided by the area, while the horizontal error bars are uncertainty in diameter measurement.
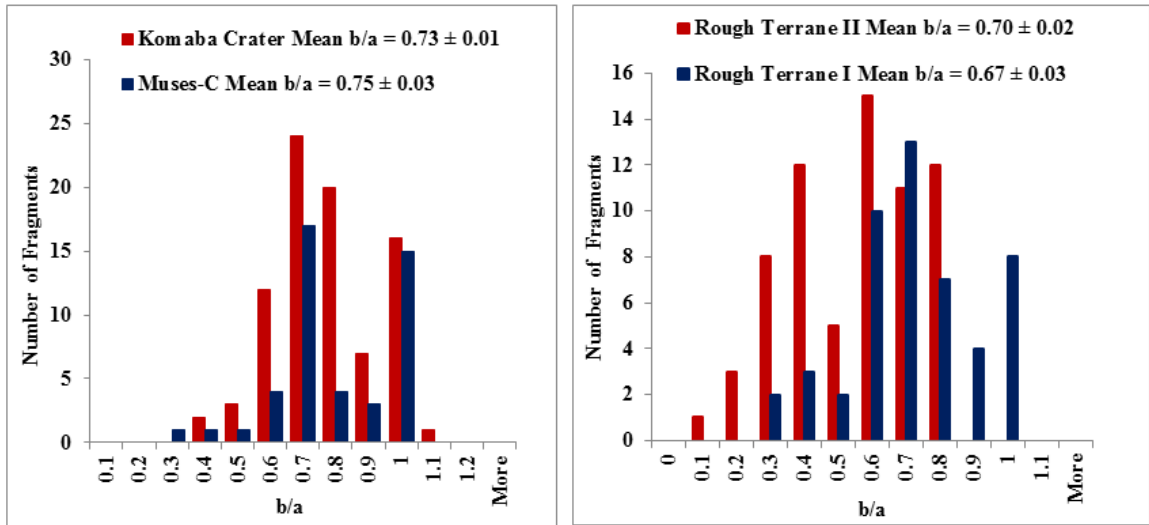
Figure (2.13): Histograms of the incremental shape distribution of fragments/ boulders on Itokawa. Shape is defined by the axial ratio "b/a" of the fragments.

34
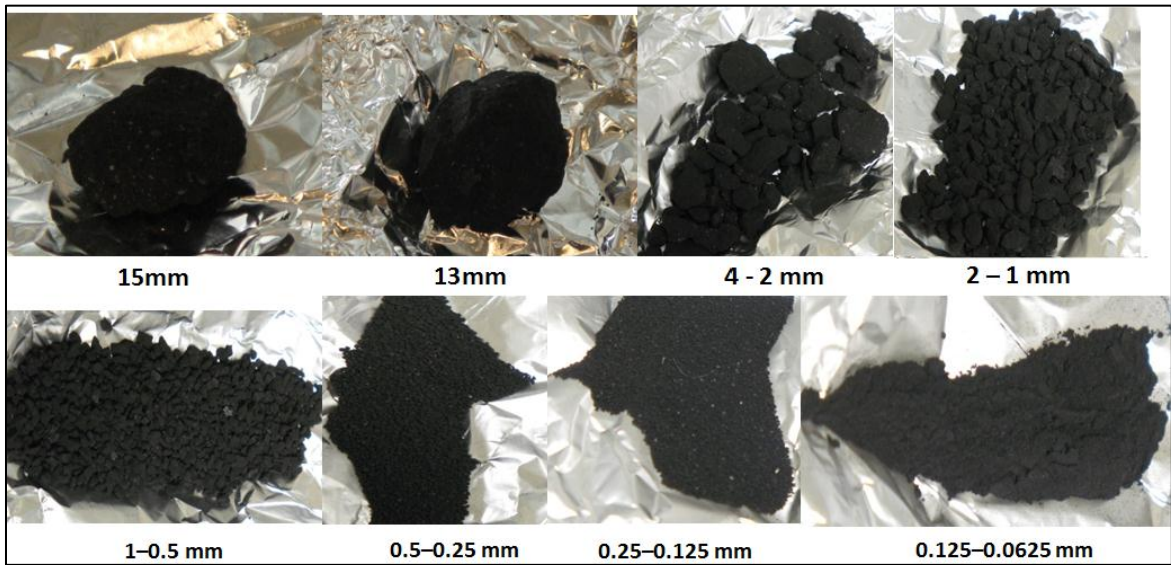
Figures (2.14): Images of a Tagish Lake sample (Sample EG-06) show the gradual change in particle sizes from 15mm, for which a digital caliper is used for measurements, down to powder-size material, which was passed through a clean set of metal sieves.

The weak physical strength of Tagish Lake and the weathering that it has experienced resulted in the rapid disaggregation of recovered samples, producing pieces of various sizes and shapes. The disaggregated samples of Tagish Lake available for study consisted of consolidated samples and powdered material (Figure 2.14). The consolidated portion of the samples included chips and fragments with size ranges between 2.4 cm – 28.1 mm, with a mean diameter of 8.9±0.4 mm; whereas, the powdered material required conventional sieving methods to be measured. The consolidated fragments of all samples together yielded 50 size measurements, where three perpendicular dimensions were averaged for each fragment, and the obtained mean diameters were used as the fragments' sizes and produced a size-frequency distribution

35

with a cumulative slope of -5.7. Note that, this size-frequency distribution was produced for a portion of each sample, and not the whole samples.

The analysis was constrained by the fragility of the fragments as well as the fact that most of the material was available as tiny chips to start with (< 5 mm) and powdery material. Since disaggregation of samples upon contact was very common, measurement of samples often resulted in producing newer "chips" and more powder, which resulted in more fine material. However, it was remarkable that at certain size ranges (2 − 3 mm in diameter), fragments show more resistance to breakup. This prompted the use of conventional sieving methods to address the measurement of the powdered material, which impossible to measure with a caliper. Unlike the case with caliper measurements, sieving does not provide a direct measurement of the fragments diameters, but size is assigned from aperture size. A new and thoroughly cleaned wire-screen set of sieves ranging between 4 mm − 0.0625 mm was used to sieve the total mass (fragments and powder) for 11 samples of Tagish Lake resulting in a mass *versus* size distribution (mass of material for a certain size range (gm) plotted against size ranges (mm). The total mass *versus* size distribution was calculated for the whole range of samples, producing a slope of -1.04 for the total mass of samples and a mean slope of -1.12 from averaging values for each sample (Figure 2.15).

The size-frequency distribution of the consolidated portion of the samples is plotted as the number of fragments with a diameter greater than a certain diameter (D) *versus* size of fragments (mm). In order to produce a size-frequency distribution for the whole population, it will be necessary to calculate a factor to convert between the different types of distributions. This was attempted by correlating the mass *versus* size

slope for the consolidated fragments to the size − frequency distribution slope obtained for the same portion. This produced a factor of 3.15 to convert from mass-size to size-frequency distribution, which coincides with the factor reported by Hartmann (1969). Hartmann (1969) mentioned that assuming a constant density of the fragment population, and based on the fragment radius $r \propto m^{\frac{1}{3}}$ where m is the mass of the fragment, then:

$$b = \frac{\beta}{3} \qquad (2.5)$$

Where b is the slope of the cumulative size-frequency distribution and β is the slope of the mass *versus* size distribution. The discrepancy between the two factors (5%) might be attributed to the uncertainty in the measured cumulative size-frequency distribution. The size distribution of the whole population was calculated using this factor between the two forms of distribution yielding a mean slope of - 3.39 ± 0.18 per sample, and a slope of -3.55 ± 0.18 for the whole population of samples treated as one sample.

Shape distribution analysis was possible to obtain for the 50 fragments measured at the start of the study. The longest three perpendicular dimensions of each fragment were used to calculate the axial ratios c/a, c/b and b/a yielding mean values of c/a = 0.51 ± 0.01, c/b = 0.76 ± 0.01, and b/a = 0.53 ± 0.01 (Figure 2.16).
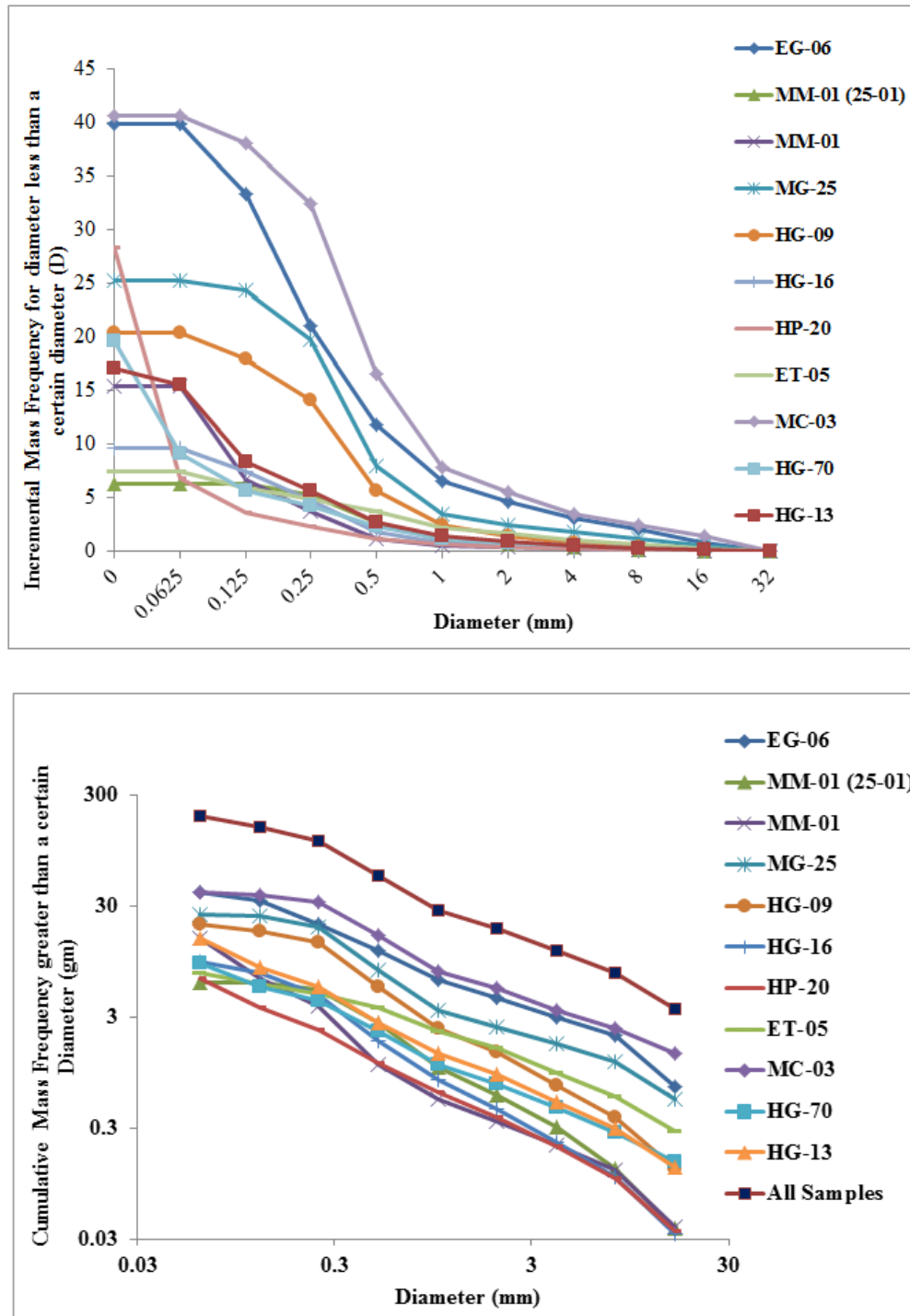
Figure (2.15): Incremental (Top) and Cumulative (Bottom) mass-frequency distribution versus fragment sizes of Tagish Lake meteorite samples. The mean power-law index for the samples is -3.39 ± 0.18, and -3.55 ± 0.18 per the whole fragments population treated as one sample.
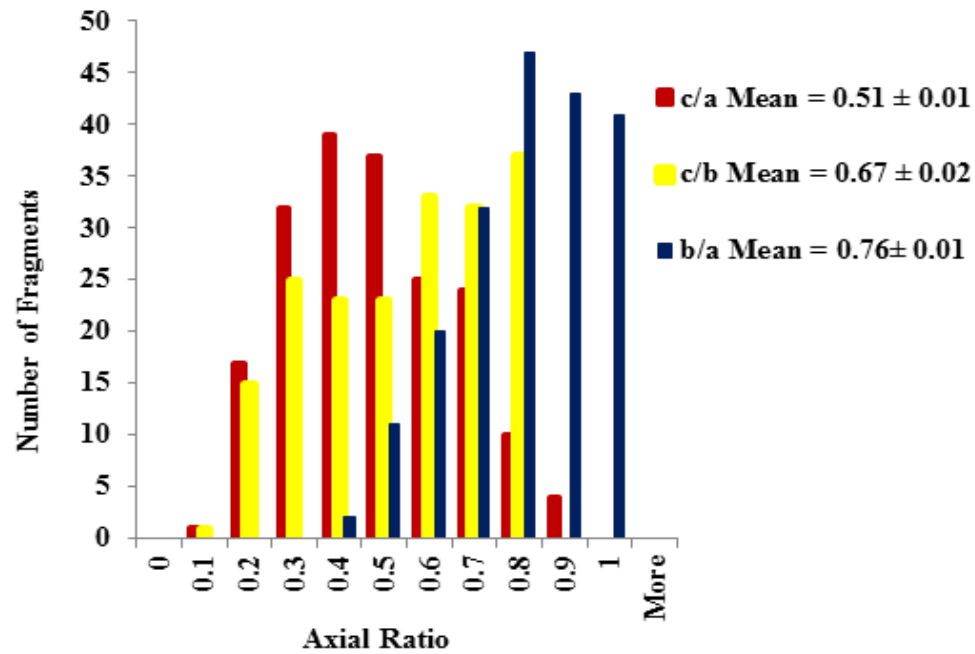
Figure (2.16): Shape distribution of fragments of Tagish Lake meteorite in lab observations.

The shape of Tagish Lake fragments, that were measured via caliper, were irregular in general, with no obvious pattern of sphericity variation versus size. A closer look at the axial ratios obtained shows the majority of the fragments were prolate fragments (a > c), which is entirely a selection effect.

2.4.3 Conclusions

The size distribution of asteroids, impact ejecta (boulders) on their surfaces and meteorites are determined by collisional processes and the response of these objects to fragmentation. The size distributions of asteroids show that the products of collisional fragmentation follow a power-law fit, which is consistent with a number of theoretical models (e.g. Williams and Wetherill, 1994; O'Brien and Greenberg, 2003).

This chapter summarized the size distribution of some planetary objects (asteroid families, near-Earth asteroids and boulders on asteroids). The aim was to provide a background for the size distribution power-law index over a wide range of diameters (sub-meter to hundreds of kilometers in diameter). The behavior observed across those sizes suggests that impact cratering on low-gravity bodies produces self-similar fragment size distributions (Table 2.2).

Images acquired from S-type asteroids Eros, Ida and Itokawa (ordinary chondrite lithologies) show various sizes of boulders on the surfaces of these asteroids around craters of comparable sizes; whereas, images of C-type asteroid Mathilde showed a remarkable lack of boulders around giant impact craters that are comparable to the size of Mathilde. Compaction has been suggested as the mechanism that allowed for such craters without the breakup of Mathilde (Housen et al., 1999). Lithology's influence can be studied through a comparison of the size distribution of two (or more) lithologically different objects; such as asteroid Itokawa (LL-chondrite) and Tagish Lake (Carbonaceous chondrite).

The size distributions of boulders on Itokawa yielded a size distribution with mean slopes of -3.3 for the smooth regions and -1.48 for the rough regions. Komaba crater showed a slightly steeper slope and narrower size range than that of the Muses-C region where abundant fine material collected, indicating that impact-induced fracturing and intra-cratering flows apparently eliminate larger fragments and resulting in a more uniform size distribution consistent with observed terrestrial erosion processes.

Tagish Lake meteorite samples produced a significantly steeper slope for the cumulative size distribution compared to Itokawa terranes. The steeper slope produced by Tagish Lake implies easier fracturing and enhanced regolith generation on similar lithologies. It also reflects the lower strength of the hydrated carbonaceous lithologies (typical of other similar meteorite lithologies such as CI and CM) compared to Itokawa and meteorite fall fragments. As well, Itokawa's rough terrane showed a much shallower size distribution of the boulders compared to the overall size distribution found on Eros and Ida, which indicates less processing on Itokawa's surface compared to those asteroids.

Region	Diameter Range (m)	Number of objects	Observed Slope
Outer Belt	$1 \times 10^3 \leq D \geq 28 \times 10^3$	16,309	-2.7
Middle Belt	$1 \times 10^3 \leq D \geq 35 \times 10^3$	14,261	-3.0
Inner Belt	$1 \times 10^3 \leq D \geq 38 \times 10^3$	9547	-3.3

Family	Diameter Range (m)	Number of members	Observed Slope
Vesta	$1 \times 10^3 \leq D \leq 14 \times 10^3$	3793	-3.8
Themis	$1 \times 10^3 \leq D \leq 31 \times 10^3$	1073	-2.0
Koronis	$1 \times 10^3 \leq D \leq 39 \times 10^3$	1267	-2.08

Object	Diameter Range (m)	Number of Fragments	Observed Slope
Eros	$0.1 \leq D \leq 15$	33,939	-3.2
Ida	$30 \leq D \leq 150$	17	-3.0
Itokawa	$D \geq 5$	373	-3.1
Muses-C (Itokawa)	$0.14 \leq D \leq 2.3$	46	-3.1
Komaba Crater (Itokawa)	$0.14 \leq D \leq 1.2$	85	-3.3

Table (2.2): Shows the size distribution of some planetary objects ranging from asteroid families down to boulders on asteroids.

Chapter Three: The Elastic Properties of Carbonaceous Chondrites

3.1 Introduction

3.1.1 Background

Carbonaceous Chondrites were defined as a group of meteorites formerly typed together based on their dark matrices and substantial carbon content excluding the free carbon in the form of graphite and diamond in their composition (Mason, 1963; McSween, 1979). The term "carbonaceous" has since been recognized as a misnomer as most carbonaceous chondrites have been found to have similar carbon content to that found in many ordinary and enstatite chondrites, and some carbonaceous chondrites show low abundance in carbon (Weisberg et al., 2006). The current and most accurate basis of chondrites classification is their refractory lithophile elements (RLE) abundances (Figure 3.1), according to which, carbonaceous chondrites are characterized by having the highest abundances of RLE amongst chondrites (Rubin, 2011).

Besides using whole-rock petrologic analysis, as one of the most common ways to classify meteorites, oxygen isotope analysis provides a unique criterion to determine relationships amongst meteorite groups based on the position of each group on the three-isotope oxygen plot (Weisberg et al, 2006; and references therein). Carbonaceous chondrites plot near or below the terrestrial fractionation line (Figure 3.2); whereas, ordinary chondrites plot above the terrestrial fractionation line (Clayton, 2005).
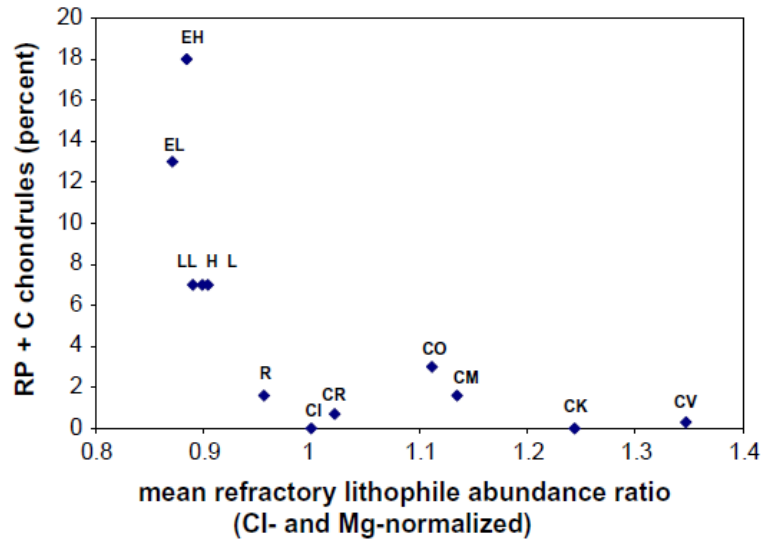
Figure (3.1): Proportion of Radial pyroxene RP + cryptocrystalline C chondrules versus mean refractory-lithophile abundances in different chondrite groups. The correlation shows that the carbonaceous chondrites acquired their high RLE contents in dustier zones of the solar nebula. Although plotted on the diagram, chondrules are absent in CI chondrites (Figure and caption adopted from Rubin, 2011).
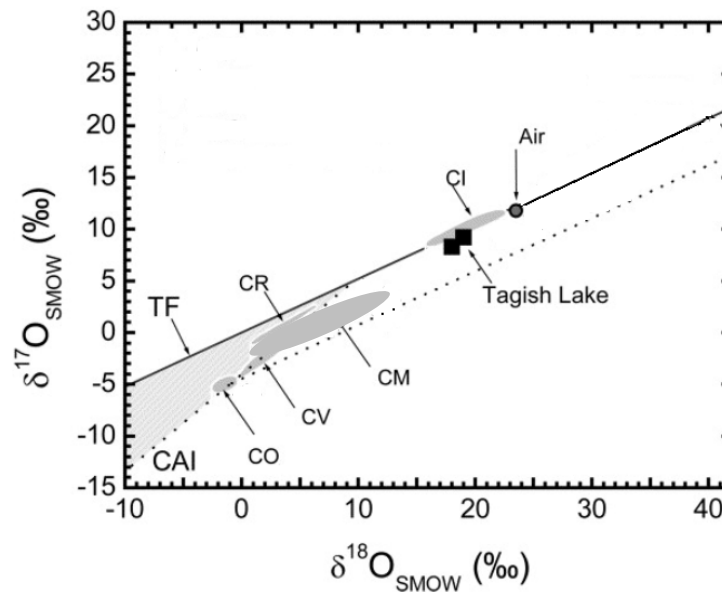
Figure (3.2): Oxygen isotope abundance of some carbonaceous chondrites groups from Clayton and Mayeda (1999) and Tagish Lake from Brown et al. (2000) modified from Taylor et al. (2004).

In the current meteorite collection, carbonaceous chondrites are relatively low in abundance with about 500 non-Antarctic carbonaceous chondrites and only 44 observed falls to date (Meteoritical Bulletin, accessed June 2012). The first recorded fall occurred near Alais in France (1806), fortunately after the notion that "stones falling from the sky" became credible, and the most recent one as of this writing in California fell in the United States on the 22nd of April 2012 (Meteoritical Bulletin, accessed July 2012). Meteorite falls occur at irregular intervals with no observed pattern of fall times or geographic distribution (Table 1). This low proportion of total falls by carbonaceous chondrites, ~4% of the total meteorite fall population, is believed to be largely due to their weak structure and high friability that reduce their survival of atmospheric entry. Despite this rarity, carbonaceous chondrites are highly sought after because of their status among of the most primitive meteorites (Figure 3.3), exotic mineralogy and chemical criteria, and evidence of undergoing aqueous alteration (McSween, 1979). Carbonaceous chondrites' appearance is often confused with that of coal or lumps of black clay with their dull to dark black color, low bulk density, high friability and lack of visible Ni-Fe alloys. Their weak nature restricts conducting physical analysis on them for concerns about damaging samples.
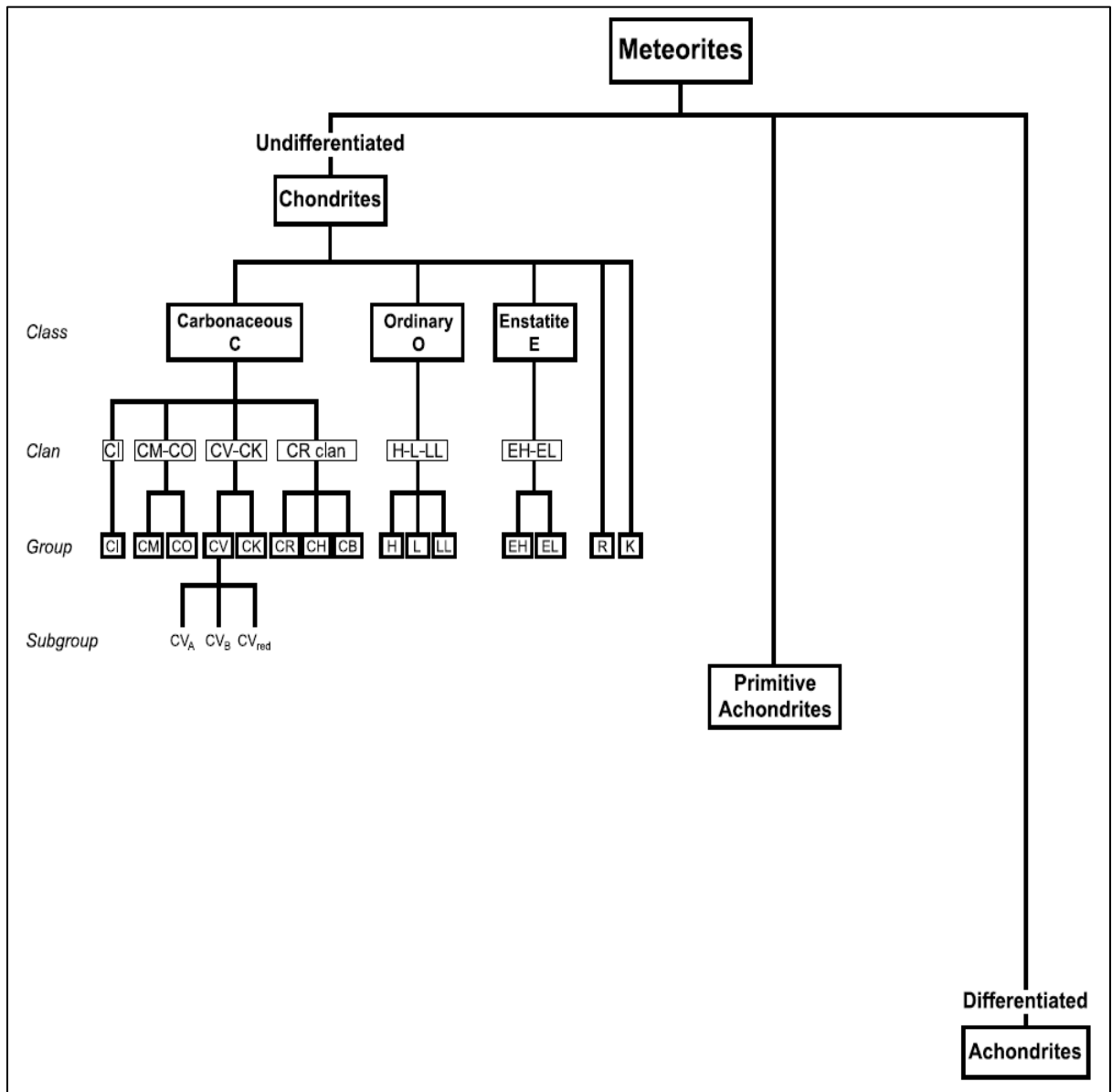
Figure (3.3): An illustration of the current classification of meteorites showing the major meteorite divisions, classes, clans, and groups (extracted from Weisberg et al., 2006). Carbonaceous chondrites are a class under Chondrites with five clans, eight groups and three subgroups.

Name	Year	Place	Type	Mass
Bell	1961	Texas, USA	C2-ung	375 g
Essebi *	1957	Haut-Zaire, Congo - Dem. Rep.	C2-ung	500 g
Tagish Lake *	2000	British Columbia, Canada	C2-ung	10 kg
Ningquiang	1983	Shaanxi, China	C3-un	4.61 kg
Gujba	1984	Yobe, Nigeria	CBa	100 kg
Alais *	1806	Languedoc-Roussillon, France	CI1	6 kg
Ivuna *	193	Mbeya, Tanzania	CI1	705 g
Orgueil *	1864	Midi-Pyrenees, France	CI1	14 kg
Revelstoke *	1965	British Columbia, Canada	CI1	1 g
Tonk *	1911	Rajasthan, India	CI1	7.7 g
Karoonda	1930	South Australia, Australia	CK4	41.73 kg
Kobe *	1999	Kinki, Japan	CK4	136 g
Banten	1933	Jawa Barat, Indonesia	CM2	629 g
Boriskino	1930	Orenburgskaya oblast', Russia	CM2	1342 g
Cold Bokkeveld	1838	Western Cape, South Africa	CM2	5.2 kg
Crescent	1936	Oklahoma, USA	CM2	78.4 g
Erakot *	1940	Madhya Pradesh, India	CM2	113 g
Haripura *	1921	Rajasthan, India	CM2	315 g
Maribo *	2009	Region Sjaelland, Denmark	CM2	25.8 g
Mighei	1889	Nikolayev, Ukraine	CM2	8 kg
Murchison	1969	Victoria, Australia	CM2	100 kg
Murray	1950	Kentucky, USA	CM2	12.6 kg
Nawapali	1890	Orissa, India	CM2	105 g
Nogoya	1879	Entre Rios, Argentina	CM2	4 kg

Name	Year	Place	Type	Mass
Pollen	1942	Nordland, Norway	CM2	254 g
Santa Cruz	1939	Tamaulipas, Mexico	CM2	60 g
Sayama *	1986	Kanto, Japan	CM2	430 g
Kainsaz	1937	Respublika Tatarstan, Russia	CO3.2	200 kg
Felix	1900	Alabama, USA	CO3.3	3.2 kg
Ornans	1868	Franche-Comte, France	CO3.4	6 kg
Lancé	1872	Centre, France	CO3.5	51.7 kg
Moss	2006	Ostfold, Norway	CO3.6	3.76 kg
Warrenton	1877	Missouri, USA	CO3.7	1600 g
Kaidun *	1980	Hadhramaut, Yemen	CR2	2 kg
Renazzo	1824	Emilia-Romagna, Italy	CR2	1000 g
Al Rais	1957	Al Madinah, Saudi Arabia	CR2	160 g
Allende	1969	Chihuahua, Mexico	CV3	2 MT
Bali	1907	Nana-Mambere, Central African Rep.	CV3	1000 g
Bukhara *	2001	Bukhara, Uzbekistan	CV3	5.3 kg
Grosnaja	1861	Chechenskaya Respublika, Russia	CV3	3.5 kg
Kaba	1857	Hajdu-Bihar, Hungary	CV3	3 kg
Mokoia	1908	Taranaki, New Zealand	CV3	4.5 kg
Vigarano	1910	Emilia-Romagna, Italy	CV3	15 kg

Table (3.1): shows the total carbonaceous chondrites falls recorded worldwide to date (Extracted from the Meteoritical Bulletin, last access July 06th, 2012).

* Samples not included in this study, including the fragile CI-chondrites.

3.1.2 Rationale and Objectives

Impact processes have touched every aspect of planetary evolution, from accretion of dust or planetesimals to disruption of planetary objects. Asteroids' distal responses to collisions are governed by their control of impact-generated shock and elastic waves; wave propagation and attenuation throughout the asteroid. In turn, elastic and shock wave behavior is dictated by the internal structure, micro and macro porosity and the elastic moduli of asteroids (Consolmagno et al., 2006). These elastic properties could be modified by impact processes occurring on asteroid surfaces due to the introduction of new macro porosity (fractures and pore spaces) or reducing existing porosity because of compaction (Consolmagno and Britt, 2002; Housen et al., 1999).

Meteorites are the only available physical representatives of asteroids on which elastic properties can be measured. Meteorites' elastic properties are fundamental in understanding the physical nature of their parent bodies as they provide some constraint on the theoretical modeling of asteroids' responses to impact processes. Until recently a data gap existed on meteorites' elastic properties with only a couple of studies in the last two decades (Yomogida and Matsui, 1982; Flynn et al, 1999) and two systematic surveys on the elastic properties of ordinary chondrites (Jones, 2008; Hons, 2004).

Carbonaceous chondrite classes have experienced variable degrees of aqueous alteration and/or low thermal metamorphism making their lithologies rather exotic and interesting to investigate. Additionally, with at least two missions scheduled to fly to C-type asteroids within the next five years; e.g., *Hayabusa 2* to asteroid (162173) 1999 JU3

expected to launch in July 2014 (Abe et al., 2012), it useful to acquire the readily accessible data on the elastic properties of carbonaceous lithologies.

Despite the extensive aqueous alteration processes that affected some of the carbonaceous chondrites, they have retained bulk compositions that are close to that of the solar photosphere for many elements (Brearley, 2006). Previous physical property investigations reported high porosity and low bulk density values for carbonaceous chondrites compared to those of the ordinary chondrites (Britt et al., 2002), suggesting different elastic properties for the carbonaceous chondrites; therefore, the main objective of this study is to measure the carbonaceous chondrites' elastic properties. The second objective of this study is to examine the relationships amongst elastic and physical properties of carbonaceous chondrites and their implications on their parent bodies' impact rates and physical strength.

3.2 Elastic Property Measurement

3.2.1 Theory

Materials subjected to any external force will either react by moving away from the force; such as in the case of liquids or internal forces arise within the material to oppose these external forces, which is characteristic of solids. The amount of force applied is an important aspect in studying materials' behavior. Stress (σ) is the amount of force applied per unit area, usually measured in Pascal ($Pa = N/m^2$) or high multiples such as megaPascals (MPa) and gigaPascals (GPa) for geological materials subject to impact. Any material undergoing stress shows change in dimensions, referred to as strain

ε, which is the ratio of the new to the original dimension; therefore, it has no unit and is expressed instead as a ratio in percentage.

According to Hooke's law of elasticity, most materials undergo extension (strain) in direct proportion to the applied load (Stress) as long as the load does not exceed the material's elastic limit. These materials are described as "elastic". In geology, rocks obey Hooke's law and exhibit a linear relationship between stress and strain up to a certain limit (Burdine, 1963); they start deforming permanently (plastic behavior) and finally break at their yield point (Figure 3.4).

The terms "maximum tensile strength" and "maximum compressive strength" that are commonly used to describe materials' mechanical properties, denote the maximum values of tensile and compressive stress, respectively, that a material can withstand prior to failure. Whereas, maximum shear strength is the maximum stress that a material can experience in shear before it fails. Those strengths are calculated at the maximum forces applied divided by the original cross-sectional area.

A different way to express materials' mechanical behavior is through their elastic moduli. The elastic moduli are mathematical descriptions of materials' tendencies to deform elastically when forces are applied. Measuring stress and strain along three axes allows for calculating different elastic moduli; however, for our purposes, we used elastic wave velocity and bulk density values to extract elastic moduli values, by applying non-destructive techniques. All elastic moduli have units of stress (strain has no units) in Gigapascals.
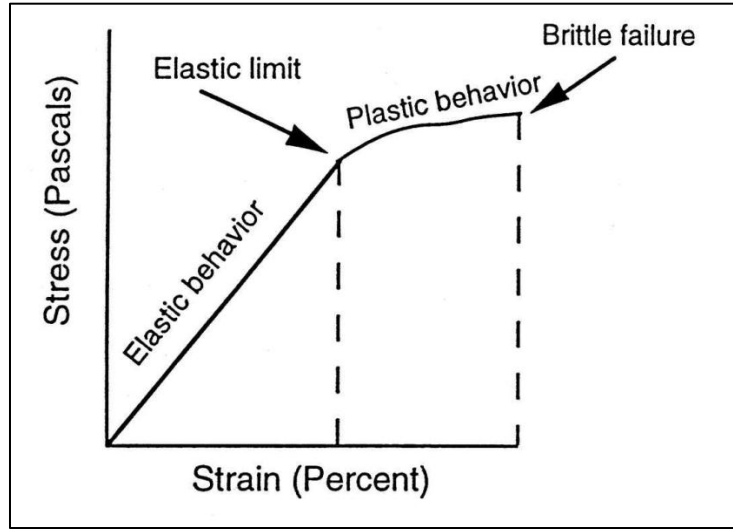
Figure (3.4): Materials when subjected to moderate stresses, the strain is proportional to stress, and the material deforms elastically. At higher stresses, where the elastic limit is exceeded, the material deforms plastically (ductile behavior). At even higher stresses, the yield strength is exceeded, and the material breaks by brittle failure (Hamburger, 2000).

Young's modulus (E)

     Young's modulus or modulus of elasticity describes the tensile elasticity or the tendency of the material to deform along an axis when opposing forces are applied along that axis, and is given by the tensile stress to tensile strain ratio:

$$E = \frac{\sigma}{\varepsilon} \qquad\qquad (3.1)$$

$$E = \rho_{Bulk} * V_E \qquad\qquad (3.2)$$

Where σ *is* tensile stress, ε is the tensile strain, ρ_{Bulk} is bulk density and V_E is calculated from the shear wave velocity V_s and Poisson' ratio ν using

$$V_E = 2 * V_s^2 * (1 + \nu) \qquad (3.3)$$

Shear modulus (μ)

Shear modulus is used to describe a material's tendency to shear when opposing forces act on two opposite surfaces. Similar to Young' modulus, shear modulus is the shear stress to the shear strain ratio in a linear relationship between stress and strain:

$$\mu = \frac{\tau}{\gamma} \qquad\qquad (3.4)$$

Where Shear stress $\tau = \frac{F}{A}$ and the shear strain $\gamma = \frac{x}{L} = \tan\varnothing \approx \varnothing$ (inclination angle)

When applying shear stress, the material twists, one face slides relative to an opposite face, or angular change in dimension takes place. Shear modulus is calculated using:

$$\mu = V_s^2 * \rho_{Bulk} \qquad\qquad (3.5)$$

Bulk modulus (K)

Bulk modulus describes the volumetric elasticity or the tendency of a material to deform in all directions when uniformly loaded from all directions. It is defined as the volumetric stress to volumetric strain ratio; thus, bulk modulus can be described as the resistance of the material to compressibility. The bulk modulus is an extension of Young's modulus to three dimensions, and can be calculated from P- and S-wave velocities (Vp and Vs respectively), and the bulk density ρbulk :

$$K = \rho_{Bulk} * \left(V_p^2 - \frac{4}{3} * V_s^2 \right) \qquad (3.6)$$

Poisson' ratio (*v*)

Poisson's Ratio (v) is a measure of the Poisson's effect, it describes the tendency of materials to expand in the two directions perpendicular to the direction of compression and vice versa; i.e. it reflects the behavior material in terms of the ratio of longitudinal to

53

transverse strain when stressed in the longitudinal direction (Hons, 2004; and references therein). As well, Poisson' ratio affects the propagation and reflection of stress waves, and the decay of stress with distance; and also the Vp/Vs ratio.

$$\nu = \frac{V_p^2 - 2 * V_s^2}{2 * (V_p^2 - V_s^2)} \qquad (3.7)$$

Another modulus is Lame's first parameter, which is useful in calculating and modeling some aspects of material deformation, such as anisotropy, and pore fluids and is given by:

$$\lambda = K - \frac{2}{3} * \mu \qquad (3.8)$$

3.2.2 Previous work

During the last two decades, a number of studies have been conducted on the physical properties of meteorites (e.g. Macke et al., 2010a; 2010b; Consolmagno and Britt, 2000). The most recent and comprehensive study of meteorites densities and porosities was conducted by Macke et al. (2010), as an extensive survey of carbonaceous meteorites' physical properties, in which they measured the grain and bulk densities, porosity and magnetic susceptibility of 196 samples of 63 carbonaceous chondrites. This survey is by far the largest systematic study conducted on carbonaceous chondrites to date and included 29 fall samples of the total 49 carbonaceous chondrite fall population. Earlier surveys that included carbonaceous chondrites as part of the studied population were primarily conducted by Britt and Consolmagno throughout the last decade. These surveys reported remarkable differences between aqueously altered carbonaceous chondrite groups CM and CI and anhydrous groups CO, CV, and CK in terms of bulk density values. Hydrated carbonaceous chondrites exhibited low to very low bulk and

grain density and higher porosity than non-hydrated groups; however, there was no emphasis on observed trends amongst the studied physical properties, probably caused by the lack of enough samples.

Published literature on meteorites' elastic properties is limited to a handful, with only a few measurements of carbonaceous chondrites' elastic properties to date. This is believed to be caused by the specialized equipment required and/or the limited number of samples suitable for such measurement in terms of size and shape. In addition, there is the reluctance of meteorites' curators to allow access to their carbonaceous chondrite collections since any type of physical measurements pose as "threat" to their samples; especially elastic property measurements that are often obtained through destructive techniques. Generally, measurements of physical properties, especially the elastic properties, require samples' sizes that are usually larger than the sizes required for chemical and petrologic studies.

A compilation by Petrovic (2001) summarized mechanical property literature for the stony meteorites and their main mineral components; olivine and pyroxene (Table 3.2). However, since these two minerals occur at low pressure – low temperature conditions on asteroids, the elastic moduli and mechanical strength values that were studied at high confining pressure – high temperature conditions do not necessarily apply to asteroidal environments. Moreover, there are other factors that affect the whole-rock elastic moduli for meteorite samples, such as the presence of other mineral phases in the meteorite and the percentage of olivine and pyroxene, mineral packing and orientation, grain size and grain boundaries, porosity and bulk density, deformation due to shock, temperature and brecciation.

Mineral	Chemical Formula	Crystal Structure	Density (gm/cm^3)	Elastic Modulus (GPa)	Shear Modulus (GPa)	Compressive Strength (MPa)	Tensile Strength (MPa)
Forsterite	Mg_2SiO_4	Orthorhombic	3.213	204	82.2	80	9.5
Fayalite	Fe_2SiO_4	Orthorhombic	4.393	140	52.9	—	—
Enstatite	$MgSiO_3$	Orthorhombic	3.209	180	74.6	—	—
Ferrosilite	$FeSiO_3$	Orthorhombic	3.900	—	—	—	—

Table (3.2): A summary of the mechanical properties of olivine (Forsterite and Fyalite) and pyroxene (Enstatite and Ferrosilite) extracted from Petrovic (2001).

Previous measurements of the elastic properties of meteorites were mostly done on ordinary chondrites, since they are more numerous and therefore more accessible than other classes of meteorites. Alexeyeva (1958; 1960) made the first attempts at studying physical properties of meteorites including their elastic properties. She measured bulk density, porosity, elastic wave velocity, thermal conductivity, specific heat and magnetic susceptibility. Ever since, a few studies were conducted on the elastic properties. This was motivated by the acquisition of lunar samples by the Apollo missions (e.g. Kanamori et al., 1970), and the discovery of meteorites in Antarctica (e.g. Yomogida and Matsui, 1980; 1981; 1982). Yomogida and Matsui (1983) expanded their investigation of the elastic properties to include non-Antarctic meteorites by measuring the elastic wave velocity and calculating the elastic moduli of three H-chondrites, seven L-chondrites and one carbonaceous chondrite (CV3 Allende). They observed a strong correlation between the elastic properties of ordinary chondrites and the porosities, the elastic properties and thermal properties, and that terrestrial weathering has no significant effect on physical properties. The latter trend was investigated by Hons (2004) in an elastic property survey

of stony meteorites classes, in which he reported a strong correlation between the length of terrestrial residence and grain and bulk density, which consequently influenced the elastic wave velocity. Moreover, a recent survey of ordinary chondrites by Jones (2009) showed that meteorite falls exhibit a reduction in grain density with increased terrestrial weathering time accompanied with an increase in bulk density. In addition, ordinary chondrite falls older than 100 years show scatter in the elastic wave velocity data relative to falls younger than 100 year, suggesting that terrestrial residence inside or outside curation facilities will still affect the bulk composition of meteorites. This was attributed to the formation of new phases of Fe-rich minerals that are more stable in terrestrial conditions (Jones, 2009), and these phases might have lower grain densities than the original minerals. The formation of these new minerals increases the bulk density by filling pore spaces and reducing the porosity.

Yomogida and Matsui (1983), in addition to measuring elastic wave velocities, derived theoretical values for the elastic wave velocities, bulk density and grain density from the normative mineral compositions. Their model values exceeded the measured values significantly, which was justified by the presence of cracks and higher porosity found in meteorite samples.

Elastic property data on carbonaceous chondrites were not sufficient enough to derive any statistically significant trends in any previous study (e.g. Jones, 2009; Hons, 2004). However, both studies observed several trends of elastic properties among the ordinary chondrites that provided a baseline for this study. The reported average trends from Hons (2004) could be summarized as follows: (1) elastic wave velocities increase and the porosity decreases with terrestrial weathering time (2) elastic wave velocities

increase with meteorite bulk density, (3) elastic wave velocities decrease with metamorphic grade/ petrologic type in ordinary chondrite fresh falls, (4) elastic wave velocities increase with meteorite darkness in ordinary chondrites, (5) elastic wave velocity decrease as average porosity increases. Jones (2009) confirmed those trends and added that on average: (6) bulk density decreases with terrestrial weathering time, (7) total porosity decreases with increasing shock state in H- and L-chondrites, (8) bulk density increases with petrologic type in H-chondrites, (9) Poisson's ratio and Vp/Vs ratio decrease with increasing petrologic type in H-chondrites and (10) Poisson's ratio and Vp/Vs ratio may decrease with increasing the porosity.

3.2.3 Methodology and Uncertainty

3.2.3.1 Sample Selection

Ideally, fresh samples returned from asteroids' surfaces (or interiors) would be the optimum for any type of analysis; however, in the absence of such samples in reality, meteorite "falls" are suitable samples. Falls have relatively well documented recovery circumstances, and they have well known terrestrial weathering time and curation conditions. While some meteorite finds might be unique samples, because of their unconstrained exposure to terrestrial weathering for undetermined lengths of time reduces the level of confidence about their original physical property state. This study selected carbonaceous chondrite falls only (of suitable size and shape).

Three meteorite collections were selected for measurements based on sample abundance of CC falls with the required specifications (Table 3.3). Most of the samples were available at the Natural History Museum collection in London, and the rest were

measured at the American Museum of Natural History in New York, and the Smithsonian Meteorite Collection at the National Museum of Natural History in Washington.

Measurements were conducted onsite applying non-destructive measurement techniques; measurement of ultra-sonic waves travel times through the sample combined with sample thickness obtained by a digital caliper were used to determine elastic wave velocities, and a modified Archimedes method was used to calculate samples' volumes necessary to determine their bulk densities. The total number of samples was 49 samples of 28 carbonaceous chondrite falls (Table 3.1); both velocity and density measurements were produced for 45 samples while elastic wave velocity was measured for all available samples.

Previous work recommended slabs of meteorites to ensure the best coupling at sample-transducer surface to produce robust signals (Hons, 2004). More than half of the sample populations were slabs, 40% were semi-slabs with one smooth surface, and the remaining two samples were non-slabs that were still suitable to measure. Ultrasonic contact transducers require optimally a surface area on the sample that is slightly larger than the diameter of each transducer, which constrains the number of suitable samples to measure. Thus, slabs of carbonaceous chondrites of ~ 1cm in diameter or larger reduced the population available for this analysis significantly. CI-carbonaceous chondrites extremely friable structure excluded them from measurement to avoid the risk of damaging the few available samples.

Meteorites	*Carbonaceous Chondrites*
Classes	All available classes
Number of samples	All available samples
Form	Slabs (priority) – non-slaps (minor option)
Minimum size	~ 1 x 1 cm
Special preparations	None
Effects on samples	None
Justification for sample form and Size	Velocity measurements require good contact between the ultrasonic transducers and the sample surface, which makes <u>slabs</u> with parallel sides, the optimum form for measurements and a diameter of 1 cm is desirable for measurements.

Table (3.3): shows sample specifications as requested at the start of this study from the different collections.

Poor coupling between transducers and sample surface resulted in weak wave arrivals that give unreliable results; good coupling can be achieved by using samples with regular surfaces and by adding suitable pressure on the transducers using a pair of C-clamps. Thus, a pair of C-clamps was used to put pressure on the transducers during measurements, as previous literature and experience suggested that applying pressure on the transducers in contact with samples improved the signal amplitude significantly which improved the readings' accuracy (Yomogida and Matsui, 1983). Care should be

taken when dealing with delicate samples, as two of the samples were partially broken due to more-than-suitable pressure applied on the transducers. Samples with existing fractures or cracks were also excluded from the measurement to avoid development of further damage, which also contributed to reducing the number of available samples.

A possible source of contamination, aside from equipment, is the platform used for measurements. Samples leave powder that might mix with other samples, and this was addressed by working on a piece of aluminum foil that was replaced regularly.

3.2.3.2 Elastic Wave Velocity Measurements

Equipment for elastic wave velocity measurements included a manually controlled electric pulse generator/receiver (Olympus Model 5077 PR) with a bandwidth of 35 MHz, a 100-MHz-bandwidth Tektronix Digital Phosphor Oscilloscope (Tektronix Model DPO2014), two pairs of 6-mm-diameter compressional and shear wave ultrasonic contact transducers (Olympus V133 and V156 respectively) and a Mitutoyo digital caliper. A pair of C-clamps was used to put pressure on the ultrasonic transducers to ensure optimum coupling at the transducer-sample contact (Figure 3.5).

The pulse generator/receiver sends a waveform with a predefined frequency of 1.5 MHz; however, using 1 MHz frequency for both P- and S-wave measurements produced better results than the recommended frequency of 1.5 MHz. Despite the details of the amplitude, wavelength, and sampling rate of the waveform not being the main concern of the measurement, resolving S-wave from P-wave arrivals is influenced by identifying the corresponding waveform shape, and picking the correct arrival times on the oscilloscope

61

depends on receiving strong apparent wave amplitudes. Thus, it is important to track the changes in amplitude and use consistent sampling rate and wavelengths.

Once in operation, an electric waveform is sent from the pulse generator and is received simultaneously by the oscilloscope and transmitter-transducer. The oscilloscope is triggered by this pulse to set a zero point for any record of incoming signals while the transducer (transmitter) converts the electric pulse to an ultrasonic (sound) wave that travels through the sample to be received at the opposite side by the receiver-transducer. Once received, the ultrasonic wave is converted back to an electric signal that is recorded by the oscilloscope and displayed on its screen as samples per second. Sound wave travel-time through the meteorite samples is displayed as *Δt* (μsec). This *Δt* value corresponds to the thickness of the meteorite slab *x (mm)*, which is measured using a digital caliper. Given the values of both sample thickness and travel-time, the sound wave velocity (*v*) is given by:

$$v = \frac{x}{\Delta t} \qquad (3.9)$$

Figure (3.5): Shows images of the equipment used throughout the elastic wave velocity measurements: A manually controlled electric pulse generator/receiver (Olympus Model 5077 PR) with a bandwidth of 35 MHz (Upper left), a 100-MHz-bandwidth Tektronix Digital Phosphor Oscilloscope Tektronix Model DPO2014 (Upper right), a sample slab of Lancé (CO-chondrite), two pairs of 6-mm-diameter P- and S- wave ultrasonic contact transducers (Olympus V133 and V156 respectively) and a pair of C-clamps.

Elastic wave velocity was measured at least four times for each sample with the exception of a few fragile samples that showed weak structure. Prior to each measurement session, the inherent time delay between the transducers was measured by clamping both transducers with no samples in between to read the Δt value corresponding to zero-thickness. This delay time, which is approximately 5-7% of the arrival time, was

used as a correction factor for the calculated P- and S-wave velocity values. A standard PVC block of known thickness and travel time was used as a test sample for both P- and S-wave measurement (see Appendix B for details on wave arrival).

Measurement of S-wave travel-times is always complicated by some P- wave arrivals; because some S-waves are converted to P-waves at transducer-sample contact due to the difference in acoustic impedance (any small difference between two media in terms of density and velocity qualifies for an impedance contrast).

$$Z = \rho.v \qquad (3.10)$$

To discriminate S- from P-wave arrivals, the transducers are oriented so that the polarization direction of the waves is in-phase with that of the transducers. This results in achieving robust S-wave arrivals while P-waves remain relatively constant (ideally P-wave propagation direction is parallel to particle vibration direction). Note that the extent of rotating the transducers is arbitrary, because transducers are not ideal mechanical devices, and the samples are not homogenous materials, leading to variation in waves' propagation.

The areas on the samples' surfaces where the transducers have been in contact with the sample are used as positions for the digital caliper edges to measure sample thickness. Thickness values, typically in the range of 1 - 2 cm, are averaged across the sample where the transducers were introduced, and the standard deviation of mean thickness provides an estimate of the standard error in measurements. Thickness variations for each sample are less than 1 mm in perfect slabs, and ~ 1 mm for semi-slabs. Occasionally, the transducers are not aligned perfectly against each other, which

does not have a significant effect on the measured travel time, and taking the mean value of repeated measurements should correct for any variation.

The limitations of this methodology lie in achieving effective coupling at the sample-transducer surface, which was addressed appropriately as discussed previously. However, one other limitation that is common to all such measurements is that those obtained elastic waves velocities are averaged along the waveform travel path, and do not represent specific regions of the samples unless a tomographic elastic wave measurement is applied. The velocities for each sample are averaged for four to five readings from different positions on the sample to represent as much regions on the sample as possible.

3.2.3.3 Bulk Density Measurements

Several approaches were adopted in bulk density measurement of meteorites, and required knowledge of the sample's mass and bulk volume to calculate the density. Mass determination is trivial to accomplish with any well calibrated mass balance. However, bulk volume measurement depends on the geometry of the samples. Volumes of regularly shaped samples are easy to measure from their geometry, but not as convenient for irregular samples as cutting might cause partial sample destruction, alteration at cut surfaces, mass loss, addition of new cracks or fractures during the preparation of the sample, or might not be allowed given the type or size of meteorite. To address this, other approaches were developed to measure irregular samples. One approach determines samples' volume by making clay molds of the samples, which requires packing them into clay and molding the clay into a measurable shape, then removing the mold and repacks it

with some material and measure the volume (Britt and Consolmagno, 2008). However accurate this method, it had the great disadvantage of contaminating meteorites.

The most commonly used method is the Archimedean method as modified by Britt and Consolmagno (1998). Originally, the Archimedean method is based on using water as the fluid, which takes the shape of the irregular sample, but in the case of meteorites it immersing the sample in water or any other liquid might allow the liquid to penetrate the sample and produces a different volume somewhere between the bulk volume and grain volume. To avoid this risk, Consolmagno and Britt (1998) introduced glass beads as possible replacement for water as the fluid medium. These beads follow approximately the shape of the sample and can avoid penetrating fractures and cracks, and are visible enough to detect and remove if they stick to the sample. The Archimedean volume determination is relatively accurate, fast and non-reactant to the sample or introduces any risk of damage; thus, this method provides a reliable effective way to measure a large suit of samples in a timely manner with good results.

The methodology is simple and becomes easier and more rapid and efficient with increasing the number of measurements. It operates as follows:

- First: ensure that the digital mass balance used for measurements is well calibrated. Then, a suitable container, with known volume and mass ($M_{Container}$), is selected (Figure 3.6). It is a good practice to measure the container's mass after a few measurements. Container and beads are placed within a large tray at the start of measurement to avoid unnecessary scatter.

- Second: Beads are then slowly and carefully poured into the container to allow the beads to settle until the container is overflowing, then the sides of the container are

tapped gently while the container is held securely, to encourage proper settling of the beads. Additional beads are then added until the beads are more than the top of the container, and a smooth straight edge is used to scrape the top gently multiple times to ensure a leveled top of the container. Then, the mass of the container filled with beads is measured (M_{Glass}).

- Third: Same container is then emptied and an appropriate sample is placed within the container after placing a thin layer of beads at the bottom of the container. This beads layer should be thick enough to prevent any contact between the sample and the base of the container. Beads are poured around and above the sample, and the container is gently tapped to ensure sample is completely engulfed by the beads. The mass of container filled with beads and sample is then measured (M_{Total}).

Throughout the measurements, the procedure was to do the three steps simultaneously and repeated four or five times so long that the sample did not produce powder. Beads of ~ 1mm diameter were used consistently throughout the study. Although this size is one or two orders of magnitude larger than the conventional sizes used by some other studies (e.g. Kohout et al., 2008; Macke et al., 2010; 2011), the beads are less likely to penetrate pre-existing cracks, and are easier to clean using an ultrasonic cleaner lessening the chances of contaminating the samples. But one disadvantage of working with 1mm beads is that the "wall effect" – produced by the vacancies between the beads and the container walls – is more accentuated between the sample and beads.
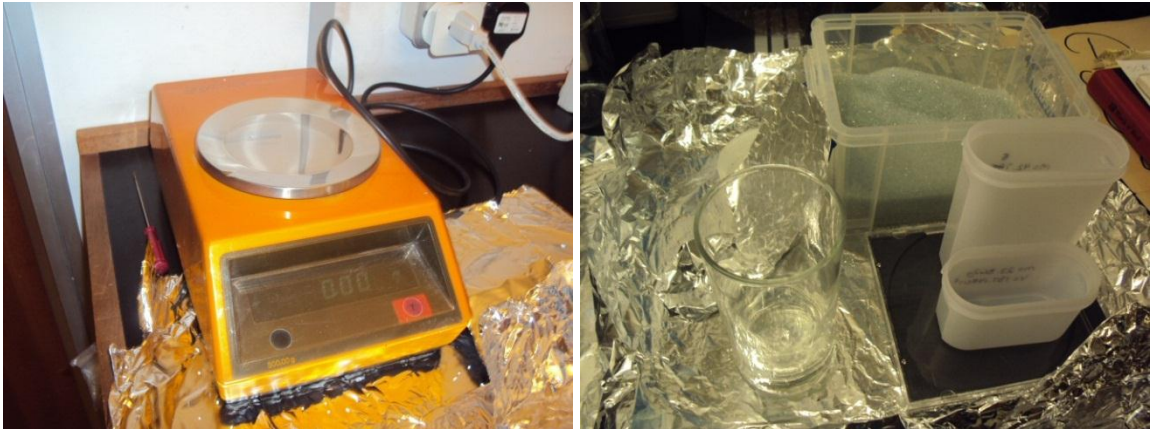
Figure (3.6): shows Images of a digital mass balance that was used at the National History Museum (left), and the glass beads and some of the containers used throughout the study (right).

Plastic containers of different sizes were selected based on the shape and size of the sample to accommodate each sample. Containers slightly larger than sample size were recommended to lessen the uncertainty related to how the beads are settled (Hons, 2004; Macke et al., 2010a). However, containers much larger than the sample are more likely to increase the wall effect (Hons, 2004). On the other hand, containers that are very close in size to the sample's size were found to prevent proper settling of the beads around the sample, which will create voids, and result in overestimating the volume and underestimating the bulk density. Therefore, containers slightly larger than the samples are preferred to ensure proper settling of the beads.

Measurements were conducted in room temperature where a thermostat showed daily variations of 1 ^{0}C on average, although humidity varied from the first meteorite collection, NHM- London, to the collections visited in the US (AMNH and NMNH). The variation of temperature and humidity and its effect on the beads' settlement were studied

in detail by Macke et al. (2010a). They found no correlation between beads' densities and temperature, pressure or humidity for the larger size beads such as those used in this study, which limits the uncertainty in the measurements to the measurement procedures and the wall effect.

The sample volume within the cup accompanied by the glass beads is given by:

$$V_{Sample} = V_{Container} - V_{Beads} \qquad (3.11)$$

If M_{Total} is the mass of the container filled with beads and the sample, then the volume of glass beads will be:

$$V_{Beads} = \frac{M_{Beads}}{\rho_{Beads}} = \frac{M_{Total} - M_{Container} - M_{Sample}}{\rho_{Beads}} \qquad (3.12)$$

Combining both equations, we get:

$$V_{Sample} = V_{Container} - \frac{M_{Total} - M_{Container} - M_{Sample}}{\rho_{Beads}} \qquad (3.13)$$

Where the density of the beads alone within the container is calculated from the second step of the measurement procedure explained previously:

$$\rho_{Beads} = \frac{M_{Beads+Container} - M_{Container}}{V_{Container}} \qquad (3.14)$$

Substituting equation (3.14) into equation (3.13):

$$V_{Sample} = V_{Container} - \frac{M_{Total} - M_{Container} - M_{Sample}}{\frac{M_{Beads+Container} - M_{Container}}{V_{Container}}} \qquad (3.15)$$

This becomes:

$$V_{Sample} = V_{Container} \left[\frac{M_{Beads+Container} + M_{Sample} - M_{Total}}{M_{Beads+Container} - M_{Container}} \right] \quad (3.16)$$

Then to get the bulk density of the sample, the sample volume is substituted into:

$$\rho_{bulk} = \frac{M_S}{V_S} \quad (3.17)$$

3.2.4 Measurement Uncertainty

3.2.4.1 Elastic wave velocity Uncertainty

As a part of a separate study, a sedimentary core was used to test ultrasonic wave propagation through rock samples. Several experiments were conducted, and small amounts of water and liquid gel couplants were applied to the samples' surfaces to investigate how couplants will affect the obtained values. Applying small amounts of water drops or liquid gel yielded sharper wave arrivals, without a substantial change in the measured wave travel time values. However, working with meteorites there is a disadvantage in using couplants, such as water or any other liquid, in the possible penetration of these liquids into the sample might modify porosity and possibly alter some mineral components (Consolmagno and Britt, 1998). Changes in porosity values result in modifying the elastic waves travel times, which will be used to determine the elastic wave velocities. Dealing with meteorites, there is continuously a concern of sample contamination, which justifies why no couplants were applied to samples during elastic wave velocity measurements.

Uncertainty in elastic wave velocity measurements is introduced by the inherent uncertainty in elastic waves travel time instruments (transducers and oscilloscope), and sample's thickness measurements. But the biggest uncertainty is in the first pick of the elastic waves on the oscilloscope display. In this study, uncertainty in compressional and shear wave velocities is estimated as one standard deviation of the mean velocity for each sample (see Appendix B for values).

3.2.4.2 Bulk Density Uncertainty

With the advances in specialized mass measurement tools and their increased accuracy, specifically digital mass balances, the uncertainty associated with bulk density measurements is associated mostly with bulk volume determination. The main assumption when using glass beads as the fluid in this method is that glass beads are equivalent to an incompressible fluid similar to water or any other liquid, which is not true. The random component of the uncertainty involves the consistency in packing the beads within the container around the sample, and keeping the surface of the beads leveled at the top of the container. Macke et al. (2008) conducted several experiments to evaluate the optimum methodology to settle the beads in a consistent manner. They suggested that mechanical shaking while holding the container filled with beads (and sample), resulted in the smallest variation in measurements, and the selection of a suitable container size is critical in obtaining reliable results.

71

The systematic error, associated with 1-mm glass beads, is caused by the wall effect (e.g. Hons, 2004; Jones, 2009; Macke et al., 2011). This effect results from the voids, existing between the beads, the beads and the sample, and the beads and the container "walls", which effectively overestimates the obtained bulk volume of the sample, and underestimates the bulk density. To correct for this effect, minerals with known bulk density are used to calibrate the density obtained via the glass beads method. The difference between the known and measured density values is then plotted against the sample mass (the smaller samples are more affected by the correction). The slope obtained from the plot provides a correction factor for the measured bulk density values (e.g. Jones, 2009; Macke, 2011).

3.3 Results

The current meteorite classification scheme identifies four clans of carbonaceous chondrites; CI clan, CR clan, CM-CO clan, and CV-CK clans, eight groups and five subgroups (Table 3.2). The term "clan", which has been added relatively recently to the classification schema, is used to indicate a higher level of classification than "group" and lesser than "class". Within the clans, members with similar refractory − lithophile element abundances, plot closely on O-isotope mixing line, and share similar petrologic characteristics, are identified as groups (Weisberg et al., 2006).

In this study, aqueous alteration was used as a basis to separate samples into two groups; the hydrated carbonaceous chondrites including those members showing

evidence of aqueous alteration (CM- and CR-chondrites), and non-hydrated include members that do not show clear evidence of aqueous alteration (CO-, CV- and CK-chondrites).

CI-chondrites – the most hydrated carbonaceous chondrites - were excluded from this study, because of their extreme friability; thus, will not be discussed in the following sections. Data acquired throughout the study are summarized in Table (3.4) and Table (3.7). This section will summarize all observations and results for the individual meteorite groups.

3.3.1 Hydrated Carbonaceous Chondrites

Aqueous alteration on small bodies is one of the widespread processes that have affected primitive material in the early solar system; including chondritic materials and inter-planetary dust particles (Brearley, 2006). Since the discovery of clay minerals in the CI-carbonaceous chondrite *Orgueil*, the significance of water in aqueous alteration processes in the solar system processes became of high interest in meteorite studies (e.g. Rivkin, 2006: and references therein). Most carbonaceous chondrite classes have experienced hydration to some extent at some point during their lifetimes; however, only CI-, CM-, and CR-chondrites (to a lesser degree) show any evidence of aqueous alteration. In the context of elastic property analysis, CR-chondrites' mineralogy should disqualify them from being described as hydrated, as the members of this class have very low matrix abundances, weak evidence of phyllosilicates presence and large mm-scale chondrules.

CM – Chondrites

CM- (Mighei-like) chondrites are the most abundant and diverse group amongst carbonaceous chondrites, and are found as individual meteorites as well as clasts within other meteorites, which might be indicative of populous CM-chondrites' parent bodies in the early Solar System (Weisberg et al., 2006). CM-chondrites are generally characterized by relatively visible small chondrules and clastic components (Calcium-Aluminum-rich Inclusions CAIs and Amoeboid Olivine Aggregates AOAs) that have been - partially or completely- replaced by phyllosilicates (McSween, 1979). Their matrices comprise ~ 70% vol of the whole-rock composition, which is second in abundance only to CI-chondrites, and these matrices usually contain small amounts of metal.

The Meteoritical Bulletin (as of July 2012) lists 15 CM-chondrite falls, of which 11 are included in this study. The five falls that were not found are: Erakot, Haripura, Maribo, and Sayama. Erakot and Haripura are both Indian falls, and most of their masses are curated by the Geological Survey of India (Grady, 2000), and Sayama is held at a private collection in Tokyo (Meteoritical Bulletin, accessed June 2012).

The bulk density was measured for 14 samples of 11 CM-falls; yielding an average bulk density of 2.20 ± 0.05 gm/cc per meteorite, and 2.22 ± 0.06 gm/cc per sample, with a minimum of 1.96 gm/cc (Nogoya) and a maximum of 2.55 gm/cc (Banten). It is noteworthy to mention that Nogoya (USNM 6490) was a remarkable sample in terms of appearance; as it displayed brecciation on the centimeter scale, which might have contributed to its very low bulk density.

74

Sample	Type	Petr. Type	Shock	Fall time	CRE age	ρ (gm/cc)	Vp (m/sec)	Vs (m/sec)	Vp/Vs
Banten	CM	2	***	1933	***	2.55	2784	1781	1.56
Bells	CM	2	1	1961	0.37	2.28	2500	1625	1.54
Boriskino	CM	2	***	1930	0.72	2.41	2943	1632	1.80
C. Bokkeveld	CM	2	1	1838	0.56	2.23	3461	2235	1.55
Crescent	CM	2	1	1936	***	2.02	1854	1293	1.43
Mighei	CM	2	1	1889	3.49	1.96	1542	979	1.57
Murchison	CM	2	2	1969	1.32	2.21	2379	1564	1.52
Murray	CM	2	1	1969	4.69	2.18	2483	1362	1.82
Nawapali	CM	2	***	1890	0.71	2.17	2331	1588	1.47
Nogoya	CM	2	1	1879	0.19	2.07	2347	1418	1.66
Pollen	CM	2	1	1942	1.71	2.27	1844	1225	1.50
Santa Cruz	CM	2	1	1939	6.78	2.06	1549	956	1.62
Renazzo	CR	2	2	1824	5.10	3.10	3472	2183	1.59
Al Rais	CR	2	1	1957	11.80	2.32	2067	1319	1.57

Table (3.4): Data of the hydrated carbonaceous Chondrites obtained from this study (CM- and CR-chondrites). CRE = Cosmic ray exposure, ρ Bulk density, Vp P-wave velocity, Vs S-wave velocity, and Vp/Vs is the Vp/Vs ratio.

Compressional wave (P-wave) velocity values for CM-chondrites coincide with sedimentary rocks, shale and unconsolidated sedimentary rocks. The mean P-wave value for CM-chondrites is 2335± 165 m/sec ranging between 1542 m/sec (Mighei) and 3461 m/sec (Cold Bokkeveld). Shear wave (S-wave) velocity ranged between 957 m/sec (Mighei) and 2236 m/sec (Cold Bokkeveld) with a mean value of 1472± 102 m/sec.

In terrestrial geology, V_P/V_S is usually used to indicate the extent of damage in the regions underneath craters. Damaged regions underneath craters were observed to correspond to dramatically high V_P/V_S (> 2), which corresponds to reduction in S-wave velocities in the region. CM-chondrites exhibited a range in V_P/V_S between 1.4 (Crescent) and 1.8 (Boriskino) with a mean V_P/V_S of 1.6 ± 0.03. Table (3.5) summarizes the V_P/V_S for all the carbonaceous chondrite groups. Whereas the variation in the V_P/V_S amongst members within the same group is more pronounced (see Appendix 1 for detailed values), the V_P/V_S remain constant amongst the different groups with the exception of CM-chondrites. CM-chondrites exhibit the highest mean values of Vp/Vs, which might indicate more damage experienced by members within this group as compared to other groups. The elastic moduli show a range of values that are significantly lower than terrestrial material, and slightly lower than ordinary chondrites (Table 3.6).

Group	Vp	Vs	Vp/Vs
CM	2323	1450	1.61
CR	2910	1837	1.59
CO	2585	1655	1.57
CV	3242	2093	1.54
CK	1700	1125	1.50
CBa	2730	1758	1.55

Table (3.5): Mean values of P-wave and S-wave velocities and Vp/Vs for all carbonaceous chondrite groups as obtained from this study.

Sample	Type	Fall time	P (gm/cc)	μ (GPa)	K (GPa)	λ (GPa)	ν	E (GPa)
Banten	CM	1933	2.55	8.09	8.98	3.59	0.15	18.66
Bells	CM	1961	2.28	6.03	6.22	2.20	0.13	13.68
Boriskino	CM	1930	2.41	6.41	12.30	8.03	0.28	16.39
Cold Bokkeveld	CM	1838	2.23	11.15	11.86	4.43	0.14	25.48
Crescent	CM	1936	2.02	3.38	2.43	0.18	0.03	6.93
Mighei	CM	1889	1.96	1.88	2.15	0.90	0.16	4.37
Murchison	CM	1969	2.21	5.40	5.30	1.70	0.12	12.09
Murray	CM	1969	2.18	4.06	8.06	5.35	0.28	10.42
Nawapali	CM	1890	2.17	5.49	4.50	0.84	0.07	11.71
Nogoya	CM	1879	2.07	4.17	5.87	3.09	0.21	10.11
Pollen	CM	1942	2.27	3.41	3.17	0.89	0.10	7.52
Santa Cruz	CM	1939	2.06	1.88	2.43	1.17	0.19	4.49
Renazzo	CR	1824	3.10	14.77	17.67	7.82	0.17	34.64
Al Rais	CR	1957	2.32	4.04	4.53	1.84	0.16	9.34

Table (3.6): Data of the hydrated carbonaceous Chondrites obtained from this study (CM- and CR-chondrites), the elastic moduli Shear modulus μ, Bulk Modulus k, Lamé parameter λ, Poisson' ratio ν, and Young' modulus E.

CR – Chondrites

CR- (Renazzo-like) chondrites are described as breccias containing large millimeter-size chondrules, low abundance in CAIs and AOAs, and some matrix-like material that is commonly known as dark inclusions (Weisberg et al., 2006). They have the lowest metal content as compared to other classes in the CR-clan with the chondrules containing most of the metal, and are moderately hydrated with all of them classified as petrologic type 2.

Only three falls have been recorded to date: Al Rais, Kaidun and Renazzo. Despite the fact that CR-chondrites are depleted in volatiles, they are still considered to be very primitive based on their refractory lithophile abundances that are similar to the solar photosphere (Weisberg et al., 2006). Al Rais and Renazzo, which are included in this study, show more evidence of aqueous alteration than the average CR-chondrites resembling CM-chondrites in this respect.

The bulk density of CR-chondrites overlaps with that of the non-hydrated carbonaceous chondrites (Table 3.4 and Table 3.7), with CR-chondrites' mean density of 2.7 ± 0.4 gm/cc (ranges between 2.3 gm/cc and 3.09 gm/cc). P-wave velocities for CR-chondrites range between 2067 m/sec and 3472 m/sec with an average of 2770 ± 360 m/sec. S-wave velocities similarly range between 1319 m/sec and 2183 m/sec and has a mean value of 1751 ± 245 m/sec. Similarly to the CM-chondrites, CR-chondrites' V_P/V_S ratio ranges from 1.4 to 1.8 with a mean value of 1.6.

3.3.2 Non-hydrated Carbonaceous Chondrites

Similarly to the hydrated carbonaceous chondrites, non-hydrated carbonaceous chondrites CO-, CV- and CK-chondrites, show some evidence of aqueous alteration, but not as much as that exhibited by the hydrated chondrites (Brearley, 2006). Most of the non-hydrated carbonaceous chondrites resemble – to a certain degree – the ordinary chondrite in terms of physical properties and appearance. Non-hydrated carbonaceous chondrites range between petrologic types 3 and types 6, but the observed falls' ranges are only found between types 3 to 4. Matrix abundances of non-hydrated carbonaceous chondrites are much lower than hydrated, ranging between 30 – 50% (Weisberg et al., 2006).

CO – Chondrites

CO- (Ornans-like) chondrites are characterized by relatively small chondrules (~ 0.15 mm) and high matrix abundance. They are known to be the least aqueously altered and the least thermally metamorphosed group among the carbonaceous chondrites (Brearley et al., 2006; Huss et al., 2006). They range between petrologic type 3.0 – 3.7 (Weisberg et al., 2006), with secondary minerals completely absent in the pristine type 3.0 gradually appearing with increasing the petrologic type. Despite the differences in their petrology and mineralogy, CM- and CO-chondrites are linked together as one clan (CM-CO clan) based on the similarity in their refractory-lithophile-element abundances, their high-temperature minerals have similar O-isotopic compositions, similar chondrule sizes, and anhydrous minerals composition (Weisberg et al., 2006).

Amongst the samples measured, CO-chondrites were the most abundant samples throughout the study, 14 samples of the 6 CO-chondrite falls were included (Table 3.7). Multiple samples were measured for each meteorite except for Warrenton (CO 3.7). CO-chondrites show a range of bulk density that falls in the middle between the hydrated and non-hydrated carbonaceous chondrites with an average bulk density of 2.8 ± 0.1gm/cc (ranging between a minimum of 2.4 gm/cc and a maximum of 3.4 gm/cc). The variation in bulk density between multiple samples of the same meteorite ranges from 1% - 57% of the variation in density between the CO-chondrite meteorites. Kainsaz showed the largest variation in bulk density amongst its three measured samples compared to the total variation amongst CO-chondrites as a group.

CO-chondrites show a lower elastic wave velocity than CR-chondrites with a mean P-wave velocity of 2400 m/sec (± 9%) (ranging between 1747 m/sec and 3088 m/sec) and mean S-wave velocity of 1526 m/sec (± 10%) (ranging between 1050 m/sec and 1982 m/sec). This could be explained by enhanced elastic wave propagation through the abundant metal-rich chondrules in CR-chondrites, as opposed to the less dense phyllosilicates-rich matrix that is characteristic of CM-chondrites while CO-chondrites have small non-metal-rich chondrules that will not have much influence on the elastic wave travel time or the elastic properties obtained (Table 3.8).

Sample	Type	Petr. Type	Shock	Fall time	CRE age	ρ (gm/cc)	Vp (m/sec)	Vs (m/sec)	Vp/Vs
Kainsaz	CO	3.2	1	1937	20.80	2.96	2958	1982	1.49
Felix	CO	3.3	3	1900	51.40	2.86	2009	1306	1.54
Ornans	CO	3.4	1	1868	19.80	2.40	2073	1372	1.51
Lancé	CO	3.5	1	1872	5.00	3.36	3088	1965	1.57
Moss	CO	3.6	***	2006	13.90	2.54	2529	1481	1.71
Warrenton	CO	3.7	1	1877	30.60	2.55	1747	1051	1.66
Allende	CV	3	1	1969	5.20	2.84	2394	1572	1.52
Bali	CV	3	3	1907	28.10	***	4203	2569	1.64
Grosnaja	CV	3	3	1861	1.70	2.90	3778	2518	1.50
Kaba	CV	3	1	1857	11.80	2.75	2440	1665	1.47
Mokoia	CV	3	1	1908	9.70	2.68	1016	665	1.53
Vigarano	CV	3	2	1910	5.60	3.20	4141	2618	1.58
Karoonda	CK	4	1	1930	40.20	2.65	1161	817	1.42
Ningqiang	CK	3	1	1983	39.70	3.26	1971	1280	1.54

Table (3.7): Data of the non-hydrated carbonaceous Chondrites obtained from this study (CM- and CR-chondrites). CRE = Cosmic ray exposure, ρ Bulk density, Vp P-wave velocity, Vs S-wave velocity, and Vp/Vs is the Vp/Vs ratio.

CV – Chondrites

CV-chondrites (Vigarano-like), unlike the typical non-hydrated groups, have a high abundance of matrix, CAIs, AOAs and large chondrules (about 1mm) with all members classified as petrologic type 3. Based on their modal metal/magnetite ratios and

Ni-content of metal and sulphides, CV-chondrites are classified into two subgroups: oxidized (CV_{ox}) and reduced (CV_{red}). Weisberg et al. (1997) subdivided CV_{ox} into the Allende-like (CV_{oxA}) and Bali-like (CV_{oxB}). Despite all CV-chondrite falls being classified as petrologic type 3, CV_{oxB} chondrites contain abundant phyllosilicates and may be classified as type 2 (Weisberg et al. 2006; and references therein). CV_{oxA} are more altered than CV_{oxB}, but their content of phyllosilicates is low in comparison; whereas CV_{red} has experienced alteration to a lesser degree and most members of this subgroup lack phyllosilicates. These observations might indicate that the CV subgroups represent different lithological varieties of their parent body that experienced complex multistage alteration (Weisberg et al., 2006).

In this study, 10 samples of five CV-chondrite samples were available for study; however, bulk density was measured for eight samples. Bulk density ranged between 2.68 gm/cc and 3.7 gm/cc with an average value of 2.96 gm/cc. The elastic wave velocity range is larger for CV-chondrites between 1016 m/sec up to 4202 m/sec with a mean value of 1995 m/sec for P-wave velocity, while the mean S-wave velocity is 1935 m/sec ranging between 665 m/sec and 2618 m/sec. CV-chondrites as a group overlaps with ordinary chondrites in bulk density and elastic wave velocity and derived elastic moduli (Table 3.8).

CK – Chondrites

CK-chondrites (Karoonda-like) are the only group amongst carbonaceous chondrites that shows the whole range of thermal metamorphism, from petrologic type 3 to 6. Among CK-chondrites, those with petrologic type < 4 show similar chemical,

mineralogical and petrological properties to CV-chondrites, which supported a close clan relationship between CV-CK chondrites (Weisberg et al., 2006). They also are analogous to ordinary chondrites in a number of metamorphic effects; homogeneity in olivine and plagioclase sizes increase as the petrologic type increases, but the most distinctive parameter in CK-chondrites is the mean grain size of interchondrule material coarsening significantly as the petrologic type increases.

Sample	Type	Fall time	ρ (gm/cc)	μ (GPa)	K (GPa)	λ (GPa)	ν	E (GPa)
Kainsaz	CO	1937	2.96	11.64	10.40	2.64	0.09	25.43
Felix	CO	1900	2.86	4.88	5.04	1.79	0.13	11.07
Ornans	CO	1868	2.40	4.52	4.30	1.29	0.11	10.05
Lancé	CO	1872	3.36	12.97	14.74	6.09	0.16	30.09
Moss	CO	2006	2.54	5.57	8.82	5.10	0.24	13.80
Warrenton	CO	1877	2.55	2.81	4.03	2.16	0.22	6.85
Allende	CV	1969	2.84	7.03	6.93	2.24	0.12	15.75
Bali	CV	1907	***	***	***	***	0.20	***
Grosnaja	CV	1861	2.90	18.41	16.89	4.61	0.10	40.51
Kaba	CV	1857	2.75	7.61	6.21	1.13	0.06	16.21
Mokoia	CV	1908	2.68	1.19	1.18	0.39	0.12	2.67
Vigarano	CV	1910	3.20	21.96	25.64	11.00	0.17	51.24
Karoonda	CK	1930	2.65	1.77	1.21	0.03	0.01	3.58
Ningqiang	CK	1983	3.26	5.35	5.55	1.98	0.14	12.14

Table (3.8): Data of the non-hydrated carbonaceous Chondrites obtained from this study (CM- and CR-chondrites), the elastic moduli Shear modulus μ, Bulk Modulus k, Lamé parameter λ, Poisson' ratio v, and Young' modulus E.

According to the Meteoritical Bulletin Database (2012), Ningqiang is classified as an ungrouped carbonaceous chondrites; however, we have treated Ningqiang as a CK-chondrite as mentioned in the Catalog of Meteorites (NHM 5th Edition).

Two samples: Karoonda and Ningqiang were available for measurements. Bulk density averages 2.96 gm/cc with a minimum of 2.65 gm/cc and maximum of 3.26 gm/cc with variability in bulk density is ~10% of the mean value. This is supported by the elastic wave velocity values; mean P-wave velocity of 1700 m/sec ranging from 1161 m/sec to 2006 m/sec (with variability of 15% of the mean), and mean S-wave velocity of 1126 m/sec with a minimum of 817 m/sec and maximum of 1377 m/sec.

3.4 Discussion

3.4.1 Comparison to Previous work

To date, this work presents the first systematic survey of the elastic wave properties of carbonaceous chondrites, as only a handful of measurements existed before on carbonaceous chondrites elastic properties (Jones, 2009; Hons, 2004). A number of studies have reported detailed bulk density data of different meteorite classes and carbonaceous chondrites samples (Macke, 2010; Consolmagno and Britt 2003), and conducting comparisons with these literature values provide some measure of data quality control. As well, comparison of the different values obtained during the different stages of measurement ensured that extreme deviations were investigated on site and helped eliminate instrumentation problems.

The current work reports the bulk density values of some common samples with Macke (2010) and comparisons show an overall consistency between the two data sets (Figure 3.7 a). Consolmagno and Britt (2002) reported a few common bulk densities for similar meteorites, which provided another dataset for comparison with the current work (Figure 3.7 b). However, Macke (2004) had more data points for comparison than Consolmagno and Britt (2002), which makes the comparison more meaningful.

Hons (2004) and Jones (2009) provided elastic wave velocity values for five carbonaceous chondrites that were measured in this study; however, Hons (2004) reported a suspiciously high value of P-wave velocities for Vigarano (6598 m/sec), which exceeded not only the velocity range of the three Vigarano samples in this study, but the whole velocity range of carbonaceous chondrites and ordinary chondrites. Therefore, the author excluded it from the comparisons as it is represents an outlier, and used the remaining four data points (Figure 3.7 c).

Trend lines were used throughout the study to quantify the agreement between different physical quantities. For comparison between the current work and previous literature values, we assumed an ideal scenario of a y-intercept is equal to zero. However, this assumption is not the case in reality, and there are slight variations introduced by many factors governing the measurements. These factors are caused by using different samples of the same meteorite, and meteorites are not homogenous materials. Even for measurements that use the same meteorite sample, these variations can be introduced by the methodology, measurement techniques, operation of equipment and the human factor (experience and accuracy). One major factor is the different size of glass beads used in this study, as the glass beads used in this study were approximately three factors larger

than the ones used in all their surveys (e.g. Consolmagno and Britt, 2002; 2003; Macke et al., 2009; 2011). Overall, these comparisons show that data from the current study are consistent with previous literature data (Figure 3.7); and the observed scatter in the data points is not systematic, as some of the current work values are higher and some are lower than those obtained from literature.

One of the objectives of this study was to observe the trends among physical properties that were documented by Hons (2004) and Jones (2009) for ordinary chondrites, and to confirm or reject existing trends and discover new trends. Those trends included: (1) velocity increase with terrestrial residence time, (2) velocity increase with bulk density, (3) velocity increase with darkness, (4) velocity decrease with petrologic type (Hons, 2004), (5) bulk density decrease with increasing terrestrial residence time, (6) bulk density increase with petrologic type, and (7) Poisson's ratio and Vp/Vs decrease with petrologic type (Jones, 2009). The following sections will discuss observed trends form this study and their implications on the parent bodies of carbonaceous chondrites.
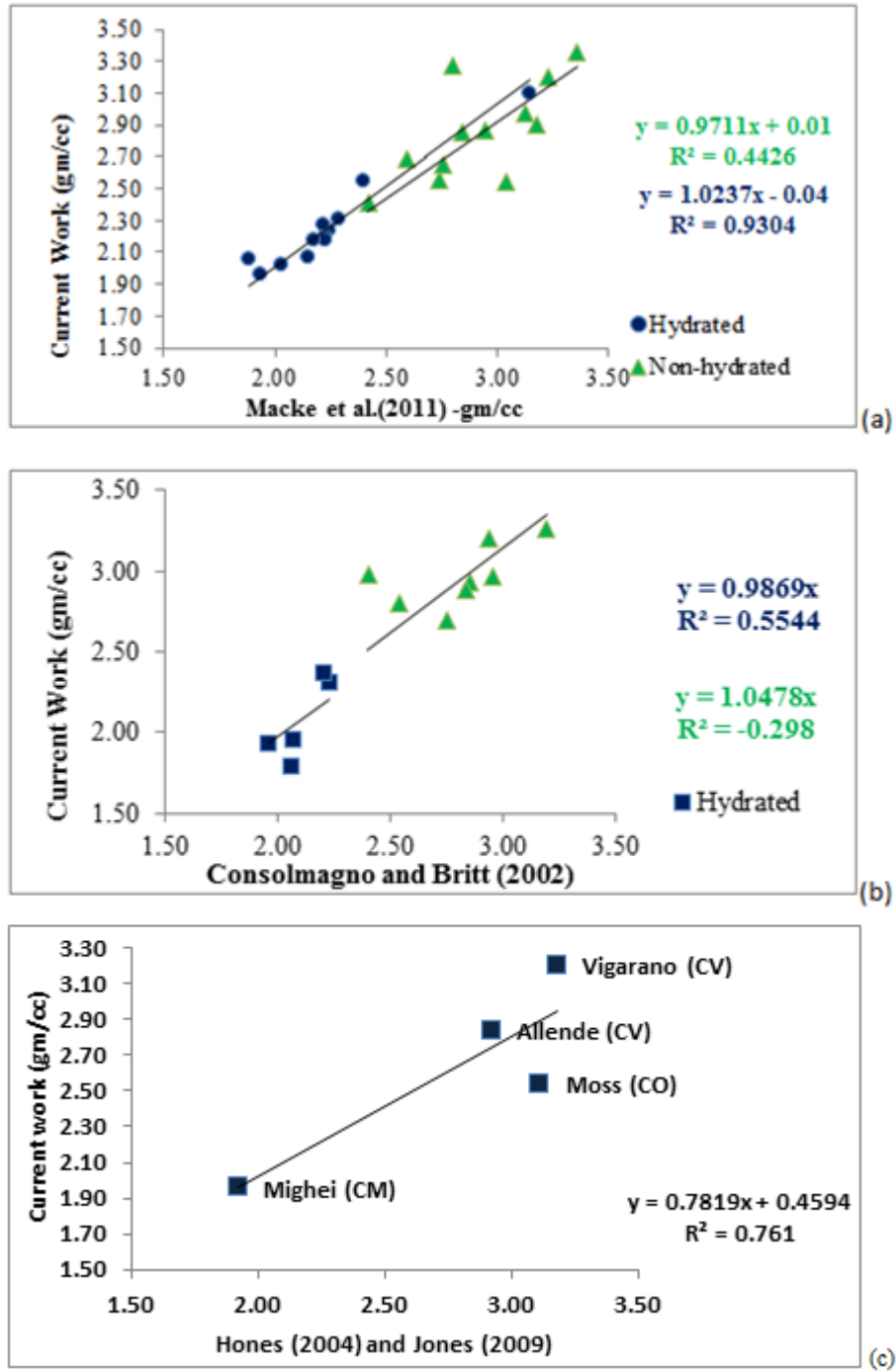
Figure (3.7): A comparison of the bulk density obtained in this study with values from the literature; (a) with Macke et al. (2011), (b) with Consolmagno and Britt (2002), and (c) *Jones (2009) and Hons (2004).*

3.4.2 Elastic Properties variation with physical properties

Bulk Density

The elastic wave velocities and the derived elastic moduli were found to increase with increasing the bulk density (Figure 3.9), which is consistent with observations of terrestrial rocks (Knopoff, 1967; and references therein) and ordinary chondrites (Yomogida and Matsui, 1983; Hons, 2004; Jones, 2009). This was observed for groups with sufficient samples (CM-, CO-, and CV-chondrites). Since higher bulk densities coincide with lower porosity, and materials with more packing are able to propagate waves at higher speeds than loosely packed material, it is expected to observe faster propagation of elastic waves with increasing the bulk density. S-wave velocities mirror the P-wave velocity − bulk density trend (Figures 3.9 and 3.10). This trend is the most statistically significant trend throughout the study; CM-chondrites have 12 samples, which allows for a meaningful correlation and the statistical significance was obtained using a Pearson Correlation Coefficient Test (PCC-Test) and found to be 97.84% for the Vp versus ρ and 96.31% for the Vs versus ρ, based on the number of data points and R value. The hydrated carbonaceous chondrites population (CM + CR) show a statistically significant increase of P- and S-wave velocities with bulk density (99.5% for Vp versus ρ and 99.39% for Vs versus ρ). Similar to CR-chondrites, more data points are also required to confirm this trend for both CK-chondrites. However, the statistical significance for CO-chondrites using the same correlation coefficient test was found to be 90.41% for the Vp versus ρ and 91.45% for the Vs versus ρ. The non-hydrated carbonaceous chondrites population shows a statistically significant increase of P- and S-

wave velocities with bulk density (93.57% for Vp versus ρ and 93.96% for Vs versus ρ). The low R^2 values are due to the large amount of scatter in the data. Subsequent investigation for two data points in the non-hydrated group to check for any problematic behavior, and found no reason to exclude them.

Petrologic Type

In terrestrial rocks, increasing the degree of metamorphism increases the elastic wave velocity. In meteorites, the extent of thermal metamorphism is quantified by a number ranging between 1 and 6 and referred to as the petrologic type. This number increases from 3 to 6 reflecting an increase in thermal metamorphism, and moving from 3 to 1 indicating an increase in aqueous alteration. In meteorites, P-wave and S-wave velocities decrease with increasing the petrologic type (Hons, 2004; Jones, 2009), and the non-hydrated carbonaceous chondrites showed this trend between petrologic type 3 and 4. This is somewhat puzzling since observations on metamorphosed terrestrial rocks are the opposite. Speculated causes include an increase in porosity by cracking or fracturing, changes in mineral phases related to increasing metamorphic grade, and/or recrystallization of matrix texture related to increasing metamorphic grade (Bland, 2006; Jones, 2009). Another possibility that Hons (2004) is that impact-induced shock might have influenced the elastic wave velocity positively because of impact melting, but as a result of this shock new fractures were introduced on the micro and macro scales leading to an overall decrease in elastic wave velocities.

Since all hydrated chondrites are all found as type 2, all CV-chondrites are found as type 3, and not enough data were available for CR- and CK-chondrites, the elastic

wave velocities variations with petrologic types were investigated for CO-chondrites from types from 3 to 4. CO-chondrites showed a reduction of P- and S-wave velocities with petrologic types with low statistical significances of 49% for Vp and 69% for Vs versus petrologic type (Figures 3.12 and 3.13). However, the total non-hydrated carbonaceous chondrites population shows a statistically significant decrease of both P- and S-wave velocities with petrologic type (89% for Vp and 91% for Vs versus petrologic type).

Terrestrial Residence

Previous work showed that weathering has a significant effect on bulk and grain densities and elastic wave velocities (e.g. Hons, 2004; Jones, 2009). Ordinary chondrites showed (1) fresh meteorite falls have a narrow range of elastic wave velocities relative to older falls, and similarly falls show less variation compared to meteorite finds, and (2) an increase in elastic wave velocity with terrestrial residence corresponding to an increase of bulk density (Hons, 2004; Jones, 2009).

Carbonaceous chondrites show a similar trend in that falls that occurred less than 60 years ago show some clustering at lower velocity values relative to older falls which show higher elastic wave velocities and more variation in their values. CM- chondrites exhibited an increase in Vp and Vs with increasing terrestrial residence with relatively low statistical significance of 64% for Vp and 74% for Vs versus fall date (Figure 3.13). More data points are required to confirm this trend for CR-chondrites. However, the hydrated carbonaceous chondrites as a population show a statistically significant increase

90

of P- and S-wave velocities with fall date (94% for Vp and 96% for Vs), which contrasts the low significance exhibited by CM-chondrites alone. The addition the two CR-chondrites seem to have changed the trend line substantially. It might be possible that the hydrated CM-chondrites are less susceptible to terrestrial weathering because of their low metal content, thus oxidation products have less effect on porosity; whereas, CR-chondrites are rich in their large iron-rich chondrules that are more susceptible to weathering and oxidation. This might explain why the trend was strengthened by the addition of the two CR-chondrites to the population.

In contrast to the hydrated carbonaceous chondrites and CV-chondrites, CO-chondrites show a decrease in their elastic velocities with increasing terrestrial residence time (Figure 3.14). The statistical significance of this trend was not strong enough to render this trend as a valid one (41% for the Vp and 23% for the Vs versus fall date), but it is still unexpected to be observed only on CO-chondrites even when Moss (fall of 2006) is removed from the data set. Similarly, CV-chondrites show an increase of velocities with low statistical significance (25% for Vp and 33% for Vs). More data points are required to confirm this trend for CK-chondrites. The total non-hydrated population shows a statistically non-significant increase of P- and S-wave velocities with fall date (39% for Vp and 74% for Vs), which contrasts the low significance exhibited by CM-chondrites alone.

In ordinary chondrites, this increase in velocity is attributed to reduction of porosity as new mineral phases are introduced and old phases are altered to gain stability in Earth conditions. These changes include oxidation of Fe-bearing minerals resulting in

91

the formation of less dense minerals that fill pore spaces, which lower the porosity. For carbonaceous chondrites, these changes might include addition of hygroscopic water, formation of sulphates and carbonate veins, mobilization of aqueous trace elements and possible reordering of phyllosilicates (Bland et al., 2006).

Cosmic Ray Exposure Age

Unless shielded, all objects in space have experienced at least one period of exposure to cosmic rays (Eugster, 2002). A variety of cosmogenic stable and radioactive nuclides are produced by this exposure to cosmic rays prior to the arrival to Earth. Provided with a production rate of these nuclides and their concentration, the duration of exposure to cosmic rays can be calculated to give an approximate cosmic-ray exposure (CRE) age. This age is assumed to be the duration of time since a meteorite was excavated from its parent body and got exposed to cosmic rays, up to the moment it entered the atmosphere and got shielded again. This concept; however, is based on two assumptions; (1) prior to departure from the parent body as a result of collision, the object (meteorite) was buried and well-shielded from cosmic-ray particles and (2) the meteorite has not experienced any break-up events during its travel-time to Earth. CRE ages are of significant value in studying impact histories of asteroids; for example, different meteorite classes showing identical CRE age distributions might suggest an origin from the same impact event (Eugster, 2002).

Carbonaceous chondrites have relatively short CRE ages ranging between ~ 0.05 – 7 Ma Most CI- and CM-chondrites have remarkably short ages (~ 0.05 – 2 M.Y.),

which are very low compared to other meteorites, except for the Lunar meteorites (Eugster et al., 2006). Possible reasons for such short ages include the proximity of the parent body to an orbital resonance, or in an Earth crossing orbit that allowed ejecta to land on Earth, or due to their weak structure that limits their survivability (Eugster et al., 2006). CRE ages of CR- and CB-chondrites are not very common, calculated ages for CR-chondrites range between 1 – 25 M.Y., while those of CB-chondrites range was about 30 M.Y., which is expected since they have strong structure supported by the metal component in their composition. The relatively short exposure time of the carbonaceous chondrites as a group was attributed to their weak structure compared to other meteorite types (Eugster, 2002 and references therein). However, weak meteorite breccia with different ranges of CRE ages were observed in most stony chondrites, which suggests that physical strength alone might not be responsible for the length of residence in space.

Throughout this study, elastic wave velocities have been found to decrease in inverse proportion to CRE ages for all groups with sufficient members (CM-, CO- and CV-chondrites). An unanticipated result; as ordinary chondrite clans do not unambiguously show this effect. Note that this correlation holds even for the CM-clan with a maximum CRE age of only ~2 M.Y., and that the correlation equals approximately two thirds of the velocity variation found amongst the CC's. CM-chondrites have 10 meteorites with recognized CRE ages, which allows for a meaningful correlation. The statistical significance was found to be 93% for the Vp versus CRE ages and 97% for the Vs versus CRE ages. The total hydrated carbonaceous chondrites show a lesser statistically significant decrease of P- and S-wave velocities with CRE ages (65% for Vp

and 68% for Vs versus CRE ages). The addition of the CR-chondrites with the significantly longer CRE ages modified the trend significantly, which is expected since the hydrated CM-chondrites have remarkably low CRE ages that coincide with their low strength. The elastic wave velocities decrease with cosmic ray exposure ages for CO-, CV-, and CK-chondrites. CO-chondrites had a statistical significance of 86% for Vp and 78% for Vs versus CRE ages, while CV-chondrites yielded 84% for Vp and 84% for Vs versus CRE ages. The non-hydrated carbonaceous chondrites show a high statistically significant decrease of P- and S-wave velocities with CRE ages (96% for Vp and 96% for Vs versus CRE ages). The implications for this trend are discussed in the next chapter.

Other Physical Properties:

Darkness of samples (how dark in appearance) was found to have a correlation with elastic wave velocity in ordinary chondrites (Hons, 2004; Jones, 2009). This darkness can be due to shock alteration or because of the composition of the meteorite, and was found to be independent of the bulk density variations. However, carbonaceous chondrites are characterized by dark matrices due to their mineralogical composition, which suggests that darkness might be an inherent property of the meteorite samples. Therefore, it would be meaningless to suggest that the presence or absence of any trend between darkness and elastic properties indicates any real relationship.

Shock stage data for the few number of carbonaceous chondrite falls are scarce, which makes deriving any trend with other properties a difficult task. Most carbonaceous chondrites have low shock stages, which might be due to their weak structure and

consequently undergoing higher shocks would lead to their destruction. In our data, carbonaceous chondrites as separate classes do not show variation in shock stages with almost all members in each class are of shock stage 1. Elastic wave velocities and bulk density increase with shock stage for carbonaceous chondrites as one group, which is consistent with the notion that non-destructive impacts will remove more porosity and add more compaction; thus, increasing the bulk density and consequently the elastic wave velocity.
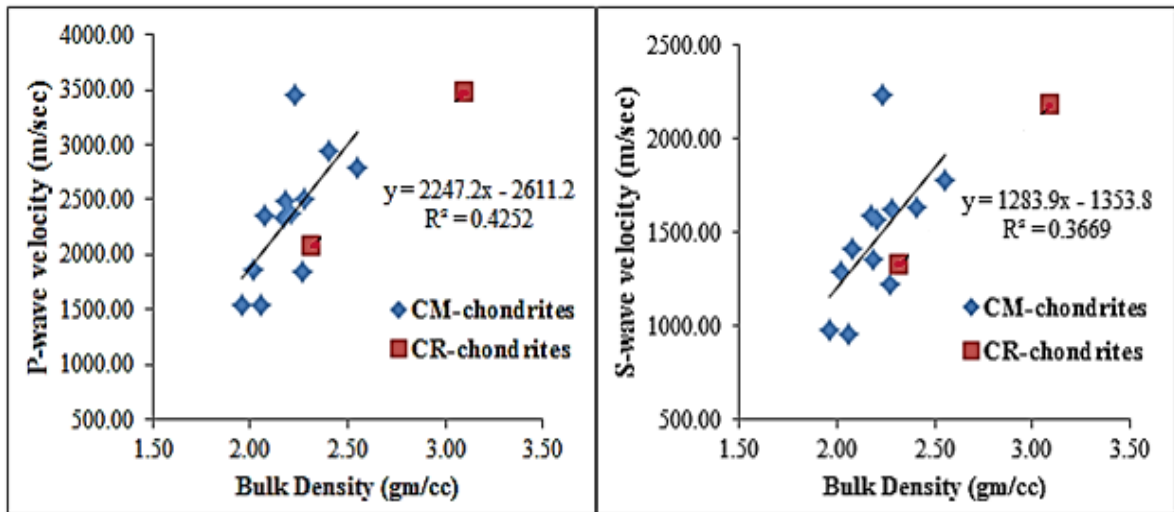
Figure (3.8): *Top:* P- and S- velocities increase with the bulk densities for CM-chondrites. CM-chondrites have 12 samples, which allows for a meaningful correlation; whereas, more data points are required to confirm this trend for CR-chondrites. The statistical significance was obtained using a Pearson Correlation Coefficient Test (PCC-Test) and was found to be 97.84% for the Vp versus ρ and 96.31% for the Vs versus ρ, based on the number of data points and R value. *Bottom:* the hydrated carbonaceous chondrites population shows a statistically significant increase of P- and S-wave velocities with bulk density (99.5% for Vp versus ρ and 99.39% for Vs versus ρ). The removal of the highest density value (Renazzo) did not change the trend line substantially, which might indicate that it is not an outlier. The low R^2 values are due to the large amount of scatter in the data.
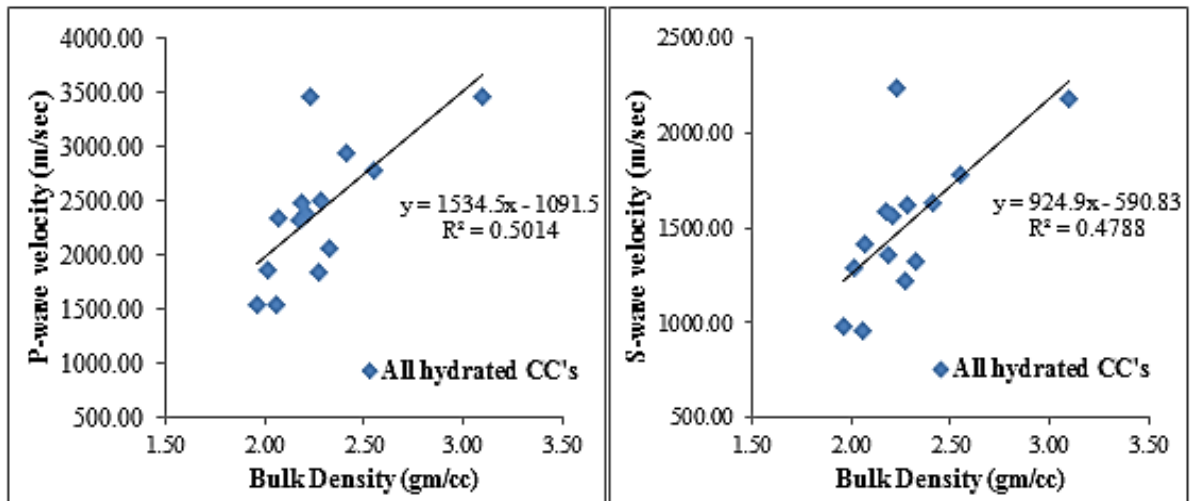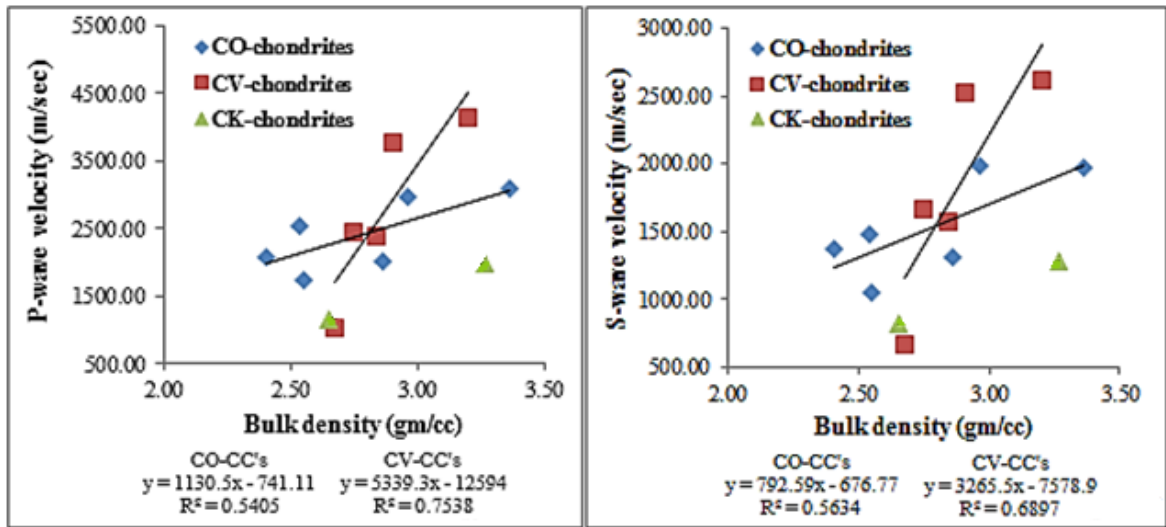
Figure (3.9): *Top:* P- and S- velocities increase with the bulk densities for non-hydrated CO- and CV-chondrites. Similar to CR-chondrites, more data points are required to confirm this trend for both CK-chondrites. The statistical significance for CO-chondrites was obtained using a Pearson Correlation Coefficient Test (requires at least six data points) and was found to be 90.41% for the Vp versus ρ and 91.45% for the Vs versus ρ. *Bottom:* the non-hydrated carbonaceous chondrites population show a statistically significant increase of P- and S-wave velocities with bulk density (93.57% for Vp versus ρ and 93.96% for Vs versus ρ). The low R^2 values are due to the large amount of scatter in the data.
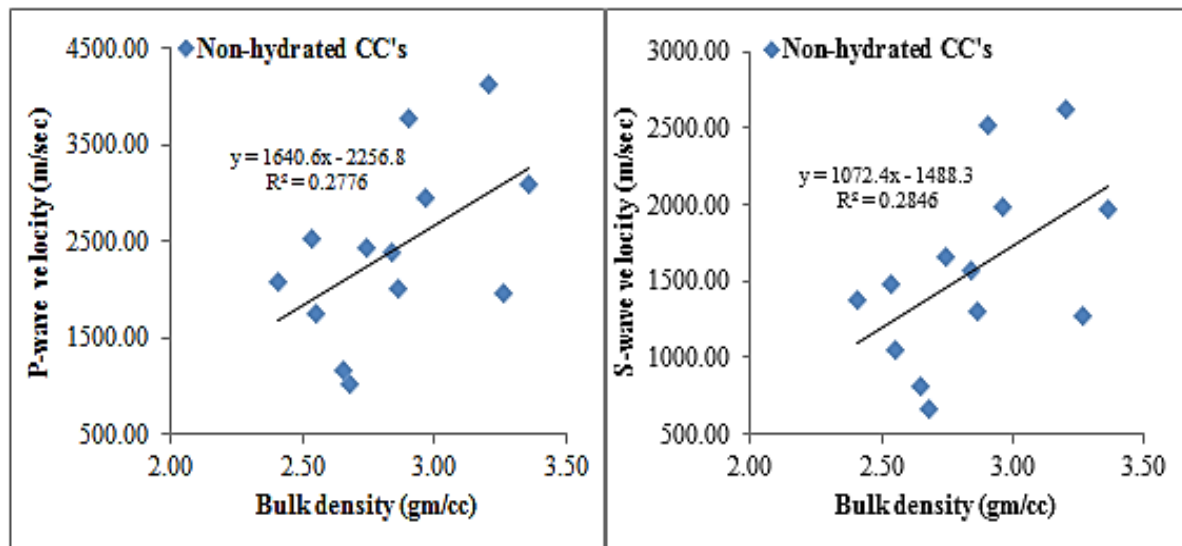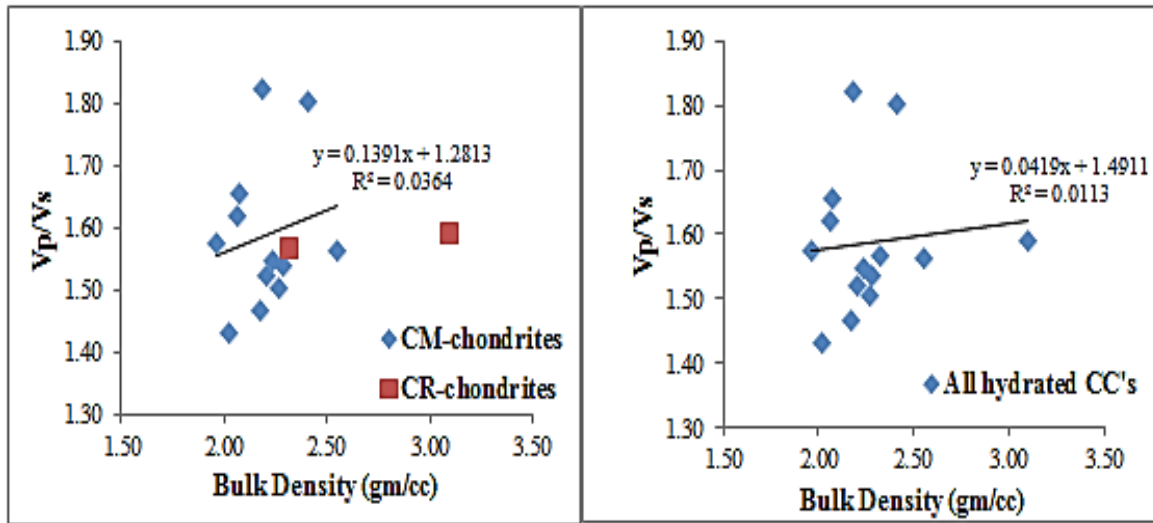
Figure (3.10): *Top*: Vp/Vs ratios versus bulk density for CM- and CR- chondrites separately (left), and for all the hydrated carbonaceous chondrites (right). PCC test show a very low statistical significance for Vp/Vs versus bulk density for CM-chondrites and all hydrated groups. *Bottom*: Vp/Vs ratios versus bulk density for CO-, CV-, and CK-chondrites separately (left), and for all the non-hydrated carbonaceous chondrites (right) show similarly a very low statistical significance for Vp/Vs versus bulk density for all non-hydrated groups. More data are required to test for this trend for CR- and CK-chondrites.
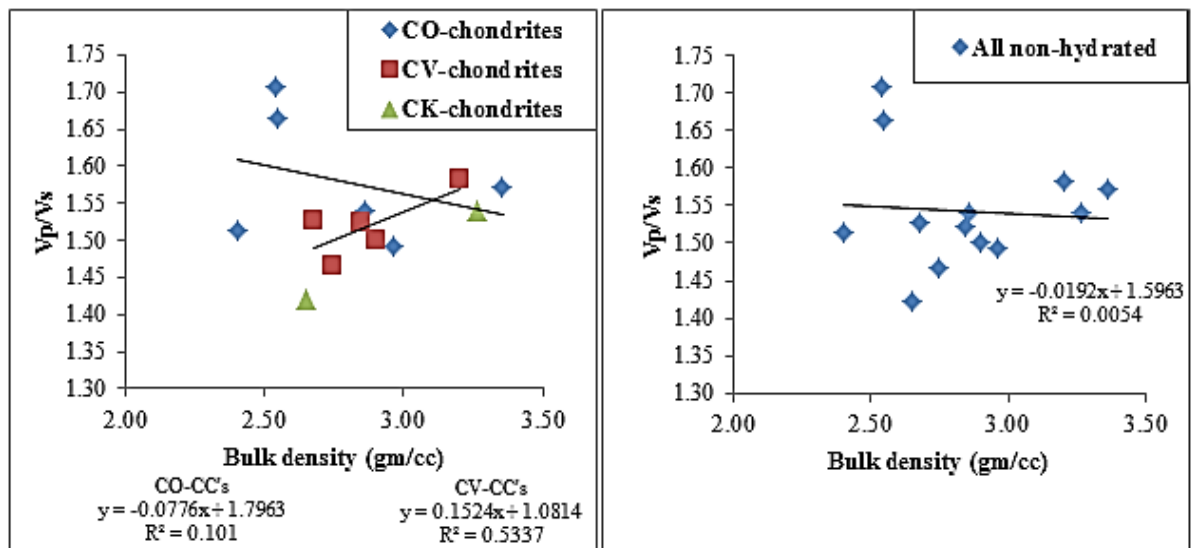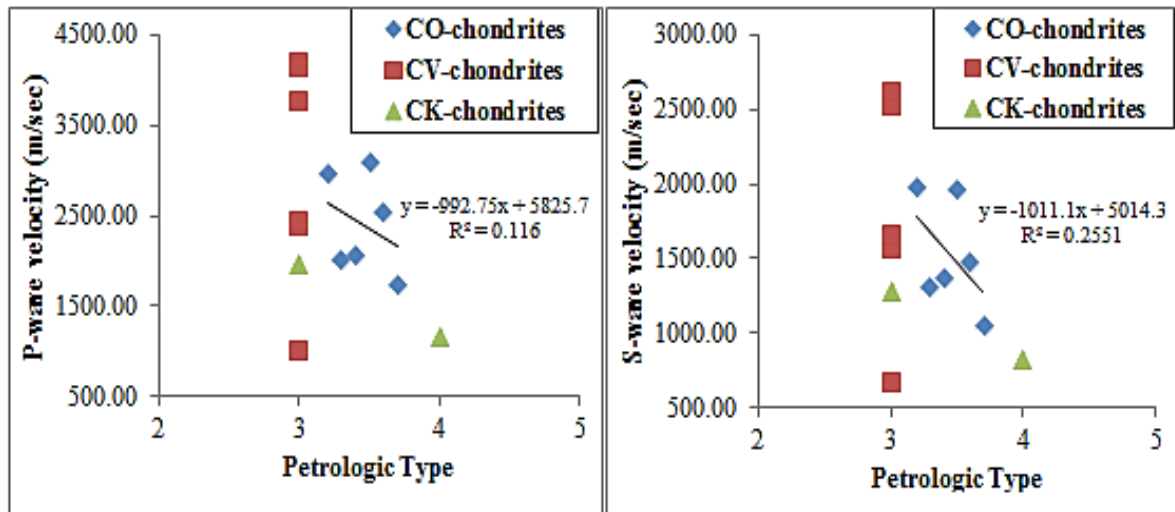
Figure (3.11): *Top*: Elastic wave velocities of CO-chondrites decrease with increasing the petrologic type from 3 to 4 showed low statistical significances of 49% for Vp and 69% for Vs versus petrologic type. The trend was not found for CV- and CK-chondrites since CV's are found as type 3 only, and more data is required for CK-chondrites. *Bottom*: the non-hydrated carbonaceous chondrites population show a statistically significant decrease of both P- and S-wave velocities with petrologic type (89% for Vp and 91% for Vs versus petrologic type). The low R^2 values are due to the large amount of scatter in the data. This trend was observed in ordinary chondrites from petrologic type 4 to 6 (Hons, 2004; Jones, 2009), and is not consistent with terrestrial rocks. Modifications in mineralogy associated with thermal metamorphism are believed to cause this trend as discussed in this section.
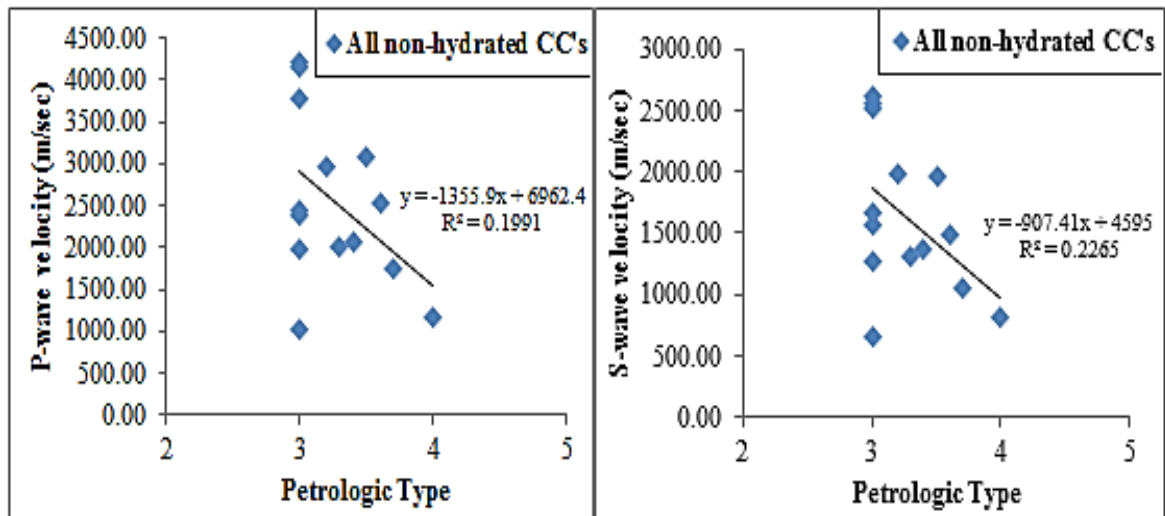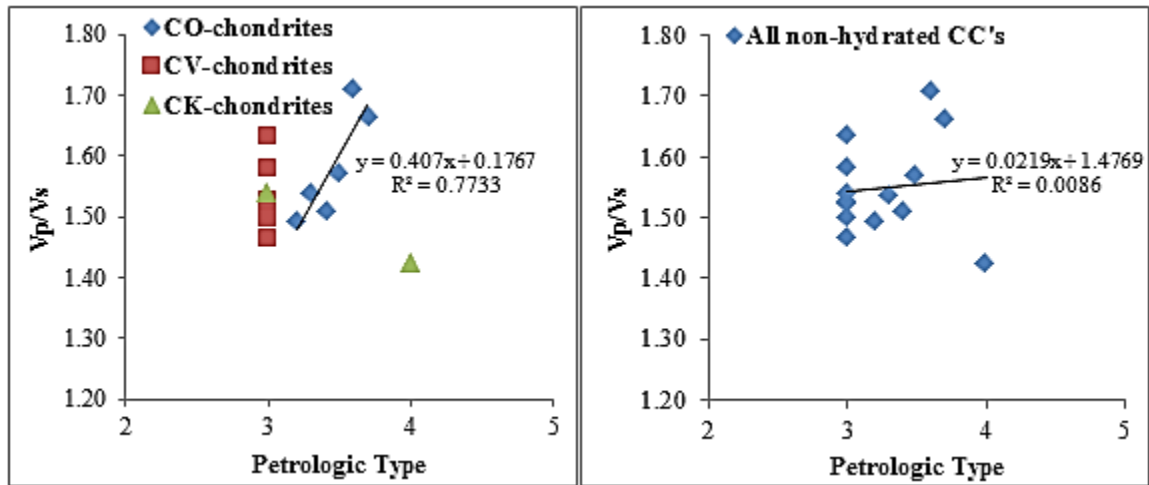
Figure (3.12): (left) *Vp/Vs* variation with petrologic type for CO-, CV- and CK-chondrites. More data points are required to confirm this trend for CK-chondrites (all CV-chondrites are type 3). The statistical significance was found to be unexpectedly high for CO-chondrites (98%). However, *right*: the total non-hydrated population showed a statistically weak correlation for Vp/Vs with petrologic type (24%).
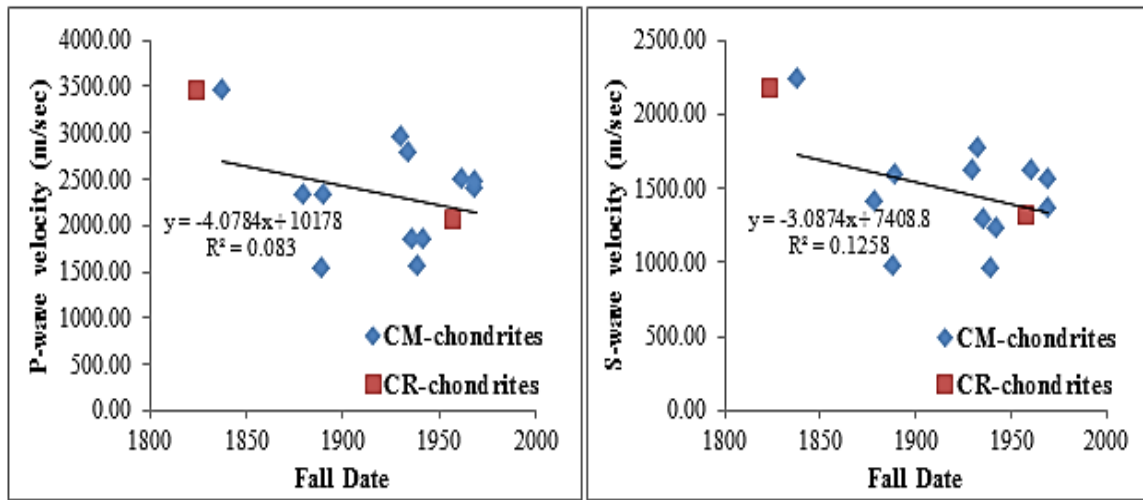
Figure (3.13): *Top*: P- and S- velocities decrease with fall dates for CM- chondrites. More data points are required to confirm this trend for CR-chondrites. The statistical significance was found to be low for CM-chondrites (64% for the Vp and 74% for the Vs versus fall date). *Bottom:* the hydrated carbonaceous chondrites population show a statistically significant decrease of P- and S-wave velocities with fall date (94% for Vp and 96% for Vs), which contrasts the low significance exhibited by CM-chondrites alone. The addition the two CR-chondrites seem to have changed the trend line substantially. The low R^2 values are due to the large amount of scatter in the data. It might be possible that the hydrated chondrites are less susceptible to terrestrial weathering because of their low metal content, thus oxidation products have less effect on porosity.
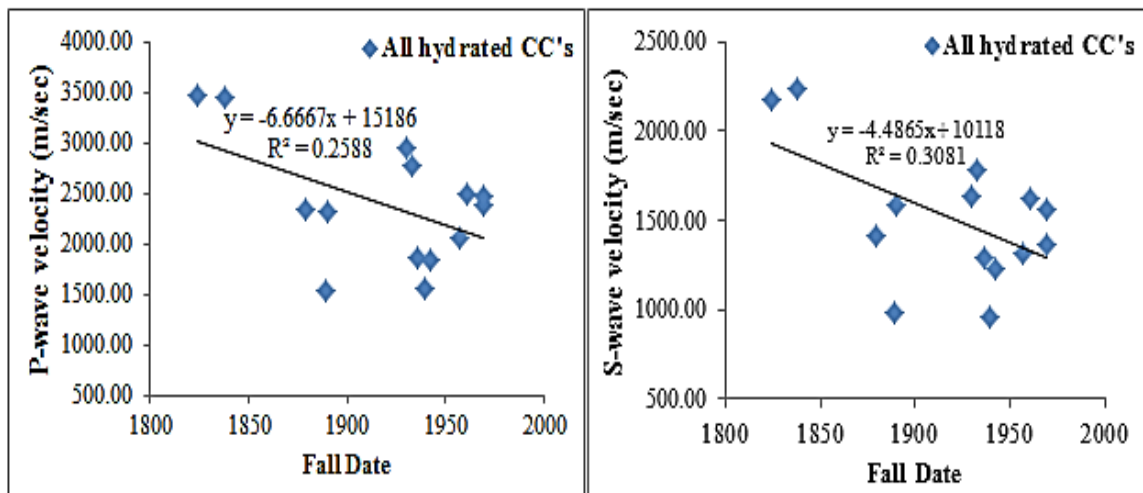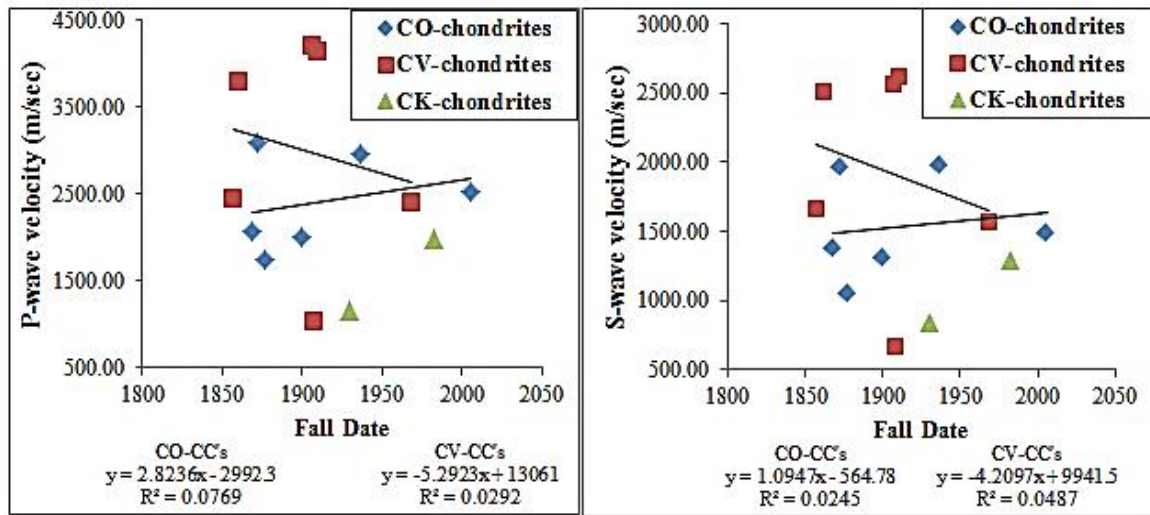
Figure (3.14): *Top*: P- and S- velocities decrease with fall dates for CO- and CV-chondrites. More data points are required to confirm this trend for CK-chondrites. The statistical significance was found to be low for CO-chondrites' trend line (41% for the Vp and 23% for the Vs versus fall date). *Bottom:* the non-hydrated carbonaceous chondrites population show a statistically non-significant decrease of P- and S-wave velocities with fall date (39% for Vp and 74% for Vs), which contrasts the low significance exhibited by CM-chondrites alone. The addition the two CR-chondrites seem to have changed the trend line substantially. The low R^2 values are due to the large amount of scatter in the data.
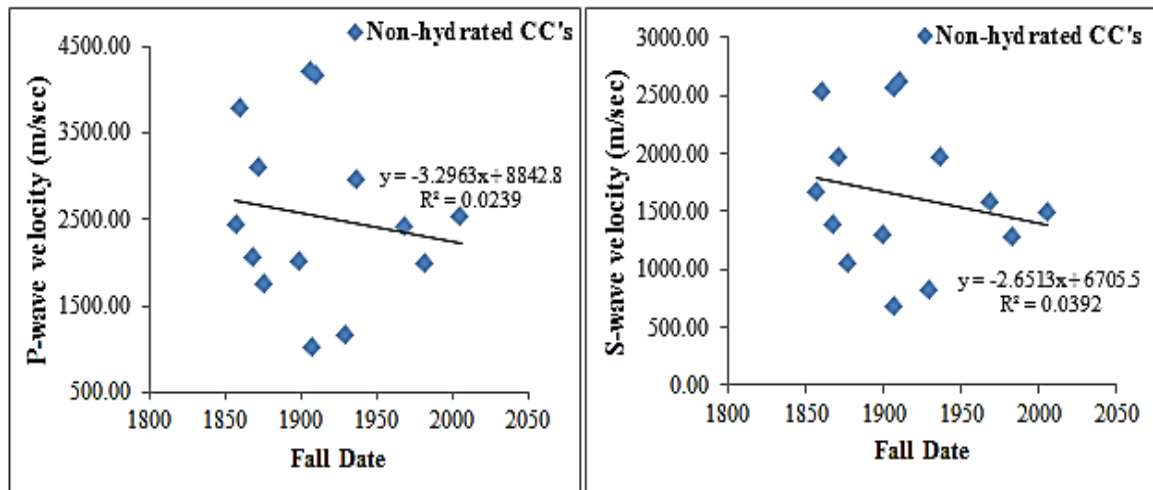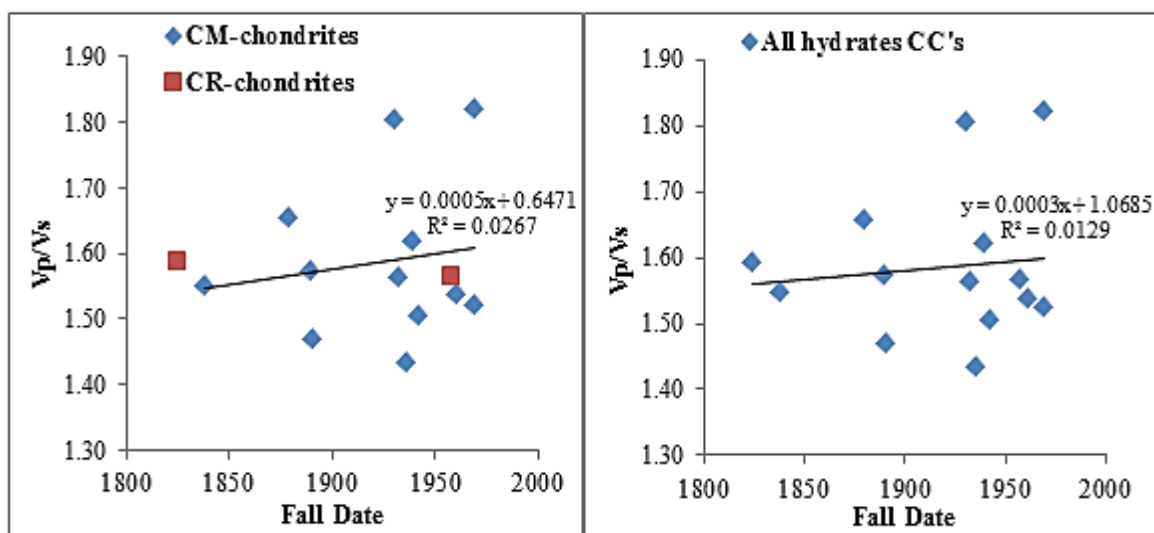
Figure (3.15): *Top*: Vp/Vs ratios variation with fall dates for hydrated carbonaceous chondrites. More data points are required to test this trend for CR-chondrites. The statistical significance was found to be low for CM-chondrites' trend line (39%) and even less significant for the whole hydrated population (30%). *Bottom:* the non-hydrated carbonaceous chondrites population shows an increase of Vp/Vs with fall date with statistical significances of 65% for CO-chondrites and 64% for the whole population. The large amount of scatter in the data is reflected by low R^2 values.
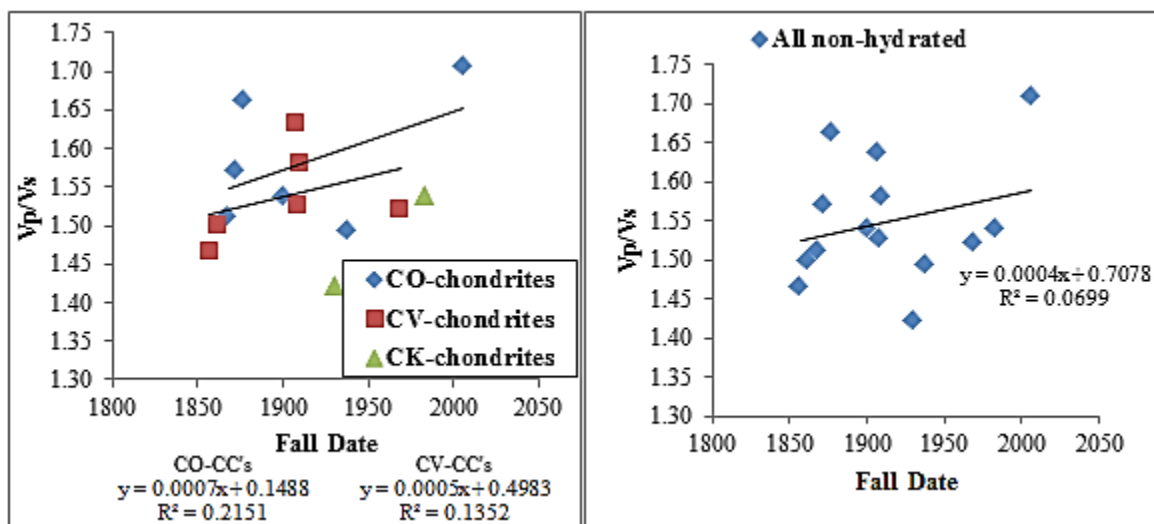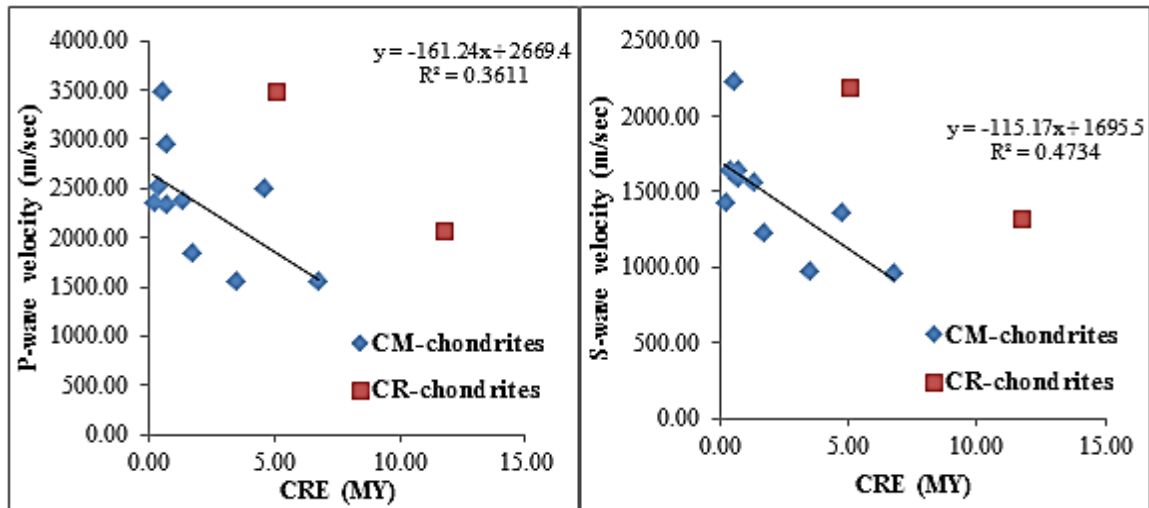
Figure (3.16): *Top:* P- and S- velocities decrease with cosmic ray exposure ages for CM-chondrites. CM-chondrites have 12 samples, which allows for a meaningful correlation; whereas, more data points are required to confirm this trend for CR-chondrites. The statistical significance was found to be 93% for the Vp versus CRE ages and 97% for the Vs versus CRE ages. *Bottom:* the whole population of hydrated carbonaceous chondrites shows a lesser statistically significant decrease of P- and S-wave velocities with CRE ages (65% for Vp and 68% for Vs versus CRE ages). The addition of the CR-chondrites with the longer CRE ages modified the trend significantly, which is expected since the significantly hydrated CM-chondrites have remarkably low CRE ages that coincide with their low strength. The low R^2 values are due to the large amount of scatter in the data.
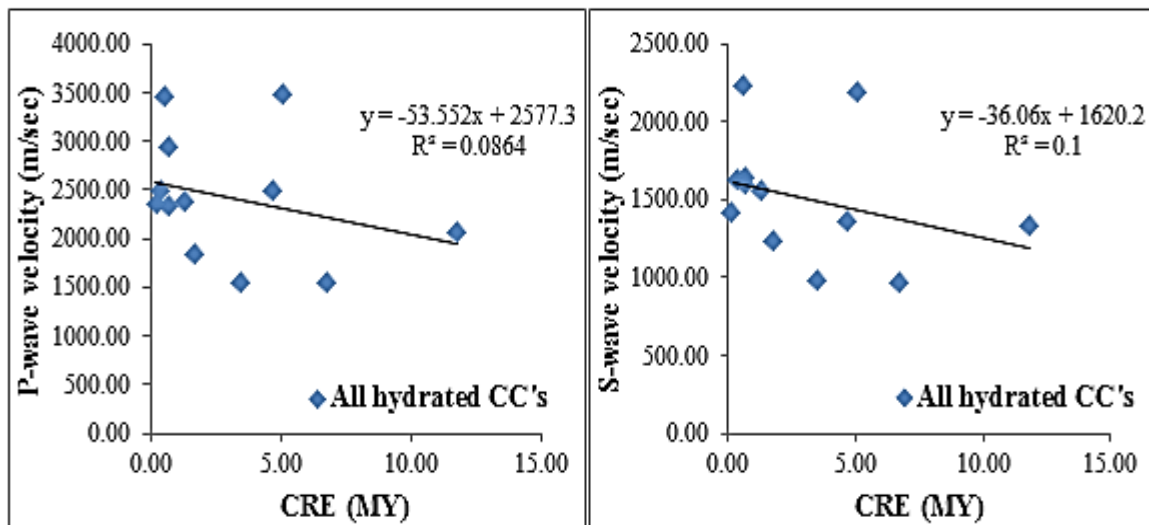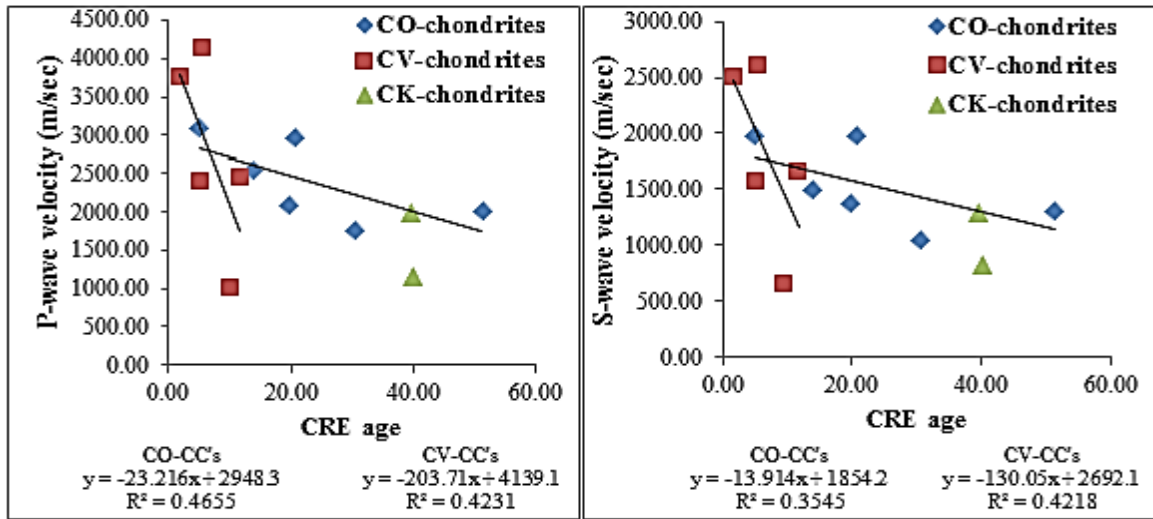
Figure (3.17): *Top:* P- and S- velocities decrease with cosmic ray exposure ages for CO-, CV-, and CK-chondrites. More data points are required to confirm this trend for CK-chondrites. CO-chondrites had a statistical significance of 86% for Vp and 78% for Vs versus CRE ages, while CV-chondrites yielded 84% for Vp and 84% for Vs versus CRE ages. *Bottom:* the whole population of non-hydrated carbonaceous chondrites show a high statistically significant decrease of P- and S-wave velocities with CRE ages (96% for Vp and 96% for Vs versus CRE ages). The low R^2 values are due to the large amount of scatter in the data.
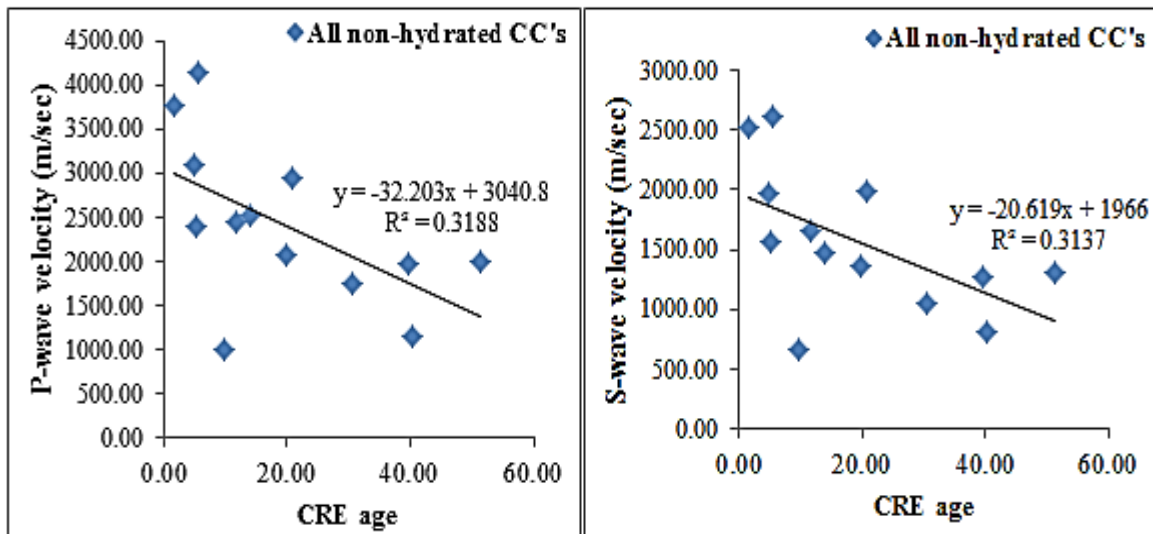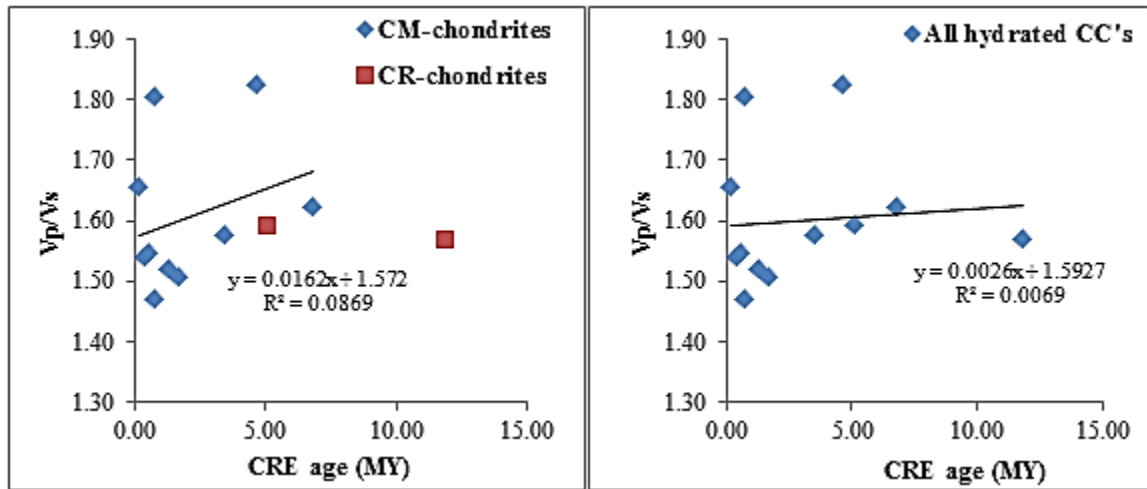
Figure (3.18): *Top*: Vp/Vs ratios variation with cosmic ray exposure ages for hydrated carbonaceous chondrites. More data points are required to test this trend for CR-chondrites. The statistical significance was found to be 60% for CM-chondrites' trend and less significant for the whole hydrated population (20%). *Bottom:* Vp/Vs ratios variation with cosmic ray exposure ages for hydrated carbonaceous chondrites. The trend has a low statistical significance for the non-hydrated carbonaceous chondrites with 25% for CO-chondrites, 49% for CV-chondrites, and 28% for the whole non-hydrated carbonaceous chondrites' population. The large amount of scatter in the data is reflected by low R^2 values.
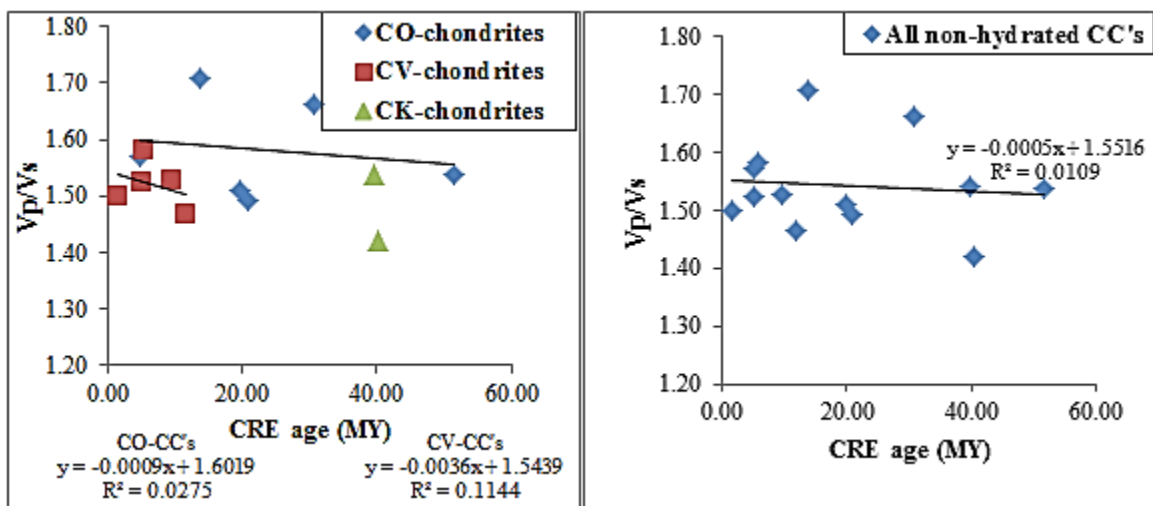
3.5 Summary

As mentioned at the beginning of this chapter, the main objective of this study was to measure the elastic properties of carbonaceous chondrites. This was accomplished by collecting elastic wave velocity and bulk density data for carbonaceous chondrite falls from three meteorites collections. The Archimedean method employing glass beads was applied to measure the bulk volume required to determine the bulk density, while the elastic wave velocities were measured using ultrasonic contact transducers, a pulse generator, and a digital oscilloscope (elastic waves travel time measurement), and a digital caliber (thickness measurement). The elastic moduli were then calculated using direct equations; thus, satisfying the main objective of this study.

The second objective was to examine the relationships among the elastic and physical properties of carbonaceous chondrites. First, through investigating previously identified trends in ordinary chondrites, which included: (1) elastic wave velocities increase with terrestrial weathering time (2) elastic wave velocities increase with bulk density, (3) elastic wave velocities decrease with metamorphic grade/ petrologic type, (4) elastic wave velocities increase with meteorite darkness in ordinary chondrite, (5) elastic wave velocity decreases as total porosity increases. Jones (2009) confirmed these trends and added: (6) bulk density decreases with terrestrial weathering time, (7) total porosity decreases with increasing shock state in H- and L-chondrites, (8) bulk density increases with petrologic type in H-chondrites, (9) Poisson's ratio and Vp/Vs ratio decrease with increasing petrologic type in H-chondrites and (10) Poisson's ratio and Vp/Vs ratio may decrease with increasing the porosity.

Since this study did not attempt to collect porosity data by measuring the grain density, no elastic property – porosity trends were identified. Darkness in carbonaceous chondrites is associated with inherent chemical composition (carbon content) more than acquired darkness because of shock or any other secondary processes; thus, no meaningful trend will be deduced by correlating darkness with elastic properties.

Three trends have been identified for the elastic properties of carbonaceous chondrites. First, the elastic wave velocities and derived elastic moduli were found to increase with increasing the bulk density for all carbonaceous chondrites, which is consistent with observations on terrestrial rocks, and ordinary chondrites. The bulk density values of the hydrated carbonaceous chondrites were lower than those of the non-hydrated. The second observed trend was that the elastic wave velocities and derived elastic moduli showed a reduction with increasing petrologic type in the non-hydrated carbonaceous chondrites (CO, CV, and CK-chondrites). Although this trend was observed only in the non-hydrated carbonaceous chondrite population (all hydrated being petrologic type 2), it still remains an interesting trend since it was previously reported in ordinary chondrites (Hons, 2004; Jones, 2009).

Third, the elastic wave velocities and derived elastic moduli decrease with increasing cosmic ray exposure (CRE) ages. This trend was not observed for the ordinary chondrites. This effect may be caused by damage induced by impacts with weaker objects; impacts that are strong enough to be recorded in the reduction of the elastic wave velocities, but not strong enough to cause total disruption. In the case of the CM-chondrites, these impacts will be caused by weaker objects, which are not found in our meteorite collections.

Chapter Four: Conclusions & Implications

The first chapter introduced asteroids within the solar system as key pieces in solving the mystery of solar system formation and evolution, as asteroids represent the remnants of primordial material that formed planets and satellites. Immense modifications occurred to these objects including dynamical, orbital and thermal processes that have contributed to their present state. Much of these modifications are governed by the collisional and accretionary processes that could observed from their current size distributions. Size distributions of asteroids, the ejecta fragments that were retained on asteroids' surfaces (boulders), as well as ejecta that have reached the Earth (meteorites), seem to follow similar power-law distributions over a wide range of sizes, from hundreds of kilometers down to sub-meter scales. However, these self-similar size distributions are influenced by the various lithologies found for these objects (meteorites and their parent bodies), as lithologies have a strong control on the fragmentation and ejecta production on asteroids.

An excellent example of the influence of lithology on ejecta production on asteroids' surfaces was reported in the flyby data of the C-type asteroid Mathilde. At least five giant impact craters were observed on Mathilde's surface from the imagery provided by NEAR-Shoemaker with a surprising absence of impact ejecta (Cheng and Barnouin-Jha, 1999). The craters' diameters - which were of sizes comparable to the size of Mathilde – are impressive since the asteroid should not be intact after such impacts, which implies the presence of mechanisms or certain physical characteristics enabling the survivability of Mathilde. A comparison of Mathilde with any Ida or Eros (both S-type

asteroids) supports this point since neither asteroid has such proportionally large craters, and both S-type asteroids have retained ejecta blankets that are visible and of predictable thickness using empirical models (e.g. Thomas et al., 2000). Mathilde's lithology is different being a dark asteroid and it has a remarkably low bulk density (~1.3 g/cm^3) implying potentially high macroporosity or microporosity. Whereas, both Eros and Ida would have been destroyed by such strong impacts, Mathilde's internal structure was capable of attenuating the shock and elastic waves and has endured such proportionally large impacts. Housen et al. (1999) explained the formation of the gigantic craters of Mathilde as a result of compaction, not excavation as in the cases of Eros and Ida. Macroporosity, if large enough, is postulated to influence the asteroid's internal structure and response to impact processes, and consequently controls the asteroid's collisional lifetime and survivability (Britt et al., 2001). Asteroids' responses to impact processes would therefore be controlled by their internal structure (micro- and macro-porosity) and their ability to transfer and attenuate elastic waves.

Small objects are continuously colliding with the Earth, and despite the vast majority of these impacts being of no critical threat to human civilizations, the largest of these impacts do pose a hazard to life on Earth. Understanding the impact process is not a trivial task since a wide range of potential conditions is involved. The crater size, shape, amount of compaction of the target rocks, and the volume, ejection velocity and deposition of ejecta around the crater are all factors that influence the outcome of the final crater size and shape (Michel and Morbidelli, 2007). Therefore, planning of any deflection missions of the NEA is not as straightforward as targeting a NEA object with a missile to deflect it, but they present another approach to study cratering processes under

110

a different light. Even if the science and technology required to deflect a small solar system object were to be available, and the required trajectory deflection magnitude and direction were determined, it will still be difficult to predict accurately how much energy and momentum are needed in an impact to accomplish a deflection successfully. This knowledge gap results from the incomplete understanding of hypervelocity impacts and the lack of data on the physical and elastic properties that control the transfer of momentum within the target objects.

As an attempt to lessen this gap, this study aimed to gain an adequate understanding of the elastic properties of the dark asteroids population through a systematic survey of their closest analogues, the carbonaceous chondrite meteorites. This was accomplished by acquiring data on a total of 49 samples of 28 carbonaceous chondrite falls at three major meteorite collections. Non-destructive ultrasonic measurement techniques provided compressional and shear wave velocities that were combined with bulk density values to provide the elastic moduli (Tables 4.1 and 4.2).

CC Clans	# Of Samples	Bulk Density (g/cc)	P-wave Velocity (m/sec)	S-wave Velocity (m/sec)	V_p/V_s
CM	12	2.20 ± 0.05	2335 ± 165	1472 ± 102	1.59
CO	6	2.78 ± 0.14	2401 ± 223	1526 ± 153	1.58
CV, CK, CR	9	2.86 ± 0.10	2664 ± 371	1721 ± 228	1.54
Hydrated	12	2.20 ± 0.05	2335 ± 165	1472 ± 102	1.59
Non-hydrated	15	2.83 ± 0.08	2566 ± 243	1648 ± 152	1.55

Table (4.1): shows the mean values of the bulk density, elastic wave velocities, and Vp/Vs ratios for the different groups of carbonaceous chondrites collected in this study.

CC clans	# of Samples	Shear Modulus (GPa)	Bulk Modulus (GPa)	Lamé's Parameter	Poisson' Ratio	Young Modulus (GPa)
CM	12	5.11 ± 0.76	6.11 ± 1.02	2.7 ± 0.67	0.16 ± 0.02	11.8 ± 1.8
CO	6	7.07 ± 1.71	7.89 ± 1.73	3.18 ± 0.80	0.16 ± 0.02	16.2 ± 3.8
CV	5	11.24 ± 3.86	11.37 ± 4.38	3.88 ± 1.92	0.13 ± 0.02	25.3 ± 8.9
CV,CK, CR	9	9.12 ± 2.5	9.53 ± 2.83	3.45 ± 1.24	0.13 ± 0.02	20.7 ± 5.8
Hydrated	12	5.11 ± 0.76	6.11 ± 1.02	2.7 ± 0.67	0.16 ± 0.02	11.8 ± 1.8
Non-hydrated	15	8.3 ± 1.62	8.88 ± 1.80	3.34 ± 0.78	0.14 ± 0.01	18.9 ± 3.7
Ordinary chondrites	99	11.73 ± 0.98	20.01 ± 1.82	12.19 ± 1.31	0.24 ± 0.01	28.81 ± 2.4

Table (4.2): shows the mean values of the elastic moduli acquired for the different groups of carbonaceous chondrites collected in this study.

Three trends have been identified for the elastic properties of carbonaceous chondrites. First, the elastic wave velocities and derived elastic moduli were found to increase with increasing the bulk density for all carbonaceous chondrites. This is consistent with observations on terrestrial rocks, and ordinary chondrites, and is expected based on Nafe-Drake bulk density-elastic velocity equations (Knopoff, 1967). The bulk density values of the hydrated carbonaceous chondrites were lower than those of the non-hydrated, which was also reported in previous literature (Consolmagno and Britt, 2002; Macke et al, 2011). Based on these observations, a valid speculation would be that asteroids would exhibit similar elastic wave velocity – bulk density trends by enhancing elastic waves propagation in highly dense objects (e.g. monoliths), and attenuating elastic waved in object with existing (micro and macro) porosity (C-type asteroids and rubble-pile asteroids). Considering the case of Mathilde, aside from possible compaction being the result of attaining such huge impacts without the disruption of Mathilde, a possible speculation would be that the shock waves from the catastrophic impacts suffered high attenuation through the highly porous (low density) asteroid, which reduced the impact efficiency as most of the impact energy was attenuated within the object.

The second observed trend was that the elastic wave velocities and derived elastic moduli showed a reduction with increasing petrologic type in the non-hydrated carbonaceous chondrites (CO, CV, and CK-chondrites). Although this trend was observed only in the non-hydrated carbonaceous chondrite population (all hydrated being petrologic type 2), it still remains an interesting trend since it was previously reported in ordinary chondrites (Hons, 2004; Jones, 2009). Petrologic type for meteorites is equivalent to the grade of thermal metamorphism (or aqueous alteration for types 1 and

2). In terrestrial rocks, thermal metamorphism results in increasing the elastic wave velocities caused by recrystallization of the grains, and the associated reduction of porosity. In meteorites, thermal metamorphism results in many modifications; such as, textural integration, phase transformation, and changes in mineral compositions. All of those changes might lead to the observed trend, but this needs further investigation that is outside of the scope of this work. In the author's opinion, since matrices of meteorites recrystallize with thermal metamorphism as reported in previous studies (e.g., Huss et al., 2006), elastic waves will have to travel through a more heterogeneous medium. This will increase the travel time required to pass through the medium as opposed to going through the more homogenous matrix of lower – petrologic type meteorites.

Third, the elastic wave velocities and derived elastic moduli decrease with increasing cosmic ray exposure (CRE) ages for all carbonaceous chondrite groups. This trend was not observed for H- chondrites' compiled elastic velocity data and CRE ages from the literature. In carbonaceous chondrites, this correlation holds true for the CM-clan with a maximum CRE age of only ~2 M.Y., and the observed velocity reductions are ~ 2/3 of the velocity variations found amongst the carbonaceous chondrites. This effect may be caused by damage induced by impacts with weaker objects. These impacts were not strong enough to cause total disruption, but were strong enough to modify the elastic properties of meteorites. In the case of the CM-chondrites, these impacts will be caused by weaker objects, which are not found in our meteorite collections. The postulated weaker objects that are damaging the hydrated carbonaceous chondrites are evidenced in the observed fireball population, which records many objects that fragment more easily than recovered meteorites. An unbiased fireball survey reveals that ~50% of fireballs

represent bodies weaker than hydrated carbonaceous chondrites with 2/3rds cometary and 1/3rd Main Asteroid Belt origins (Figure 4.1).
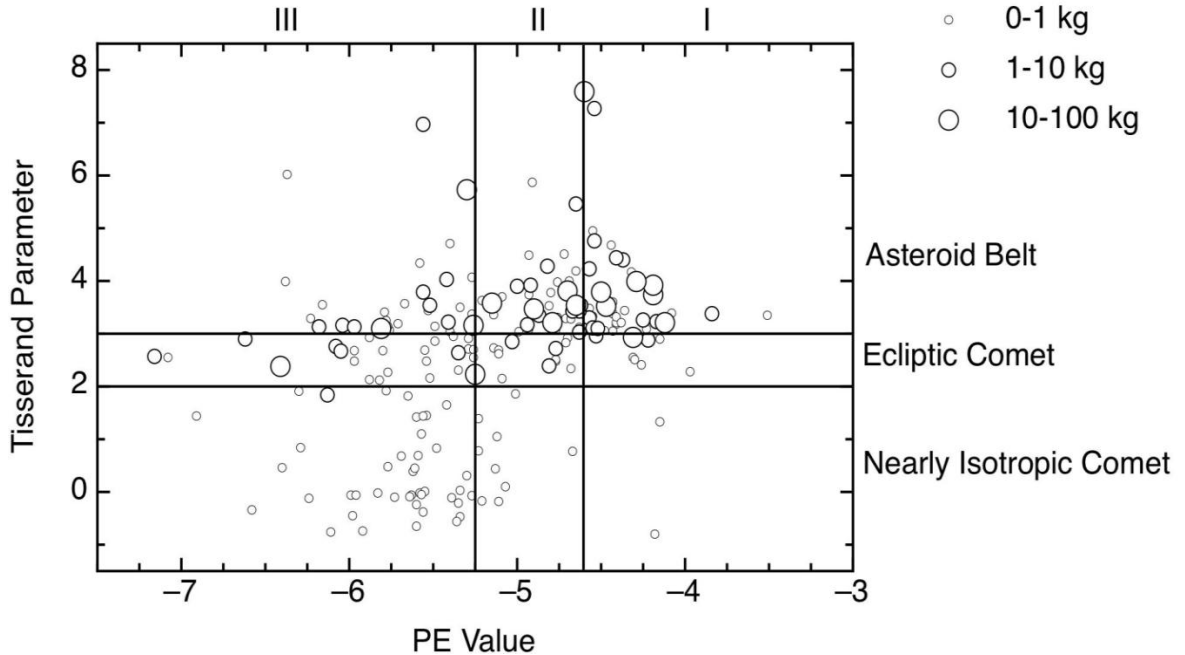
Figure (4.1): Plot of MORP Clear-Sky Survey events in Tisserand parameter and PE criterion space. Circles represent meteoroid masses described in legend. Note that there is very weak material originating in the Asteroid Belt, and similarly there is very strong nearly isotropic comet material (Adopted from Milley, 2010).

The above plot shows Tisserand parameter (which is commonly used to distinguish source region) plotted against the PE criterion (which is related to meteoroid strength) for events included in the unbiased MORP Clear-Sky Survey. The vertical lines divide the object material by PE values (types I through III) and the horizontal lines divide source region by Tisserand parameter (Asteroid Belt, Kuiper Belt or scattered disk and Oort cloud). Each of the divisions corresponds to material strength within a source region. The size of the symbol relates to the object mass. Traditionally, asteroidal

115

material is thought to be strongest, made of stones and some carbonaceous material; whereas, comets are made of icy material. The trends between material type and source region agree in that material arriving from the main belt of asteroid is stronger, goes deeper into the atmosphere and corresponds to types I and II fireballs, while cometary material is weaker, less penetrating and corresponds to types II and III fireballs.
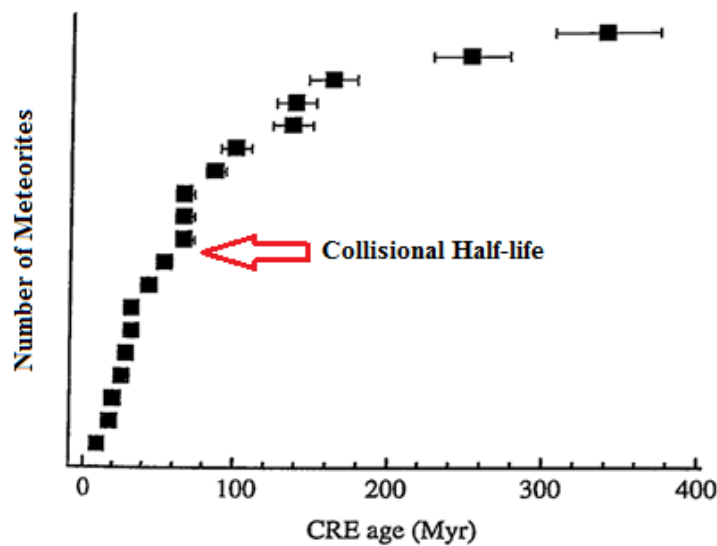
Figure (4.2): shows comic ray exposure ages for Mesosiderites (Herzog, 2003). The Collisional half-life is defined as the period of time by which the amount of any material is reduced by half. In the case of meteorites, it means the amount of time required for half the meteorites to be destroyed by collisional processes (Figure adapted from Herzog, 2003).

Meteoroid lifetime models have been based on CRE "survivorship" lifetimes, or collisional half-lives. A collisional half-life is the period of time that it takes for a certain type of meteorites undergoing collisions to decrease by half due to total disruption (Figure 4.2). The variations in collisional half-lives recorded by CRE ages from iron

meteorites to stony meteorites (ordinary chondrites and HED's) to hydrated carbonaceous chondrites have been suggested to correspond to their respective strengths. The velocity data imply that the carbonaceous chondrites are weak enough to have their elastic properties modified by collisions, and that such collisions are frequent relative to the timescales of ordinary chondrite - HED meteorites' half-lives of 10 – 20 MY. Non-destructive collisions' frequencies are about 1–2 MY implied by the CM-chondrites' elastic wave velocity – CRE correlation (Table 4.3).

	Weaker unsampled objects	Hydrated CC's	OC-HED	Iron meteorites
Mean CRE (MY)	Unknown	2	17	500
$T_{1/2}$ Collisions (MY)	Unknown	1.3	11	300
Weak impacts/$T_{1/2}$	Unknown	1-2	7	200
Hydrated impacts/$T_{1/2}$	~1	~1	9	250
OC-HED impacts/$T_{1/2}$	<1	<1	~1	27
Irons impacts/$T_{1/2}$	<1	<1	<1	~1
Impacts/ 100 MY	66	82	9	0.3

Table (4.3): Collisional half-lives and mutual impact rates between major meteorite classes: Weak unsampled material, the hydrated carbonaceous chondrites (CM-chondrites only), ordinary chondrites and HED meteorites, and Iron meteorites. Note that the stronger bodies survive many non-destructive impacts.

LIST OF REFERENCES

1. Abe, M., Yoshikawa, M., Sugita, S., Namiki, N., Kitazato, K., Okada, T., Tachibana, S., Arakawa, M., Honda, R., Ohtake, M., Tanaka, S., Fukuhara, T., Takagi, Y., Kadono, T., Okazaki, R., Yano, H., Demura, H., Hirata, N., Nakamura, R., Sawada, H., izuno, T., Iwata, T., Saiki, T., Nakazawa, S., Iijima, Y., Hayakawa, M., Kobayashi, N., Mitani, T., Shirai, K., Ogawa, K., and Hayabusa-2 Science Team. 2012. Hayabusa-2, C-type asteroid sample return mission, science targets and instruments. *Asteroids, Comets and Meteors meeting* 2012. Abstract ID 6137.

2. Alexayeve, K. N. 1958. Physical properties of stony meteorites and their interpretation based on the hypothesis on the origin of meteorites. *Meteoritika*, **16**: 67-77.

3. Alexeyeva, K. N. 1960. New data on physical properties of stony meteorites, Meteoritika, **18:** 68-76.

4. Anders, E. 1964. Origin, age, and composition of meteorites. *Space Science Reviews*. **3**: 583-714.

5. Bland, P. A., Zolensky, M. E., Benedix, G. K., & Sephton, M. A. 2006. Weathering of chondritic meteorites. In D. S. Lauretta, & H. Y. McSween (Eds.), *Meteorites and the Early Solar System II* (pp. 853-867). Tucson: University of Arizona Press.

6. Bottke, W. F., Cellino, A., Paolicchi, P., & Binzel, R. P. 2002. An Overview of the Asteroids: The Asteroids III Perspective. In W. Bottke, A. Cellino, P. Paolicchi, & R. Binzel (Eds.), *Asteroids III* (pp. 3-15). Tucson: University of Arizona Press.

7.   Brearley, A. J. 2006. The Action of Water. In D. S. Lauretta, & H. Y. McSween (Eds.), *Meteorites and the Early Solar System II* (pp. 587-624). Tucson: University of Arizona Press.

8.   Britt, D. T., & Consolmagno, G. J. 2003. Stony meteorite porosities and densities: A review of the data through 2001. *Meteoritics & Planetary Science*, **38**: 1161-1180.

9.   Britt, D. T., Yeomans, D., Housen, K., & Consolmagno, G. 2002. Asteroid density, porosity and structure. In W. Bottke, A. Cellino, P. Paolicchi, & R. Binzel (Eds.), *Asteroids III* (pp. 485-500). Tucson: University of Arizona Press.

10.   Britt, D. T. and Consolmagno, G. J. 2000. The porosity of dark meteorites and the structure of low-albedo asteroids. *Icarus*, **146**: 213-219. 12.

11.   Britt, D. T. and Consolmagno, G. J. 1997. The porosity of meteorites and asteroids: Results from the vatican collection of meteorites, *Lunar and Planetary Science*, **28**: 159-160.

12.   Brown P. G., Hildebrand A. R., Zolensky M. E., Grady M., Clayton R. N., Mayeda T. K., Tagliaferri E., Spalding R., MacRae N. D., Hoffman E. L., Mittlefehldt D. W., Wacker J. F., Bird J. A., Campbell M. D., Carpenter R., Gingerich H., Glatiotis M., Greiner E., Mazur M. J., McCausland P.J., Plotkin H., Rubak Mazur T. 2000. The fall, recovery, orbit and composition of the Tagish Lake meteorite: A new type of carbonaceous chondrite. *Science* **290**, 320–325.

13.   Brown, P., R. E. Spalding, D. O. ReVelle, E. Tagliaferri, and Worden, S. P. 2002. The flux of small near-Earth objects colliding with the Earth. *Nature* **420:** 294–296.

14. Burbine, T. H., McCoy, T. J., Meibom, A., Gladman, B., & Keil, K. 2002. Meteoritic Parent Bodies: Their Number and Identification. In W. Bottke, A. Cellino, P. Paolicchi, & R. Binzel (Eds.), *Asteroids III* (pp. 653-667). Tucson: University of Arizona Press.

15. Burdine, N.T. 1963. Rock Failure under Dynamic Loading Conditions. *SPE Journal* **3**, Number 1.

16. Bus S. J., Vilas F., and Barucci M. A. 2002. Visible-wavelength spectroscopy of asteroids. In W. Bottke, A. Cellino, P. Paolicchi, & R. Binzel (Eds.), *Asteroids III* (pp. 169-182). Tucson: University of Arizona Press.

17. Ceplecha Z., and McCrosky R. E. 1976. Fireball End Heights: A Diagnostic for the Structure of Meteoric Material. *Journal of Geophysical Research*, **81**:6257–6275.

18. Cheng A. F. and Barnouin-Jha O. 1999. Giant craters on Mathilde. *Icarus* **140**:34–48.

19. Clayton R. N., Mayeda T. K. 1999. Oxygen isotope studies of carbonaceous chondrites. Geochim Cosmochim Acta 63:2089-2104

20. Clayton RN (2005) Oxygen isotopes in meteorites. In: Davis AM (ed) Meteorites, comets and planets, vol 1, *Treatise on geochemistry*. Elesevier-Pergamon, Oxford, pp 129–142.

21. Consolmagno, G. J., & Britt, D. T. 1998. The density and porosity of meteorites from the Vatican collection. *Meteoritics & Planetary Science*, **33**: 1231-1241.

22. Consolmagno, G. J., Britt, D. T., & Stoll, C. P. 1998. The porosities of ordinary chondrites: Models and interpretation. *Meteoritics & Planetary Science*, **33:** 1221-1229.

23. Consolmagno G. J., Macke R. J., Rochette P., Britt D. T., and Gattacceca J. 2006. Density, magnetic susceptibility, and the characterization of ordinary chondrite falls and showers. *Meteoritics & Planetary Science* **41**:331–342

24. Consolmagno, G. J., Britt, D. T., & Macke, R. J. 2008. The significance of meteorite density and porosity. *Chemie der Erde - Geochemistry*, **68:** 1-29.

25. Corrigan, C. M., Zolensky, M. E., Dahl, J., Long, M., Weir, J., Sapp, C., et al. (1997). The porosity and permeability of chondritic meteorites and interplanetary dust particles. *Meteoritics & Planetary Science*, **32**: 509-515.

26. De Leon J., Pinilla Alonso N., Licandro J., Campins H., Marzo G. A., 2012. Near-infrared spectroscopic survey of B-type asteroids: Compositional analysis. *Icarus*, **218**: 196.

27. Eugster O. (2003) Cosmic-ray exposure ages of meteorites and lunar rocks and their significance. *Chem. Erde/Geochemistry,***63**, 3–30.

28. Eugster O., Herzog G. F., Marti K., and Caffee M. W. 2006. Irradiation records, cosmic-ray exposure ages and transfer times of meteorites. In Meteorites and the early solar system II, edited by Lauretta D. S. and McSween H. Y. Jr., Tucson: The University of Arizona Press. 829–851.

29. Flynn, G.J., Moore, L.B., and Klock, W. 1999. Density and porosity of stone meteorites: Implications for the density, porosity, cratering, and collisional disruption of asteroids, *Icarus*, **142**: 97-105.

30. Fujiwara, A., Kawaguchi, J., Yeomans, D. K., Abe, M., Mukai, T., Okada, T., Saito, J., Yano, H., Yoshikawa, M., Scheeres, D. J., Barnouin-Jha, O. S., Cheng, A. F., Demura, H., Gaskell, R. W., Hirata, N., Ikeda, H., Kominato, T., Miyamoto, H.,

Nakamura, A. M., Nakamura, R., Sasaki, S., & Uesugi, K. 2006. The Rubble-Pile Asteroid Itokawa as Observed by Hayabusa. *Science*, 312, 1330

31. Gladman, B.J., Davis, D.R., Neese, C., Jedicke, R., Williams, G., Kavelaars, J.J., Petit, J-M., Scholl, H., Holman, M., Warrington, B., Esquerdo, G., and Tricarico, P. 2009. Sub-Kilometer Asteroid Diameter Survey (SKADS) V1.0. EAR-A-I0655-5-SKADS-V1.0. *NASA Planetary Data System*.

32. Grady, M. M. (2000). Catalogue of Meteorites (5th edn.). Cambridge: Cambridge University Press.

33. Halliday, I., Griffin, A. A., and Blackwell, A. T. 1996. Detailed data for 259 fireballs from the Canadian camera network and inferences concerning the influx of the large meteoroids. *Meteoritics & Planetary Science*, **31**:185–217.

34. Hamburger, M., (2000). Stress, Strain, and the Physics of Earthquake Generation. Image curtsey NASA Jet Propulsion Laboratory. Accessed June 2012:

     http://www.indiana.edu/~volcano/notes/handout1.htm

35. Harris, A. W. (2002). A New Estimate of the Population of Small NEAs. *Bulletin of the American Astronomical Society* **34**, 835.

36. Hartmann, W. K, and Hartmann A. C. 1968. Asteroid collisions and evaluation of asteroidal mass distribution and meteoritic flux. Icarus, **8**: 361 − 381.

37. Hartmann, W. K. (1969) Terrestrial, lunar, and interplanetary rock fragmentation. *Icarus*, **10**: 201-213.

38. Herzog G. F. (2003) Cosmic-ray exposure ages of meteorites. In Treatise on Geochemistry, Vol. 1: Meteorites, Comets, and Planets (A. M. Davis, ed.), pp. 347–380. Elsevier, Oxford.

39. Hildebrand, A. R., McCausland, P. J. A., Brown, P. G., Longstaffe, F. J., Russell, S. D. J., Tagliaferri, E., Wacker, J. F., and Mazur M. J. 2006. The fall and recover of the Tagish Lake meteorite. *Meteoritics & Planetary Science*, **41**:407–431.

40. Hirayama K. 1918. Groups of asteroids probably of common origin. *Astron. J.,* **31:** 185−188.

41. Hiroi, T. and Hasegawa S. (2003) Revisiting the search for the parent body of the Tagish Lake meteorite: Case of a T/D asteroid 308 Polyxo. *Antarctic Meteorite Research.* **16**: 176-184.

42. Hogg, R. 2008. Issues in particle size analysis. *KONA Powder and Particle Journal*, **26**: 81 − 93.

43. Hons, M. 2004. *Compressional and shear wave velocity in meteorites*. B.Sc. Thesis, Department of Geology and Geophysics, University of Calgary, Calgary, Alberta.

44. Hons, M. and Hildebrand, A. 2004. Compressional and shear wave velocities in meteorites. *Lunar and Planetary Science XXXV*, Houston: Abstract no. 2059.

45. Housen, K.R., Holsapple, K.A., and M.E., Voss, 1999. Compaction as the origin of the unusual craters on the asteroid Mathilde. *Nature*, **402**: 155-157.

46. Huss G.R., Rubin A.E., Grossman J.N. 2006. Thermal metamorphism in chondrites. In D. S. Lauretta, & H. Y. McSween (Eds.), *Meteorites and the Early Solar System II* (pp. 567-586). Tucson: University of Arizona Press.

47. Ivezi´c, ˇZ., Tabachnik, S., Rafikov, R., Lupton, R. H., Quinn, T., Hammergren, M., Eyer, L., Chu, J., Armstrong, J. C., Fan, X., Finlator, K., Geballe, T. R., Gunn, J. E., Hennessy, G. S., Knapp, G. R., Leggett, S. K. Munn, J. A., Pier, J. R., Rockosi, C. M., Schneider, D. P. Strauss, M. A. Yanny, B. Brinkmann, J. Csabai, I.,

Hindsley, R. B., Kent, S. Lamb, D. Q. Margon, B. McKay, T. A., Smith, J. A., Waddel, P., York, D. G., and the SDSS Collaboration (2001). Solar System Objects Observed in the Sloan Digital Sky Survey Commissioning Data. *AJ* 122, 2749–2784.

48.   Jones S. F. 2009. Elastic Wave Velocity, Porosity, and Pore Geometry of Ordinary Chondrites and Artificially Shocked Samples. M.Sc. Thesis. University of Calgary, Canada, 202 p.

49.   Jones, S. F. and Hildebrand, A. R. 2008. Acoustic Velocity Trends, Porosity, and Pore Geometry in Ordinary Chondrites: Implications for Meteorite and Meteorite Parent Body Elastic Properties. *Meteoritics and Planetary Science Supplement*, **43**, paper ID. 5040.

50.   Kanamori, H., Nur, A., Chung, D. H., and Simmons, G., 1970. Elastic wave velocities of lunar samples at high pressures and their geophysical implications, *Proc. Apollo 11 Lunar Sci. Conf.*, 2289-2293.

51.   Knopoff, L. 1967. Density − Velocity Relations for Rocks. *Geophys. J. astr. Soc.* **13**, 1 − 8.

52.   Kohout, T., G. Kletetschka, T. Elbra, T. Adachi, V. Mikula, L.J. Pesonen, P. Schnabl and S. Slechta, 2008. Physical properties of meteorites − applications in space missions to asteroids. *Meteoritics & Planetary Science*, **43**, 1009-1020.

53.   Lakes, R. 1991. Meaning of Poisson's Ratio. University of Wisconsin. http://silver.neep.wisc.edu/~lakes/PoissonIntro.html (accessed: June 1st, 2012).

54. La Spina, A., and Paolicchi, P. 1996. Catastrophic fragmentation as a stochastic process: Sizes and shapes of fragments. *Planetary and Space Science*, **44**: 1563–1578.

55. Lauretta, D. S., and McSween, H. Y. 2006. Preface to Meteorites and the Early Solar System II. In D. S. Lauretta, & H. Y. McSween (Eds.), *Meteorites and the Early Solar System II* (pp. xv-xvii). Tucson: University of Arizona Press.

56. Li Y-G, Vidale J.E. and Cochran E.S. (2004). Low-velocity damaged structure of the San Andreas Fault at Parkfield from fault zone trapped waves. *Geophysical Research Letters,* **31**, L12S06, doi: 10. 1029/2003GL019044.

57. Lee, P., Veverka, J., Thomas, P., Helfenstein, P., Belton, M. J. S., Chapman, C., Greeley, R., Pappalardo, R., Sullivan, R., and Head J. W.III. 1996. Ejecta Blocks on 243 Ida and On Other Asteroids. *Icarus*. **120:** 87−105.

58. Lewis, J. S. 2004. Physics and Chemistry of the Solar System. Elsevier Academic Press revised 2nd edition. 655 pp.

59. Lowrie, W. 1997. Fundamentals of Geophysics. Cambridge University Press, United Kingdom: 368 pp.

60. Macke, R., Britt, D., and Consolmagno, G. 2008. Density and porosity of shower meteorites as indicators of meter-scale asteroid homogeneity. *Bulletin of the American Astronomical Society*, *40***:** 455, abstract #33.02.

61. Macke, R. J., Britt, D. T., & Consolmagno, G. J. 2010a. Analysis of systematic error in "bead method" measurements of meteorite bulk volume and density. *Planetary and Space Science*, **58**, 421-426.

62. Macke, R. J., Britt, D. T., & Consolmagno, G. J. 2010b. Using grain density and magnetic susceptibility to quantify weathering in chondrite finds. *Meteoritics & Planetary Science*, **45**, Supplement, A124 (abstract #5155).

63. Macke, R. J., Consolmagno, G. J., Britt, D. T., & Hutson, M. L. 2010c. Enstatite chondrite density, magnetic susceptibility and porosity. *Meteoritics & Planetary Science*, **45**: 1513–1526.

64. Macke, R. J., Britt, D. T., & Consolmagno, G. J. 2010d. Density, porosity and magnetic susceptibility of achondritic meteorites. *Meteoritics & Planetary Science,* **46**: 311–326.

65. Macke, R. J., Consolmagno, G. J, and Britt, D. T. 2011. Density, porosity, and magnetic susceptibility of carbonaceous chondrites. *Meteoritics & Planetary Science,* **46**, 12: 1842–1862.

66. Marzari F., Davis D. R., and Vanzani V. 1995. Collisional evolution of asteroid families. *Icarus,* **113***,* 168–187.

67. Marzari F., Farinella P., and Davis D. R. 1999. Origin, aging and death of asteroid families. *Icarus* **142***,* 63–77.

68. Masiero, J. R., Mainzer, A. K., Grav, T., J. M. Bauer, R. M. Cutri, J. Dailey, P. R. M. Eisenhardt, McMillan, R. S., Spahr, T. B., Skrutskie, M. F., Tholen, D., Walker, R. G., Wright, E. L., DeBaun, E., Elsbury, D., Gautier IV, T., Gomillion, S., Wilkins. A. 2011. Main Belt Asteroids with WISE/NEOWISE I: Preliminary Albedos and Diameters. *The Astrophysical Journal.* **741**: 68 doi:10.1088/0004-637X/741/2/68

69. Mason, B. (1960). The Origin of Meteorites, *Journal of Geophysical Research*, **65,** 9: 2965–2970

70. Mason, B., (1963). The Carbonaceous Chondrites. *Space Science Reviews*. **1**: 621-646.

71. Meteoritical Bulletin, accessed July 2012:

    http://www.lpi.usra.edu/meteor/metbull.php

72. McSween, H. Y., 1979. Ore carbonaceous chondrites primitive or processed? A review. *Rev. Geophys. Space Phys*., **17:** 1059-1077.

73. McSween, H.Y. 1999. Meteorites and their parent planets. Cambridge University Press, United Kingdom. 2nd edn. 324 pp.

74. Michel, P. and Morbidelli, A. (2007). Review of the population of impactors and the impact cratering rate in the inner solar system. *Meteoritics & Planetary Science*, **42**, 11: 1861-1869.

75. Michikami, T., Nakamura, A.M., Hirata, N., Gaskell, R.W., Nakamura, R., Honda, T., Honda, C., Hiraoka, K., Saito, J., Demura, H., Ishiguro, M., Miyamoto, H., 2008. Size-frequency statistics of boulders on global surface of Asteroid 25143 Itokawa. *Earth Planet. Space* **60:** 13–20.

76. Michikami, T., Nakamura, A., Hirata, N. 2010. The shape distribution of boulders on Asteroid 25143 Itokawa: Comparison with fragments from impact experiments. *Icarus* **207**, 277.

77. Milley E. P. 2010. Physical Properties of Fireball-Producing Earth-Impacting Meteoroids and Orbit Determination through Shadow Calibration of the Buzzard Coulee Meteorite Fall. M.Sc. Thesis. University of Calgary, Canada, 167 p.

78. Miyamoto, H., H. Yano, D. J. Scheeres, S. Abe, O. Barnouin-Jha, A. F. Cheng, H. Demura, R. W. Gaskell, N. Hirata, M. Ishiguro, T. Michikami, A. M. Nakamura, R. Nakamura, J. Saito, and S. Sasaki, Regolith Migration and Sorting on Asteroid Itokawa, *Science*, **316**, 1011–1014, 2007.

79. Nakamura T, Noguchi T, Tanaka M, Zolensky ME, Kimura M, Tsuchiyama A, Nakato A, Ogami T, Ishida H, Uesugi M, Yada T, Shirai K, Fujimura A, Okazaki R, Sandford SA, Ishibashi Y, Abe M, Okada T, Ueno M, Mukai T, Yoshikawa M, Kawaguchi J. 2011. Itokawa dust particles: A direct link between S-type asteroids and ordinary chondrites. Science 333, 1113–1116.

80. Nakamura, A. M., Michikami, T., Hirata, N., Fujiwara, A., Nakamura, R., Ishiguro, M., Miyamoto, H., Demura, H., Hiraoka, K., Honda, T., Honda, C., Saito, J., Hashimoto, T., Kubota, T. 2008. Impact process of boulders on the surface of asteroid 25143 Itokawa—fragments from collisional disruption. *Earth, Planets and Space*, **60**, p. 7-12.

81. Nakamura, E., Makishima, A., Moriguti, T., Kobayashi, K., Tanaka, R., Kunihiro, T., Tsujimori, T., Sakaguchi, C., Kitagawa, H., Ota, T., Yachi, Y., Yada, T., Abe, M., Fujimura, A., Ueno, M., Mukai, T., Yoshikawa, M., Kawaguchi, J. 2012. Space Environment of an Asteroid Preserved on Micro-Grains Returned by the Hayabusa Spacecraft. *43rd Lunar and Planetary Science Conference*, LPI Contribution No. 1659, id.1375.

82. Nesvorný, D., Jedicke, R., Whiteley, R.J., and Ivezic, Z. 2005. Evidence for asteroid space weathering from the Sloan Digital Sky Survey. *Icarus* **173**: 132-152.

83. Neuendorf, K. K.E., Mehl, Jr., J. P. And Jackson, J. A. eds. 2005. Glossary of Geology. 5th edition. Alexandria, Virginia, American Geological Institute. 779 pp. ISBN 0-922152-76-4.

84. Noguchi, T., Nakamura, T., Kimura, M., Zolensky, M. E., Tanaka, M., Hashimoto, T, Konno, M., Nakato, A., Ogami, T., Fujimura, A., Abe, M., Yada, T., Mukai, T., Ueno, M.,Okada, T., Shirai, K., Ishibashi, Y., Okazaki, R. 2010). Incipient Space Weathering Observed on the Surface of Itokawa Dust Particles. *Science* **333**: 1121-1125.

85. O'Brien, D.P. 2004. The Collisional and Dynamical Evolution of the Main-Belt, NEA, and TNO Populations, PhD Dissertation, University of Arizona.

86. O'Brien, D. P. and Greenberg, R. 2003. Steady-State Size Distributions for Collisional Populations: Analytical Solution with Size-Dependent Strength. *Icarus* 164, pp. 334-345.

87. Parker, A., Ivezić, Ž., Jurić, M., Lupton, R., Sekora, M. D., & Kowalski, A. 2008. The size distributions of asteroid families in the SDSS Moving Object Catalog 4. *Icarus*, **198:** 138 - 155

88. Pieters, C.M. and McFadden, L. A. (1994) Meteorite and Asteroid Reflectance Spectroscopy: Clues to Early Solar System Processes, Ann. Rev. *Earth Planet. Sci.*, **22:** 457-497

89. Petrovic, J. J. 2001. Review, Mechanical properties of meteorites and their constituents. *Journal of Materials Science*, **36**: 1579-1583.

90. Rabinowitz, D., Helin, E., Lawrence, K., and Pravdo, S. 2000. A reduced estimate of the number of kilometre-sized near-earth asteroids. *Nature* **403**, 165–166.

91. Rivkin, A. S., Howell, E. S., Vilas, F., and Lebofsky, L. A. 2006. Hydrated minerals on Asteroids: The Astronomical Record. In D. S. Lauretta, & H. Y. McSween (Eds.), *Meteorites and the Early Solar System II* (pp. 19-52). Tucson: University of Arizona Press

92. Rubin, A. E. 2011. Origin of the differences in refractory-lithophile-element abundances among chondrite groups. *Icarus*, **213**: 547 – 558.

93. Saito, J., Miyamoto, H., Nakamura, R., Ishiguro, M., Michikami, T., Nakamura, A. M., Demura, H., Sasaki, S., Hirata, N., Honda, C.,. Yamamoto, A, Yokota, Y., Fuse, T., Yoshida, F., Tholen, D.J., Gaskell, R. W., Hashimoto, T., Kubota, T., Higuchi, Y., Nakamura, T., Smith, P., Hiraoka, K., Honda, T., Kobayashi, S., Furuya, M., Matsumoto, N., Nemoto, E., Yukishita, A., Kitazato, K., Dermawan, B., Sogame, A., Terazono, J., Shinohara, C., & Akiyama H. 2006. Detailed Images of Asteroid 25143 Itokawa from Hayabusa, *Science*, **312,** 1341

94. Scott, E. R. D., Kiel, K., and Stoffler, D. 1992. Shock metamorphism of carbonaceous chondrites. *Geochimica et Cosmochimica Acta*, **56** (12): 4281-4293.

95. Stuart, J.S., Binzel, R.P., 2004. Bias-corrected population, size distribution, and impact hazard for the near-Earth objects. *Icarus* **170**, 295–311.

96. Stuart, J. S. (2001). A Near-Earth Asteroid Population Estimate from the LINEAR Survey. *Science* 294, 1691–1693.

97. Taylor, S., Alexander, C.M.O.'D., Delaney, J., Ma, P., Herzog, G. F., Engrand, C. 2004. Isotopic fractionation of iron, potassium, and oxygen in stony cosmic spherules: Implications for heating histories and sources. Geochimica et Cosmochimica Acta, **69**: 2647 – 2662.

98. Thomas P. (1979) Surface Features of Phobos and Deimos. *Icarus* **40**, 223-243.

99. Thomas, P.C., Veverka, J., Sullivan, R., Simonelli, D.P., Malin, M.C., Caplinger, M., Hartmann, W.K., James, P.B., 2000. Phobos: regolith and ejecta blocks investigated with Mars Orbiter Camera images. *J. Geophys. Res*. **105**, 15091–15106.

100. Thomas, P.C, Veverka, J., Robinson, M.S., Murchie, S. 2001. Shoemaker crater as the source of most ejecta blocks on the asteroid 433 Eros. *Nature*. **413**

101. Urey, H. C. 1961. Criticism of Dr. B. Mason's Paper on 'The Origin of Meteorites', *J. Geophys. Res*., **66**: 6: 1988–1991

102. Veverka, J., Farquhar, B., Robinson, M., Thomas, P., Murchie, S.,Harch, A., Antreasian, P. G., Chesley, S. R., Miller, J. K., Owen, W. M. Jr., Williams, B. G., Yeomans, D., Dunham, D., Heyler, G., Holdridge, M., Nelson, R. L., Whittenburg, K. E., Ray, J. C., Carcich, B., Cheng, A., Chapman, C., Bell, J. F. III, Bell, M., Bussey, B., Clark, B., Domingue, D., Gaffey, M. J., Hawkins, E., Izenberg, N., Joseph, J., Kirk, R., Lucey, P., Malin, M., McFadden, L., Merline, W. J., Peterson, C., Prockter, L., Warren, J., and Wellnitz, D. (2001b) The landing of the NEAR-Shoemaker spacecraft on asteroid 433 Eros. *Nature,* **413***,* 390–393.

103. Weisberg M. K., Prinz M., Clayton R. N., and Mayeda T. K. (1997a) CV3 chondrites; three subgroups, not two (abstract). *Meteoritics & Planetary Science*, **32**, 138–139.

104. Weisberg, M. K., McCoy, T. J., & Krot, A. N. 2006. Systematics and Evaluation of Meteorite Classification. In D. S. Lauretta, & H. Y. McSween (Eds.), *Meteorites and the Early Solar System II* (pp. 19-52). Tucson: University of Arizona Press.

105. Weissman, P.R., Bottke, Jr., W. F., and Levison, H. F. 2002. Evolution of comets into asteroids. In W. Bottke, A. Cellino, P. Paolicchi, & R. Binzel (Eds.), *Asteroids III* (pp. 669-686). Tucson: University of Arizona Press.

106. Wetherill, G. W. (1985). Asteroidal source of ordinary chondrites (Meteoritical Society Presidential Address 1984). *Meteoritics* **20**, 1–22.

107. Wilkison, S. L. and Robinson, M. S. 2000. Bulk density of ordinary chondrite meteorites and implications for asteroidal internal structure. *Meteoritics and Planetary Science*, **35**: 1203-1213.

108. Williams, D. R. and Wetherill, G. W. 1994. Size distribution of collisionally evolved asteroidal populations - Analytical solution for self-similar collision cascades. *Icarus* 107, 117–128.

109. Yomogida, K., and T. Matsui, 1981a. Porosity of ordinary chondrite-Is it a good measure of a consolidation state of composite materials of chondrite? (Abstract), Lunar Planet. Sci., **12**, 1227-1229.

110. Yomogida, K., and T. Matsui, 1981b. Physical properties of some Antarctic meteorites, *Memoirs of the National Institute of Polar Research*, Special Issue, **20**, 384-394,

111. Yomogida, K., and T. Matsui, 1982. Physical properties of some unequilibrated Ant-arctic ordinary chondrites, *Memoirs of the National Institute of Polar Research*, Special Issue, **25**, 308-318.

112. Yomogida, K. and Matsui, T. 1983. Physical properties of ordinary chondrites, Journal of Geophysical Research, **88**: 9513-9533.

113. Yoshida, F., Nakamura, T., Watanabe, J., Kinoshita, D., Yamamoto, N., and Fuse, T. 2003. Size and Spatial Distributions of Sub-km Main-Belt Asteroids. *Publications of the Astronomical Society of Japan* **55**, 701–715.

114. Yoshida, F. 2012. Size Distribution of Asteroids. *Asteroids, Comets, and Meteors 2012*. Abstract # 6063.

115. Zappalá, V., P. Bendjoya, A. Cellino, P. Farinella, and C. Froeschle (1995). Asteroid families: Search of a 12,487-asteroid sample using two different clustering techniques. *Icarus* **116**, 291–314.

APPENDIX A: SIZE-FREQUENCY DISTRIBUTION DATA

Tagish Lake meteorites

ID	Sample Name	Mass (gm)	a	b	c	Dimension (mm)
1	MM-50-i-1	5.807	23.42	22.55	13.16	19.71
2	MM-50-i-2	2.117	17.01	15.54	14.8	15.78
3	MM-50-a-1	17.215	32.24	28.19	23.55	27.99
4	MM-50-a-2	1.166	10.61	9.45	*********	10.03
5			12.84	10.88	*********	11.86
6			7.58	7.31	*********	7.445
7	HG-25 a	6.581	22.13	20.46	19.36	20.65
8	HG-10 a	5.314	22.18	17.67	16.25	18.7
9	HG-10 b	3.238	19.11	15.63	14.12	16.29
10	ET-05 (22-04) a	0.862	12.44	8.33	8.28	9.683
11	ET-05 (22-04) b1	0.665	12.78	9.36	6.45	9.53
12	ET-05 (22-04) b2		3.61	2.54	2.26	2.803
13	MG-25 a	0.523	12.62	11.61	4.39	9.54
14	MG-25 b	0.613	13.84	9.91	4.61	9.453
15	MG-25 c1 I	0.766	14.81	6.15	3.83	8.263
16	MG-25 c1 II		8.86	4.54	2.74	5.38
17	MG-25 c2		10.75	9.8	3.09	7.88
18	MG-25 d1	0.644	9.99	8.79	3.02	7.267
19	MG-25 d2		10.57	6.98	6.46	8.003
20	MG-25 i	2.353	21.08	15.09	9.8	15.32
21	RC-25 a	2.423	17.21	14.19	10.05	13.82
22	RC-25 b	2.353	15.02	14.17	12.58	13.92
23	RC-25 c	2.331	19.88	12.81	10.08	14.26
24	HG-14 a 1	5.939	26.02	19	15.5	20.17
25	HG-14 a 2	0.689	10.24	8.98	5.62	8.28
26			7.31	6.41	5	6.24

ID	Sample Name	Mass (gm)	a	b	c	Dimension (mm)
27			8.27	4.91	2.81	5.33
28			5.65	5.45	2.54	4.547
29	HG-14 b	2.791	20.58	15.78	8.53	14.96
30	HG-14 d	1.891	14.02	13.47		13.75
31	MG - 36 a	2.856	15.2	13.05	12.09	13.45
32	HG-20 a	7.405	34.97	21.32		28.15
33	HG-20 c 1	1.333	14.18	11.52	5.76	10.49
34	HG-20 c 2		12.3	7.38	4.73	8.137
35	HG-20 c 3		11.43	9.56	2.99	7.993
36	HG-08 a 1	1.166	11.95	8.69	5.98	8.873
37	HG-08 a 2		11.3	8.37	3.93	7.867
38	HG-08 a 3		9.35	7.51	5.89	7.583
39	HG-08 b 1	0.627	10.84	7.59	3.49	7.307
40	HG-08 b 2		12.35	5.99	2.79	7.043
41	HG-08 b 3		8.17	3.53	3.25	4.983
42	HG-08 b 4		7.65	3.89	3.67	5.07
43	HG-09 a	1.153	15.13	11	7.15	11.09
44	HG-09 b	0.943	14.92	9.37	8.37	10.89
45	HG-09 c	0.444	10.44	8.25	6.4	8.363
46	HG-09 d 1	0.597	11.26	10.71	10.44	10.8
47	HG-09 d 2		10.28	8.12	2.42	6.94
48	HG-09 d 3		6.77	6.41	2.04	5.073
49	MG-66 a	3.095	19.67	15.39	10.55	15.2
50	MM-79 a	0.848	16.55	12.8	5.47	11.61
51	MM-79 b 1	1.953	17.1	12.17	5.72	11.66
52	MM-79 b 2		17.23	11.91	5.22	11.45
53	MM-65 c	1.421	15.44	11.76	10.98	12.73
54	MM-65 d 1	1.58	10.59	6.5	2.19	6.427
55	MM-65 d 2		9.24	8.23	4.04	7.17
56	MM-65 d 3		10.4	7.79	7.35	8.513

ID	Sample Name	Mass (gm)	a	b	c	Dimension (mm)
57	MM-65 d 4		7.76	6.81	6.04	6.87
58	MM-65 d 5		7.94	6.95	6.29	7.06
59	MM-65 d 6		6.16	5.38	5	5.513
60	MM-01(25-01) a 1	0.475	8.33	8.14	3.76	6.743
61	MM-01(25-01) a 2		8.1	7.85	3.49	6.48
62	MM-01(25-01) a 3		10.5	6.49	1.97	6.32
63	MM-01 a	5.235	20.9	19.22	15.03	18.38
64	MM-01 c	1.975	19.14	14.97	9.24	14.45
65	MM-01 d 1	1.935	12.18	6.69	6.57	8.48
66	MM-01 d 2		8.73	8.61	5.94	7.76
67	MM-01 d 3		14.7	8.57	6.87	10.05
68	EG-06 a	1.454	16.46	11.83	11.66	13.32
69	EG-06 b	3.093	18.03	16.42	11.3	15.25
70	EG-06 i	1.239	19.73	9.75	8.72	12.73
71	EG-06 j	0.688	14.97	9.14	8.01	10.71
72	HG-71 a	5.045	22.5	19.76	15.19	19.15
73	HG-71 c	0.909	13.24	12.54	8.46	11.41
74	HG-71 d	0.743	17.18	7.88	5.08	10.05
75	HG-70 e	0.994	16.09	9.27	6.66	10.67
76	HG-70 f	0.913	12.08	11.92	6.84	10.28
77	HG-70 g	0.821	13.35	11.19	7.57	10.7
78	HG-70 h	0.685	11.83	11.52	10.18	11.18
79	HG-16 a	2.153	16.87	14.62	13.01	14.83
80	HG-13 a	1.629	15.82	12.57	11.4	13.26
81	HG-13 b	1.3	17.15	8.37	7.56	11.03
82	HG-13 c 1	1.163	15.89	10.13	5.77	10.6
83	HG-13 c 2		8.51	8.15	7.78	8.147
84	HG-13 e	1.449	16.23	10.77	8.82	11.94
85	HG-13 h	1.139	13	10.16	9.63	10.93
86	HG-13 j 1		15.71	7.83	7.42	10.32

ID	Sample Name	Mass (gm)	a	b	c	Dimension (mm)
87	HG-13 j 2	1.261	14.41	6.91	3.95	8.423
88	HG-13 k	0.791	11.96	9.5	6.62	9.36
89	HG-19 d 1	0.335	9.85	6.2	3.36	6.47
90	HG-19 d 2		9.02	7.06	3.98	6.687
91	MM-10 a	0.414	12.12	6.19	5.96	8.09
92	PM-09 b	0.747	16.13	11.37	6	11.17
93	PM-09 c 1	1.199	9.2	5.26	4.6	6.353
94	PM-09 c 2		10.04	6.44	5.19	7.223
95	PM-09 c 3		12.15	7.21	4.14	7.833
96	PM-09 c 4		9.76	6.74	3.91	6.803
97	PM-09 c 5		9	5.23	4.45	6.227
98	PM-09 c 6		5.86	5.63	3.05	4.847
99	PM-09 c 7		4.29	3.64	1.57	3.167
100	MC-03 a	0.792	16.19	7.73	7.61	10.51
101	MC-03 b 1	1.127	11.18	8.02	6.04	8.413
102	MC-03 b 2		11.3	8.28	5.39	8.323
103	MC-03 b 3		5.22	4.34	2.43	3.997
104	MC-03 c 1	2.761	8.52	6.85	3.95	6.44
105	MC-03 c 2		7.69	7.33	2.97	5.997
106	MC-03 c 3		7.31	6.79	3.75	5.95
107	MC-03 c 4		13.78	11.34	4.44	9.853
108	MC-03 c 5		5.47	4.94	4.85	5.087
109	MC-03 c 6		8.74	6.96	2.55	6.083
110	MC-03 c 7		14.06	4.87	4.28	7.737
111	MC-03 c 8		8.59	6.91	3.92	6.473
112	MC-03 c 9		7.53	7.21	3.17	5.97
113	MC-03 c 10		8.14	6.71	3.02	5.957
114	MC-03 c 11		8.77	7.97	3.92	6.887
115	HP-23 a	14.258	30.28	23.5	22.51	25.43
116	HP-23 c 1	1.254	13.26	11.79	4.31	9.787

ID	Sample Name	Mass (gm)	a	b	c	Dimension (mm)
117	HP-23 c 2		11.65	9.94	3.84	8.477
118	HP-11 a	8.243	22.31	19.58	18.74	20.21
119	HP-11 b	5.985	27.38	17.89	13.89	19.72
120	RC-07 (30-28) b	11.085	27.11	23.77	17.17	22.68
121	RC-07 (30-28) c	9.676	17.41	11.57	5.44	11.47
122	Unknown fragment	14.839	28.55	26.44	25.74	26.91
123	MM-83 a	12.455	31.41	25.2	18.66	25.09
124	MM-83 a (platy frag)		25.73	23.21	*********	24.47
125	MM-83 c	0.146	13.66	5.09	3.21	7.32
126	MM-82 b	2.265	22.5	15.4	7.83	15.24
127	MM-86 a	1.915	14.54	14.11	13.92	14.19
128	MM-86 b 1	1.521	14.15	9.9	7.34	10.46
129	MM-86 b 2		10.9	9.57	7.09	9.187
130	MM-86 c	0.114	7.02	4.7	3.6	5.107
131	MM-86 h	0.084	5.27	4.98	4.08	4.777
132	MM-86 i	0.177	6.54	3.87	3.22	4.543
133	MM-86 g	0.08	7.44	6.72	4.46	6.207
134	HG-67 a 1	1.079	18.56	9.09	5.42	11.02
135	HG-67 a 2		8.58	6.67	2.2	5.817
136	HG-67 a 3		6.46	5.72	5.43	5.87
137	HG-67 c	0.168	10.17	6.72	2.97	6.62
138	HG-67 d 1	0.489	8	6.73	6.18	6.97
139	HG-67 d 2		8.77	5.33	4.78	6.293
140	HG-67 e 1	0.208	8.38	4.16	2.07	4.87
141	HG-67 e 2		8.25	6.81	3.52	6.193
142	ET-03 c	1.169	16.35	9.48	8.2	11.34
143	ET-03 d	0.713	11.35	8.56	6.05	8.653
144	ET-03 e	0.704	14.18	11.41	6.6	10.73
145	ET-03 f 1	1.281	8.04	7.43	6.68	7.383
146	ET-03 f 2		14.44	10.13	5	9.857

ID	Sample Name	Mass (gm)	a	b	c	Dimension (mm)
147	ET-03 f 3		8.9	7.61	5.4	7.303
148	ET-03 f 4		8.14	7.07	5.41	6.873
149	ET-03 h 1	1.32	9.49	6.56	6	7.35
150	ET-03 h 2		9.63	6.1	3.8	6.51
151	ET-03 h 3		7.1	6.62	4.68	6.133
152	ET-03 h 4		6.56	6.29	4.92	5.923
153	ET-03 h 5		9.86	7.24	2.84	6.647
154	ET-03 h 6		7.17	5.11	4.32	5.533
155	ET-03 h 7		7.37	5.96	4.43	5.92
156	ET-03 h 8		7.22	4.43	3.33	4.993
157	ET-03 h 9		4.21	4.04	2.89	3.713
158	ET-03 h 10		4.68	3.41	2.86	3.65
159	ET-03 m 1	0.63	10.08	6.28	5.37	7.243
160	ET-03 m 2		10.3	6.17	5.97	7.48
161	RC-04 a	1.442	16.69	11.29	8.63	12.2
162	RC-04 b	0.663	11.96	8.06	7.94	9.32
163	HG-22 a 1	1.316	15.46	11.53	5.92	10.97
164	HG-22 a 2		9.54	7.77	3.01	6.773
165	HG-22 a 3		6.72	5.14	3.7	5.187
166	HG-22 b	0.514	10.61	9.6	4.68	8.297
167	HG-57 b	1.231	12.16	8.42	5.78	8.787
168	HG-57 c	0.366	10.22	6.83	4.75	7.267
169	MM-88 a	7.609	24.77	22.9	18.78	22.15
170	HP-25 a	1.066	15.56	12.39	6.44	11.46
171	HP-23 a	0.817	14.49	11.33	*********	12.91
172	HP-20 a	8.817	25.21	21.04	18.6	21.62
173	HP-20 b	6.978	22.4	17.04	14.88	18.11
174	HP-20 c	2.374	19.98	15.87	13.26	16.37
175	HP-20 e	0.914	13.65	8.63	7.87	10.05
176	HP-20 f	0.683	13.9	7.73	7.04	9.557

ID	Sample Name	Mass (gm)	a	b	c	Dimension (mm)
177	HP-20 g 1	0.75	16.2	8.53	5.55	10.09
178	HP-20 g 2		6.14	6.4	4.54	5.693
179	HP-20 h 1	0.878	13.13	10.45	3.47	9.017
180	HP-20 h 2		15.94	8.43	3.69	9.353
181	HP-01 b	3.578	20.36	16.86	14.61	17.28
182	HP-01 c	2.191	21.16	15.06	10.71	15.64
183	HP-01 d 1	0.401	10.26	6.62	5.16	7.347
184	HP-01 d 2		9.52	5.61	5	6.71
185	RC-08 a	1.777	14.18	12.2	10.01	12.13
186	RC-08 b	1.589	16.9	8.91	8.31	11.37
187	MG-58 a	1.799	13.15	13.06	10.9	12.37
188	MM-21 a	3.528	15.7	15.35	12.1	14.38
189	MM-21 b	1.683	17.05	13.32	10.31	13.56
190	MM-21 c	0.91	13.99	9.4	8.84	10.74
191	MM-26 a		16.17	9.69	7.62	11.16
192	MM-26 b		11.15	8.84	6.61	8.867
193	EG-36 b		13.2	9.48	4.73	9.137
194	HG-24 a		17.2	14.01	7.58	12.93
195	PM-09 a		33.84	32.5	23.7	30.01
196	MG-65 a		34.84	33.37	16.18	28.13

Asteroid 25134 Itokawa

Komaba Crater

ID	Long (px)	Short (px)	Long (cm)	Short (cm)	Mean (cm)
1	14.813	9.523	148.13	95.23	121.68
2	5.063	3.629	50.63	36.29	43.46
3	3.391	2.132	33.91	21.32	27.615
4	9.066	7.944	90.66	79.44	85.05
5	9.704	5.591	97.04	55.91	76.475
6	3.084	2.43	30.84	24.3	27.57
7	7.255	5.8	72.55	58	65.275
8	5.572	5.328	55.72	53.28	54.5
9	8.562	5.618	85.62	56.18	70.9
10	4.111	2.012	41.11	20.12	30.615
11	4.175	3.133	41.75	31.33	36.54
12	2.859	2.843	28.59	28.43	28.51
13	4.954	4.296	49.54	42.96	46.25
14	3.24	2.056	32.4	20.56	26.48
15	3.195	2.05	31.95	20.5	26.225
16	3.625	2.285	36.25	22.85	29.55
17	9.028	6.621	90.28	66.21	78.245
18	4.378	2.861	43.78	28.61	36.195
19	3.197	2.425	31.97	24.25	28.11
20	7.205	6.094	72.05	60.94	66.495
21	12.473	10.665	124.73	106.65	115.69
22	3.49	2.7	34.9	27	30.95
23	3.192	3.086	31.92	30.86	31.39
24	6.416	4.222	64.16	42.22	53.19
25	7.864	4.264	78.64	42.64	60.64
26	4.148	3.163	41.48	31.63	36.555
27	4.08	4.132	40.8	41.32	41.06
28	3.933	2.46	39.33	24.6	31.965
29	4.04	2.228	40.4	22.28	31.34
30	4.204	2.855	42.04	28.55	35.295
31	3.028	2.355	30.28	23.55	26.915

ID	Long (px)	Short (px)	Long (cm)	Short (cm)	Mean (cm)
32	3.917	2.209	39.17	22.09	30.63
33	2.853	2.216	28.53	22.16	25.345
34	4.038	2.056	40.38	20.56	30.47
35	2.55	1.8	25.5	18	21.75
36	4.68	3.06	46.8	30.6	38.7
37	5.007	2.834	50.07	28.34	39.205
38	2.961	1.884	29.61	18.84	24.225
39	3.101	2.131	31.01	21.31	26.16
40	4.752	1.626	47.52	16.26	31.89
41	2.019	1.884	20.19	18.84	19.515
42	2.773	2.153	27.73	21.53	24.63
43	2.993	2.019	29.93	20.19	25.06
44	2.025	2.018	20.25	20.18	20.215
45	3.584	1.62	35.84	16.2	26.02
46	3.151	1.702	31.51	17.02	24.265
47	2.311	2.21	23.11	22.1	22.605
48	2.23	2.16	22.3	21.6	21.95
49	2.813	2.083	28.13	20.83	24.48
50	3.24	2.7	32.4	27	29.7
51	3.903	2.5	39.03	25	32.015
52	2.261	1.869	22.61	18.69	20.65
53	4.019	2.05	40.19	20.5	30.345
54	3.543	1.793	35.43	17.93	26.68
55	2.809	2.809	28.09	28.09	28.09
56	2.975	2.055	29.75	20.55	25.15
57	2.792	1.416	27.92	14.16	21.04
58	1.453	1.377	14.53	13.77	14.15
59	2.863	2.753	28.63	27.53	28.08
60	3.038	2.315	30.38	23.15	26.765
61	4.148	3.163	41.48	31.63	36.555
62	2.991	1.869	29.91	18.69	24.3
63	2.025	2.012	20.25	20.12	20.185
64	2.028	2.025	20.28	20.25	20.265
65	3.654	2.883	36.54	28.83	32.685

ID	Long (px)	Short (px)	Long (cm)	Short (cm)	Mean (cm)
66	3.51	2.295	35.1	22.95	29.025
67	3.029	2.002	30.29	20.02	25.155
68	3.585	2.842	35.85	28.42	32.135
69	4.296	2.316	42.96	23.16	33.06
70	7.259	3.586	72.59	35.86	54.225
71	4.1	1.568	41	15.68	28.34
72	3.601	2.351	36.01	23.51	29.76
73	3.638	2.953	36.38	29.53	32.955
74	2.991	1.963	29.91	19.63	24.77
75	3.577	2.644	35.77	26.44	31.105
76	3.014	2.216	30.14	22.16	26.15
77	4.23	2.599	42.3	25.99	34.145
78	4.035	2.018	40.35	20.18	30.265
79	3.051	1.947	30.51	19.47	24.99
80	2.9	2.868	29	28.68	28.84
81	3.575	3.575	35.75	35.75	35.75
82	1.983	1.928	19.83	19.28	19.555
83	3.064	2.277	30.64	22.77	26.705
84	3.586	3.586	35.86	35.86	35.86
85	3.038	1.947	30.38	19.47	24.925

Rough Terrane I

ID	Long (px)	Short (px)	long (cm)	short (cm)	Mean (cm)
1	6.515	3.763	65.15	37.63	51.39
2	21.534	14.774	215.34	147.74	181.54
3	32.974	27.03	329.74	270.3	300.02
4	13.256	8.138	132.56	81.38	106.97
5	18.314	10.36	183.14	103.6	143.37
6	27.274	15.641	272.74	156.41	214.575
7	10.763	3.484	107.63	34.84	71.235
8	9.801	6.101	98.01	61.01	79.51
9	4.998	2.038	49.98	20.38	35.18

ID	Long (px)	Short (px)	long (cm)	short (cm)	Mean (cm)
10	9.412	7.427	94.12	74.27	84.195
11	13.117	11.963	131.17	119.63	125.4
12	12.992	6.916	129.92	69.16	99.54
13	50.776	30.355	507.76	303.55	405.655
14	16.287	10.221	162.87	102.21	132.54
15	43.51	21.827	435.1	218.27	326.685
16	16.94	8.015	169.4	80.15	124.775
17	11.156	7.027	111.56	70.27	90.915
18	19.074	12.999	190.74	129.99	160.365
19	14.917	13.01	149.17	130.1	139.635
20	30.459	19.839	304.59	198.39	251.49
21	31.404	25.498	314.04	254.98	284.51
22	3.263	3.032	32.63	30.32	31.475
23	8.764	7.257	87.64	72.57	80.105
24	19.732	17.997	197.32	179.97	188.645
25	3.672	3.672	36.72	36.72	36.72
26	17.116	10.59	171.16	105.9	138.53
27	20.954	14.209	209.54	142.09	175.815
28	8.429	2.228	84.29	22.28	53.285
29	8.561	2.125	85.61	21.25	53.43
30	10.901	8.327	109.01	83.27	96.14
31	10.673	7.303	106.73	73.03	89.88
32	4.062	4.062	40.62	40.62	40.62
33	6.105	4.839	61.05	48.39	54.72
34	7.031	5.031	70.31	50.31	60.31
35	14.148	9.108	141.48	91.08	116.28
36	9.821	5.71	98.21	57.1	77.655
37	5.007	1.938	50.07	19.38	34.725
38	5.195	2.762	51.95	27.62	39.785
39	10.754	8.466	107.54	84.66	96.1
40	3.876	2.018	38.76	20.18	29.47
41	4.07	3.1	40.7	31	35.85
42	3.015	2.811	30.15	28.11	29.13
43	5.023	5.023	50.23	50.23	50.23

ID	Long (px)	Short (px)	long (cm)	short (cm)	Mean (cm)
44	4.284	2.762	42.84	27.62	35.23
45	6.047	6.046	60.47	60.46	60.465
46	13.954	4.884	139.54	48.84	94.19
47	4.115	2.8	41.15	28	34.575
47	3.657	4.687	36.57	46.87	41.72
48	5.756	3.05	57.56	30.5	44.03

Rough Terrane II

ID	Long (px)	Short (px)	Long (cm)	Short (cm)	Mean (cm)
1	33.197	18.276	331.97	182.76	257.365
2	18.699	18.412	186.99	184.12	185.555
3	21.396	19.303	213.96	193.03	203.495
4	17.361	16.313	173.61	163.13	168.37
5	6.601	3.635	66.01	36.35	51.18
6	18.14	14.001	181.4	140.01	160.705
7	4.154	3.213	41.54	32.13	36.835
8	18.762	13.801	187.62	138.01	162.815
9	27.297	8	272.97	80	176.485
10	19.075	13.03	190.75	130.3	160.525
11	38.729	22.731	387.29	227.31	307.3
12	4.07	3.101	40.7	31.01	35.855
13	9.514	4.462	95.14	44.62	69.88
14	7.234	6.269	72.34	62.69	67.515
15	12.483	7.549	124.83	75.49	100.16
16	9.626	8.972	96.26	89.72	92.99
17	4.689	4.354	46.89	43.54	45.215
18	3.05	3.014	30.5	30.14	30.32
19	6.698	8.651	66.98	86.51	76.745
20	5.224	4.441	52.24	44.41	48.325
21	20.159	16.039	201.59	160.39	180.99
22	14.02	10.982	140.2	109.82	125.01

ID	Long (px)	Short (px)	Long (cm)	Short (cm)	Mean (cm)
23	9.046	4.114	90.46	41.14	65.8
24	17.168	10.003	171.68	100.03	135.855
25	4.972	3.102	49.72	31.02	40.37
26	9.309	6.659	93.09	66.59	79.84
27	12.107	4.431	121.07	44.31	82.69
28	5.942	2.914	59.42	29.14	44.28
29	5.581	3.954	55.81	39.54	47.675
30	7.104	5.121	71.04	51.21	61.125
31	8.838	7.674	88.38	76.74	82.56
32	13.501	7.9	135.01	79	107.005
33	15.889	13.503	158.89	135.03	146.96
34	8.078	3.622	80.78	36.22	58.5
35	8.137	6.572	81.37	65.72	73.545
36	8.597	5.031	85.97	50.31	68.14
37	9.731	6.858	97.31	68.58	82.945
38	4.25	4.111	42.5	41.11	41.805
39	13.13	12.459	131.3	124.59	127.945
40	8.561	3.718	85.61	37.18	61.395
41	7.997	5.031	79.97	50.31	65.14
42	6.225	3.55	62.25	35.5	48.875
43	6.99	4.111	69.9	41.11	55.505
44	7.212	3.853	72.12	38.53	55.325
45	6.432	6.071	64.32	60.71	62.515
46	11.625	5.703	116.25	57.03	86.64
47	6.334	2.099	63.34	20.99	42.165
48	6.477	3.015	64.77	30.15	47.46
49	7.985	7.442	79.85	74.42	77.135
50	9.815	8.652	98.15	86.52	92.335
51	7.354	7.225	73.54	72.25	72.895
52	6.105	5.246	61.05	52.46	56.755
53	14.667	8.223	146.67	82.23	114.45

ID	Long (px)	Short (px)	Long (cm)	Short (cm)	Mean (cm)
54	7.921	4.276	79.21	42.76	60.985
55	8.18	7.221	81.8	72.21	77.005
56	14.841	11.375	148.41	113.75	131.08
57	11.985	9.673	119.85	96.73	108.29
58	7.824	6.307	78.24	63.07	70.655
59	2.764	2.191	27.64	21.91	24.775
60	6.24	3.996	62.4	39.96	51.18
61	13.33	4.443	133.3	44.43	88.865
62	9.058	7.243	90.58	72.43	81.505
63	10.636	10.052	106.36	100.52	103.44
64	7.635	5.471	76.35	54.71	65.53
65	5.246	3.015	52.46	30.15	41.305
66	23.11	10.575	231.1	105.75	168.425
67	6.988	5.65	69.88	56.5	63.19

Muses-C Region

ID	Long (px)	Short (px)	Long (cm)	Short (cm)	Mean (cm)
1	3.192	2.257	31.92	22.57	27.245
2	2.264	2.264	22.64	22.64	22.64
3	2.025	1.947	20.25	19.47	19.86
4	5.047	2.991	50.47	29.91	40.19
5	2.149	1.869	21.49	18.69	20.09
6	32.191	14.164	321.91	141.64	231.775
7	3.028	2.019	30.28	20.19	25.235
8	4.058	1.156	40.58	11.56	26.07
9	3.6	2.235	36	22.35	29.175
10	4.038	3.925	40.38	39.25	39.815
11	4.284	2.762	42.84	27.62	35.23
12	2.106	1.524	21.06	15.24	18.15

ID	Long (px)	Short (px)	Long (cm)	Short (cm)	Mean (cm)
13	3.037	1.947	30.37	19.47	24.92
14	13.435	8.978	134.35	89.78	112.065
15	4.015	1.575	40.15	15.75	27.95
16	2.762	2.665	27.62	26.65	27.135
17	2.777	2.696	27.77	26.96	27.365
18	4.204	2.859	42.04	28.59	35.315
19	3.629	2.169	36.29	21.69	28.99
20	4.363	2.301	43.63	23.01	33.32
21	4.296	4.186	42.96	41.86	42.41
22	2.963	2.257	29.63	22.57	26.1
23	2.777	2.696	27.77	26.96	27.365
24	2.959	1.947	29.59	19.47	24.53
25	3.639	3.018	36.39	30.18	33.285
26	2.935	2.935	29.35	29.35	29.35
27	5.117	3.499	51.17	34.99	43.08
28	2.7777	2.702	27.777	27.02	27.3985
29	1.432	1.378	14.32	13.78	14.05
30	2.986	1.947	29.86	19.47	24.665
31	3.084	1.963	30.84	19.63	25.235
32	5.087	4.111	50.87	41.11	45.99
33	22.869	21.125	228.69	211.25	219.97
34	4.283	2.801	42.83	28.01	35.42
35	3.545	2.212	35.45	22.12	28.785
36	6.394	3.639	63.94	36.39	50.165
37	4.227	2.741	42.27	27.41	34.84
38	3.069	1.938	30.69	19.38	25.035
39	2.908	2.843	29.08	28.43	28.755
40	4.804	3.629	48.04	36.29	42.165
41	3.253	2.019	32.53	20.19	26.36
42	2.019	1.907	20.19	19.07	19.63
43	1.947	1.869	19.47	18.69	19.08

ID	Long (px)	Short (px)	Long (cm)	Short (cm)	Mean (cm)
44	4.229	2.71	42.29	27.1	34.695
45	3.68	2.542	36.8	25.42	31.11
46	1.521	1.389	15.21	13.89	14.55

Planetary Data System specification for image st_2532629277_v.fit:

```
PDS_VERSION_ID                      = PDS3

RECORD_TYPE                         = "FIXED_LENGTH"
RECORD_BYTES                        = 2880
FILE_RECORDS                        = 367

^HEADER                             = "st_2532629277_v.fit"
^IMAGE                              = ("st_2532629277_v.fit", 3)

DATA_SET_ID                         = "HAY-A-AMICA-3-HAYAMICA-V1.0"
PRODUCT_NAME                        = "20051109:ST_2532629277_V.FIT"
PRODUCT_ID                          = "20051109_ST_2532629277_V_FIT"
INSTRUMENT_HOST_ID                  = "HAY"
INSTRUMENT_HOST_NAME                = "HAYABUSA"
INSTRUMENT_ID                       = "AMICA"
INSTRUMENT_NAME                     = "ASTEROID MULTI-BAND IMAGING CAMERA"
TARGET_NAME                         = "25143 ITOKAWA"
TARGET_TYPE                         = "ASTEROID"
START_TIME                          = 2005-11-09T05:00:02
STOP_TIME                           = 2005-11-09T05:00:02
PRODUCT_CREATION_TIME               = 2008-04-08  /* File uploaded to OLAF */
FILTER_NAME                         = "V"
EXPOSURE_DURATION                   = .0435 <SECOND>

TARGET_DISTANCE                     = 1.08147 <KILOMETER>
LONGITUDE                           = 88.24613 <DEGREE>
LATITUDE                            = 7.55017 <DEGREE>
CELESTIAL_NORTH_CLOCK_ANGLE         = 201.96662 <DEGREE>
BODY_POLE_CLOCK_ANGLE               = 86.53524 <DEGREE>
HAY:BODY_POLE_ASPECT_ANGLE          = 90.00337 <DEGREE>
SUB_SOLAR_AZIMUTH                   = 82.57162 <DEGREE>
RIGHT_ASCENSION                     = 215.62945 <DEGREE>
DECLINATION                         = -13.85974 <DEGREE>
RA_DEC_REF_PIXEL                    = (512,512)
SUB_SOLAR_LONGITUDE                 = 111.45453 <DEGREE>
SUB_SOLAR_LATITUDE                  = 0.76703 <DEGREE>
INCIDENCE_ANGLE                     = 36.16202 <DEGREE>
EMISSION_ANGLE                      = 30.55462 <DEGREE>
PHASE_ANGLE                         = 8.98281 <DEGREE>
SOLAR_ELONGATION                    = 172.56480 <DEGREE>
SUB_SPACECRAFT_LONGITUDE            = 102.47091 <DEGREE>
SUB_SPACECRAFT_LATITUDE             = 0.77510 <DEGREE>
TARGET_CENTER_DISTANCE              = 1.199351 <KILOMETER>
X_OFFSET                            = -75.9
Y_OFFSET                            = 134.8
HAY:BODY_POLE_SUN_ANGLE             = 172.62936 <DEGREE>
TARGET_HELIOCENTRIC_DISTANCE        = 144747547.07848 <KILOMETER>
SPACECRAFT_SOLAR_DISTANCE           = 144747548.26312 <KILOMETER>

OBJECT                              = HEADER
 BYTES                              = 5760
 HEADER_TYPE                        = "FITS"
```

```
 INTERCHANGE_FORMAT                    = "BINARY"
 RECORDS                               = 2
 DESCRIPTION                           = "FITS Standard NOST 100-2.0"
END_OBJECT                            = HEADER


OBJECT                                = IMAGE
  LINES                               = 1024
  LINE_SAMPLES                        = 1024
  SAMPLE_BITS                         = 8
  SAMPLE_TYPE                         = "MSB_UNSIGNED_INTEGER"
  OFFSET                              = 0.0
  SCALING_FACTOR                      = 1.0
  DERIVED_MINIMUM                     = -128.0
  DERIVED_MAXIMUM                     = 127.0
  AXIS_ORDER_TYPE                     = "FIRST_INDEX_FASTEST"
  LINE_DISPLAY_DIRECTION              = "UP"
  SAMPLE_DISPLAY_DIRECTION            = "RIGHT"
  UNIT                                = "ADU"
  HORIZONTAL_PIXEL_FOV                = 20 <ARCSECOND>
  VERTICAL_PIXEL_FOV                  = 20 <ARCSECOND>
  DESCRIPTION                         = "Hayabusa AMICA image"
END_OBJECT                            = IMAGE

END
```

APPENDIX B: BULK DENSITY AND ELASTIC WAVE VELOCITY DATA

Sample	Label	Type	Petr. Type	Fall time	ρ (gm/cc)	Vp (m/sec)	Vs (m/sec)
Banten	NHM BM 1984.M5	CM	2	1933	2.36	2896.57	1881.59
Banten	USNM 6017	CM	2	1933	2.74	2672.17	1680.98
Bells	USNM 6926	CM	2	1961	2.28	2500.20	1625.64
Boriskino	NHM BM 63624	CM	2	1930	2.41	2943.29	1632.07
Cold Bokkeveld	NHM BM 1727	CM	2	1838	2.23	3461.57	2235.85
Crescent	USNM 6927	CM	2	1936	2.02	1854.23	1293.96
Mighei	NHM BM 65 604	CM	2	1889	1.96	1501.82	950.14
Mighei	USNM 3483	CM	2	1889		1582.28	1008.93
Murchison	NHM BM 1984.M154	CM	2	1969	2.21	2379.59	1564.02
Murray	NHM BM1971.288	CM	2	1969	2.18	2528.52	1439.01
Murray	AMNH 4782	CM	2	1950		2437.52	1286.87
Nawapali	NHM BM 82968	CM	2	1890	2.17	2331.06	1588.49
Nogoya	NHM BM1985.MM154	CM	2	1879	2.29	2296.09	1490.26
Nogoya	USNM 6490	CM	2	1879	1.85	2399.20	1346.06
Pollen	NHM BM 1964.496	CM	2	1942	2.27	1844.05	1225.96
Santa Cruz	NHM BM 1959.782	CM	2	1939	2.06	1549.51	956.69
Renazzo	NHM BM 41105	CR	2	1824	3.00	3020.46	1952.49
Renazzo	AMNH 4905	CR	2	1824	3.15	3867.42	2693.49
Renazzo	USNM 6172	CR	2	1824	3.13	3530.08	1903.92
Al Rais	NHM BM 1971.289	CR	2	1957	2.37	1902.90	1311.45
Al Rais	USNM 1794	CR	2	1957	2.26	2232.67	1327.39
Kainsaz	NHM BM 1999.M63	CO	3.2	1937	2.69	3877.23	2712.84
Kainsaz	AMNH 4717	CO	3.2	1937	2.89	2640.97	1800.64
Kainsaz	USNM 2486	CO	3.2	1937	3.31	2354.44	1432.72
Felix	NHM BM 1971.290	CO	3.3	1900	2.87	2005.15	1296.45
Felix	USNM 235	CO	3.3	1900	2.86	2012.83	1315.51
Ornans	NHM (?)	CO	3.4	1868	2.38	2244.36	1481.47

Sample	Label	Type	Petr. Type	Fall time	ρ (gm/cc)	Vp (m/sec)	Vs (m/sec)
Ornans	USNM M6336	CO	3.4	1868	2.43	1901.72	1261.58
Lancé	NHM BM 1924.14	CO	3.5	1872	3.34	2825.29	1950.78
Lancé	AMNH 5120	CO	3.5	1872	3.41	2661.98	1762.11
Lancé	AMNH 5121	CO	3.5	1872	3.47	2723.40	1758.96
Lancé	USNM 2873	CO	3.5	1872	3.22	4142.31	2388.68
Moss	AMNH 5185	CO	3.6	2006	2.42	2514.93	1353.46
Moss	AMNH 5186	CO	3.6	2006	2.66	2543.75	1608.81
Warrenton	NHM (?)	CO	3.7	1877	2.55	1747.37	1050.49
Allende	NHM (?)	CV	3.0	1969	2.84	2260.34	1461.35
Allende	USNM 3529	CV	3.0	1969		2528.45	1683.31
Bali	USNM 7116	CV	3.0	1907		4202.72	2569.39
Grosnaja	NHM BM 63624	CV	3.0	1861	2.94	4126.70	2667.48
Grosnaja	AMNH 455	CV	3.0	1861	2.87	3428.73	2368.94
Kaba	NHM BM 35794	CV	3.0	1857	2.75	2440.15	1664.67
Mokoia	NHM BM 1910.729	CV	3.0	1908	2.68	1015.91	665.35
Vigarano	AMNH 2226	CV	3.0	1910	3.05	4479.68	2854.56
Vigarano	AMNH 2226	CV	3.0	1910	2.88	3796.28	2624.09
Vigarano	USNM 3137	CV	3.0	1910	3.68	4146.83	2376.60
Karoonda	NHM BM 1973 M25	CK	4.0	1930	2.65	1161.18	817.22
Ningqiang	NHM BM 1999.M66	CK	3.0	1983	3.26	1934.98	1182.21
Ningqiang	AMNH 4816	CK	3.0	1983		2005.99	1377.32

The Elastic Moduli Data

Sample	Type	Petr. Type	Shock	CRE age	Vp/Vs	Shear Modulus	Bulk Modulus	Lame' Parameter	Poisson's Ratio	Young' Modulus
Banten	CM	2			1.56	8.09	8.98	3.59	0.15	18.66
Bells	CM	2	1	0.37	1.54	6.03	6.22	2.20	0.13	13.68
Boriskino	CM	2		0.72	1.80	6.41	12.30	8.03	0.28	16.39
C.Bokkeveld	CM	2	1	0.56	1.55	11.15	11.86	4.43	0.14	25.48
Crescent	CM	2	1		1.43	3.38	2.43	0.18	0.03	6.93
Mighei	CM	2	1	3.49	1.57	1.88	2.15	0.90	0.16	4.37
Murchison	CM	2	2	1.32	1.52	5.40	5.30	1.70	0.12	12.09
Murray	CM	2	1	4.69	1.82	4.06	8.06	5.35	0.28	10.42
Nawapali	CM	2		0.71	1.47	5.49	4.50	0.84	0.07	11.71
Nogoya	CM	2	1	0.19	1.66	4.17	5.87	3.09	0.21	10.11
Pollen	CM	2	1	1.71	1.50	3.41	3.17	0.89	0.10	7.52
Santa Cruz	CM	2	1	6.78	1.62	1.88	2.43	1.17	0.19	4.49
Renazzo	CR	2	2	5.10	1.59	14.77	17.67	7.82	0.17	34.64
Al Rais	CR	2	1	11.80	1.57	4.04	4.53	1.84	0.16	9.34
Kainsaz	CO	3	1	20.80	1.49	11.64	10.40	2.64	0.09	25.43
Felix	CO	3	3	51.40	1.54	4.88	5.04	1.79	0.13	11.07
Ornans	CO	3	1	19.80	1.51	4.52	4.30	1.29	0.11	10.05
Lancé	CO	4	1	5.00	1.57	12.97	14.74	6.09	0.16	30.09
Moss	CO	4		13.90	1.71	5.57	8.82	5.10	0.24	13.80
Warrenton	CO	4	1	30.60	1.66	2.81	4.03	2.16	0.22	6.85
Allende	CV	3	1	5.20	1.52	7.03	6.93	2.24	0.12	15.75
Bali	CV	3	3		1.64				0.20	
Grosnaja	CV	3	3	1.70	1.50	18.41	16.89	4.61	0.10	40.51
Kaba	CV	3	1	11.80	1.47	7.61	6.21	1.13	0.06	16.21
Mokoia	CV	3	1	9.70	1.53	1.19	1.18	0.39	0.12	2.67
Vigarano	CV	3	2	5.60	1.58	21.96	25.64	11.00	0.17	51.24
Karoonda	CK	4	1	40.20	1.42	1.77	1.21	0.03	0.01	3.58
Ningqiang	CK	3	1	39.70	1.54	5.35	5.55	1.98	0.14	12.14
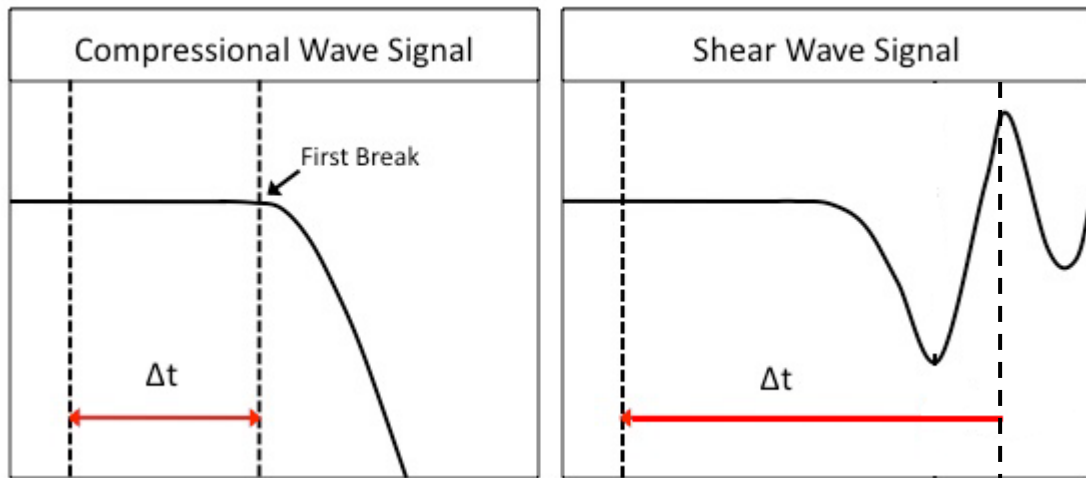
An illustration of compressional and shear waves; where the Δt shows the wave travel time, the dashed lines on the shows the start and first break on the waves.

APPENDIX C: CALCULATION OF MUTUAL IMPACT RATES

$$Number\ of\ impacts\ by\ a\ certain\ ``impactor"\ type\ per\ T_{\frac{1}{2}} = \left(\frac{1}{T_{\frac{1}{2}}\ of\ impactor}\right) *\ T_{\frac{1}{2}}\ of\ target$$

$$Number\ of\ impacts\ by\ a\ certain\ ``impactor"\ type\ per\ a\ million\ years\ = \frac{1}{T_{1/2}\ of\ impactor}$$

$$Number\ of\ impacts\ by\ "weaker"\ impactors\ on\ "weaker"\ targets\ per\ T_{1/2}\ =$$

$$\frac{\left[T_{1/2}\ of\ weaker - \left(T_{1/2}\ of\ hydrated\ meteorites * impacts/MY\right) + \left(T_{1/2}\ of\ stony\ meteorites * impacts/\ MY\right)\right]}{T_{1/2}\ of\ hydrated\ meteorites}$$

$$Number\ of\ impacts\ by\ hydrated\ impactors\ on\ hydrated\ targets\ per\ T1/2 =$$

$$\frac{\left[T_{1/2}\ of\ hydrated - \left(T_{1/2}\ of\ stony\ meteorites * impacts/MY\right) + \left(T_{1/2}\ of\ iron\ meteorites * impacts/\ MY\right)\right]}{T_{1/2}\ of\ hydrated\ meteorites}$$

$$Number\ of\ impacts\ by\ stony\ impactors\ on\ stony\ targets\ per\ T_{1/2}\ =$$

$$\frac{\left[T_{1/2}\ of\ stony - \left(T_{1/2}\ of\ iron\ meteorites * impacts/\ MY\right)\right]}{T_{1/2}\ of\ stony\ meteorites}$$

APPENDIX D: NOTES ON METHODOLOGY FOR FUTURE WORK

Specifications for equipment used throughout this study:

1. Ultrasonic contact transducers:

- V133-RM 2 Contact Transducer, 2.25 MHz, 0.25 in. Element Diameter, Fingertip Case Style, Right Microdot Connector.

- V156-RM 2 Contact Transducer, 5.00 MHz, 0.25 in. Shear element size, Fingertip Case Style, Right Microdot Connector.

- BCM-74-6 5 BNC to Microdot. 6 ft.

2. Electric Pulse generator/ receiver: 5077PR-15-U 1 Variable 400-volt square-wave pulser/receiver with 35MHZ bandwidth.

3. C- clamps

4. Measuring containers: plastic and glass, and a large plastic or metal tray.

5. Glass Beads: preferably new or cleaned with an ultrasonic cleaner.

6. Tektronix Model DP03014 Digital Phosphor Oscilloscope, 4 Channels, 100 MHz, 1 GS/s. 4 leads. No monitor was attached.

7. Software used for image processing:

- Image J version 1.46: platform independent. Download: bundled with 32-bit Java 1.6.0_20 (28MB), with 64-bit Java 1.6.0_20 (24MB; requires 64-bit Windows) or without Java (3MB). Website: http://rsbweb.nih.gov/ij/download.html

- ArcGIS version 9.3: http://resources.arcgis.com/content/arcgisdesktop/9.3/about

Notes:

- Beads of smaller sizes are more likely to cause problems when used for meteorites as they fill existing pores and fractures on samples (troublesome to get out). However, they are better at settling around meteorite samples.

- While working with ultrasonic transducers, its good practice to wipe the surface of transducers to prevent contamination, and to work on a disposable platform (Aluminum foil is useful) to avoid mixing powders of different samples.

- Frequencies recommended by the manufacturer to operate the pulse generator have been tested; however, using a lower frequency (1 MHz) provided stronger and clearer signals. Therefore, 1 MHz frequencies were used throughout the study.

- Not using C-clamps to put pressure on the transducers while holding the samples jeopardizes the results, as the first-break in the waveform changes position slightly depending on the quality of contact between the sample and transducers. It is recommended to put as much pressure as the sample could handle to optimize the sample- transducer contact. This been said, I have broken two samples through the measurements (pure accident), because she put more pressure than recommended.

- It is useful and preferable to record waveforms using a USB device. This would increase the level of confidence in results, and it will enable comparisons between different meteorites.

- ALWAYS have a research notebook! Not because computers are not trustworthy, but keeping everyday record of activities makes writing a thesis a less painful and more enjoyable process.